TABLE OF CONTENTS

Page

LIST OF TABLES

Page

LIST OF FIGURES

Page

LIST OF ABREVIATIONS AND ACRONYMS

3D	Three-dimensional
2D	Two-dimensional
AM	Additive manufacturing
BFG	Blas furnace gas
BGG	Biogas-gasified gas
CAD	Computer aided design
CGB	Conventional gas burner
Co	Cobalt
Cr	Chrome
CT	Computed tomography
EDM	Electrical discharge machining
GHG	Greenhouse gas
HC	Hydrocarbons
LCG	Low calorific gas
LG	Landfill gas
LPBF	Laser powder bed fusion
LPG	Liquefied petroleum gas
PM	Porous medium
PMB	Porous medium burner
PPC	Pores per centimeter
PPI	Pores per inch
SLM	Selective laser melting
SiSiC	Silicon-silicon carbide
UHC	Unburned hydrocarbons
VG	VGStudio Max 3.0 software

LIST OF SYMBOLS AND UNITS OF MEASUREMENT

Symbols, Latin Letters

A	$[m^2]$	Area
A_c	$[m^2]$	Cell area
A/F	[-]	Air-fuel ratio
a	$[m]$	Unit cell size
c_p	$[J/K]$	Specific heat capacity
D	$[m]$	Diameter
D_i	$[m^2/s]$	Mass diffusivity
d_c	$[m]$	Cell diameter
d_h	$[m]$	Hydraulic diameter
d_p	$[m]$	Pore diameter
E	$[GPa]$	Young's modulus
E_{ign}	[J]	Ignition energy
F	[-]	Forchheimer coefficient
FSR	[-]	Flame-speed ratio
h_v	$[W/(m^3 \cdot K)]$	Volumetric heat transfer coefficient
K_{1C}	$[MPa \cdot m^{1/2}]$	Fracture toughness
k	$[W/(m \cdot K)]$	Thermal conductivity
L	$[m]$	Length
Le	[-]	Lewis number
l_{ref}	$[m]$	Length of the reference line
m	$[kg]$	Mass
n_{int}	[-]	Number of intersections
n_x, n_y, n_z	[-]	Number of unit cells in x-, y-, z-direction
P	$[m]$	Perimeter
Pe	[-]	Péclet number
p	$[Pa]$	Pressure
Δp	$[Pa]$	Pressure difference
R	$[K]$	Thermal shock resistance parameter
S_L	$[m/s]$	Laminar flame speed
S_{surf}	$[m^2]$	Surface area
S_v	$[m^{-1}]$	Specific surface
V	$[m/s]$	Effective flame speed
V_c	$[m^3]$	Cell volume
V_s	$[m^3]$	Solid volume
ΔV	$[m/s]$	Stable dynamic range
Q	$[W/m^2]$	Firing rate (heat output)
$\dot{Q}$	$[m^3/s]$	Flow rate
T	$[K]$	Flame temperature
$T_{max,op}$	[°C]	Maximum operational temperature

t_{ASTM}	$[m]$	Mean chord length based on ASTM D3576-15 standard
t_s	$[m]$	Mean strut thickness

Symbols, Greek Letters

α	$[m^2/s]$	Thermal diffusivity
α_0, α_1	[-]	Constants in the Forchheimer equation
α_t	$[K^{-1}]$	Thermal expansion coefficient
δ	$[m]$	Pebble diameter
ε	[-]	Porosity
η	$[\%]$	Efficiency
$\kappa_{g,s}$	[-]	Heat transfer coefficient between gas and solid phases
κ_{perm}	$[m^2]$	Absolute permeability measured in the Darcy regime
κ_{rad}	$[m^{-1}]$	Radiative extinction coefficient
μ	$[Pa{\cdot}s]$	Viscosity
ν	[-]	Poisson's ratio
ρ	$[kg/m^3]$	Density
σ_a	$[m^{-1}]$	Absorption coefficient
σ_e	$[m^{-1}]$	Extinction coefficient, $\sigma_a + \sigma_s$
σ_s	$[m^{-1}]$	Scattering coefficient
σ_t	$[MPa]$	Tensile strength
τ	[-]	Optical depth, $\sigma_e L$
ϕ	[-]	Equivalence ratio
Ψ	[-]	Sphericity
ω	[-]	Scattering albedo, σ_s/σ_e

Subscripts

Ar	Archimedes
$ASTM$	Based on the ASTM D3576-15 standard
ad	Adiabatic
app	Apparent
cl	closed
cl,p	closed pore
$corr$	Corrected
cr	critical
cr,r	critical rich
cr,l	critical lean
cs	Based on the cross-section slice method
eff	Effective
eq	Equivalent
f	Foam
g	gas

hex	hexagon
lat	Diamond lattice
m	Mean
man	Manufacturer
max	maximum
min	minimum
op	Open
$oper$	operational
ref	reference
s	solid
$stoic$	Stoichiometric
sph	Based on the maximal inscribed sphere method
sq	Square
$tetr$	tetrakaidecahedron
tot	Total
uc	Unit cell
w	Water
$w, 2D$	Based on the watershed method of 2D image slices
$w, 3D$	Based on the watershed method of 3D volume
$w, 3D, surf$	Based on the watershed method of 3D volume and cell outer surface

INTRODUCTION

0.1 The problem at hand

More stringent emission standards and the depletion of natural resources require the development of advanced combustion techniques. Through numerous research efforts, the application of porous medium burners (PMB) has been proven as advantageous, since these PMBs provide higher thermal efficiency, lower pollutant emissions, and use less fuel in comparison to conventional gas burners (CGB) (M. A. Mujeebu, M. Z. Abdullah, M. Z. A. Bakar, & A. A. Mohamad, 2011). These burners also provide the possibility of burning low-calorific fuels and lean fuel/air mixtures, which are normally nonflammable (S. Wood & A. T. Harris, 2008). These days, PMBs have widespread industrial (GoGas, 2008) and household (F. Avdic, 2004) applications. The most investigated design is the two-section PMB design composed of ceramic reticulated foams, where the upstream region with small pores acts as a flame arrestor and a preheater of incoming gases, and the downstream section with large pores provides flame support and heat recirculation in the porous medium (PM) (M. A. Mujeebu et al., 2009).

Various approaches of numerical analysis have been undertaken to predict the performance of ceramic foams and optimize their geometry (A. P. Horsman, 2010). However, non-uniform cell size distribution (J. T. Richardson, Y. Peng, & D. Remue, 2000) and low repeatability among specimens of the same type (J. Grosse et al., 2009) lead to difficulty in evaluating heat transport properties and combustion processes. Though ceramic foams can withstand high operational temperatures and provide good heat recirculation, they are subject to thermal shock and structural failures (V. R. Vedula, D. J. Green, & J. R. Hellman, 1999), which might influence the operational stability of the burner.

0.2 Proposed solution

For this reason, the development and application of porous structures with organized and definite morphology represent great potential for achieving the optimum characteristics in

PMB designs. The diamond lattice is one such morphology which has been previously studied in the laboratory of LAMSI (M. Dumas, P. Terriault, & V. Brailovski, 2017). For the production of such complex shapes, it is recommended to use additive manufacturing (AM) technology. In terms of the material, CoCr alloy, which is designed for application at elevated temperatures (≤ 1150 ℃), is considered a good candidate for the replacement of ceramics given its better resistance to thermal shock and crack propagation.

0.3 Research objective

The research objective of this study was defined as follows:
Study the impact of the material properties and porous media (PM) geometry on the performances of additively manufactured porous medium burners.

To reach this general objective, specific project objectives were specified as follows:

1) Analyze conventional ceramic foams using advanced visualization and image treatment techniques;
2) Design diamond lattice PM with flow characteristics similar to those of the conventional ceramic foams
3) Manufacture the diamond lattice PM using laser powder bed fusion (LPBF) additive manufacturing technique;
4) Compare, experimentally, the performances of the foam and diamond lattice PMBs made of two different materials (SiSiC ceramics and CoCr metallic alloy).

0.4 Organization of the thesis

The first chapter presents a literature review which familiarizes the reader with combustion fundamentals and introduces the principles of PMB operation. The main parameters that influence PMB's performance (flame stability limits, thermal output and efficiency, pollutant emissions, etc.) are also discussed. The second chapter describes our motivation for the selection of our experimental setups, allowing comparison between foam and diamond lattice geometries as well as between ceramic and CoCr materials. This chapter will discuss

methods of foam analysis based on CT scan data and approaches in designing the equivalent diamond lattices with further production by means of AM. We also describe the test bench assembly and the equipment used. The third chapter explains the experimental proceedings of six experimental setups and presents the results of temperature, pollutant emissions, and pressure drop measurements, as well as the assessment of PM structural durability after burning tests. The conclusion section provides a summary of the work, and the recommendation section proposes the next steps needed for advancement in the development of PMBs.

CHAPTER 1

LITERATURE REVIEW

1.1 Combustion fundamental principles

Combustion is a chemical reaction between a *fuel* and an *oxidizer* which normally generate heat and light in the form of a flame. Flames can be divided into two types: premixed flames and diffusion flames. Premixed flames are formed by mixing fuel and oxidizer prior to entering the combustion zone, whereas diffusion flames are formed by diffusion at the border between fuel and oxidizer, such that mixing and combustion occur simultaneously (F. El-Mahallawy & S. El-Din Habik, 2002). This thesis only examines premixed combustion. Moreover, in the majority of cases, methane/air (CH_4/air) mixtures are assumed, if not specified otherwise. This is dictated by the fact that natural gas is primarily composed of methane, and the majority of experiments are undertaken with this gas.

An important characteristic that defines mixture composition is the equivalence ratio (ϕ). This ratio indicates whether combustion occurs for the fuel-lean ($\phi < 1$), stoichiometric ($\phi = 1$), or fuel-rich ($\phi > 1$) mixtures and is represented by:

$$\phi = \frac{(A/F)_{stoic}}{(A/F)} \tag{1.1}$$

where $A/F = m_{air}/m_{fuel}$ is the air-fuel ratio.

Another essential feature is laminar flame speed (S_L), which defines the speed of chemical reaction between reactants, and is equal to the unburned reactants' velocity (V) at stationary condition. Figure 1.1 shows the dependence of equivalence ratio ϕ on laminar flame speed and adiabatic flame temperature (T_{ad}). Laminar flame speed is directly dependent on flame temperature. Both S_L and T_{ad} maximums are attributed for a slightly rich mixture and drop on both sides. The flammability limit $\phi_{min} < \phi < \phi_{max}$ is the point at which combustion

can be sustained. Beyond these limits, the energy release of combustion is lower than the required ignition energies (E_{ign}), and insufficient to provide self-sustaining flames (C. E. Baukal Jr., 2012). Preheating reactants lowers the required E_{ign} and allows for extending flammability limits (B. Dikici, M. L. Pantoya, & V. Levitas, 2010).

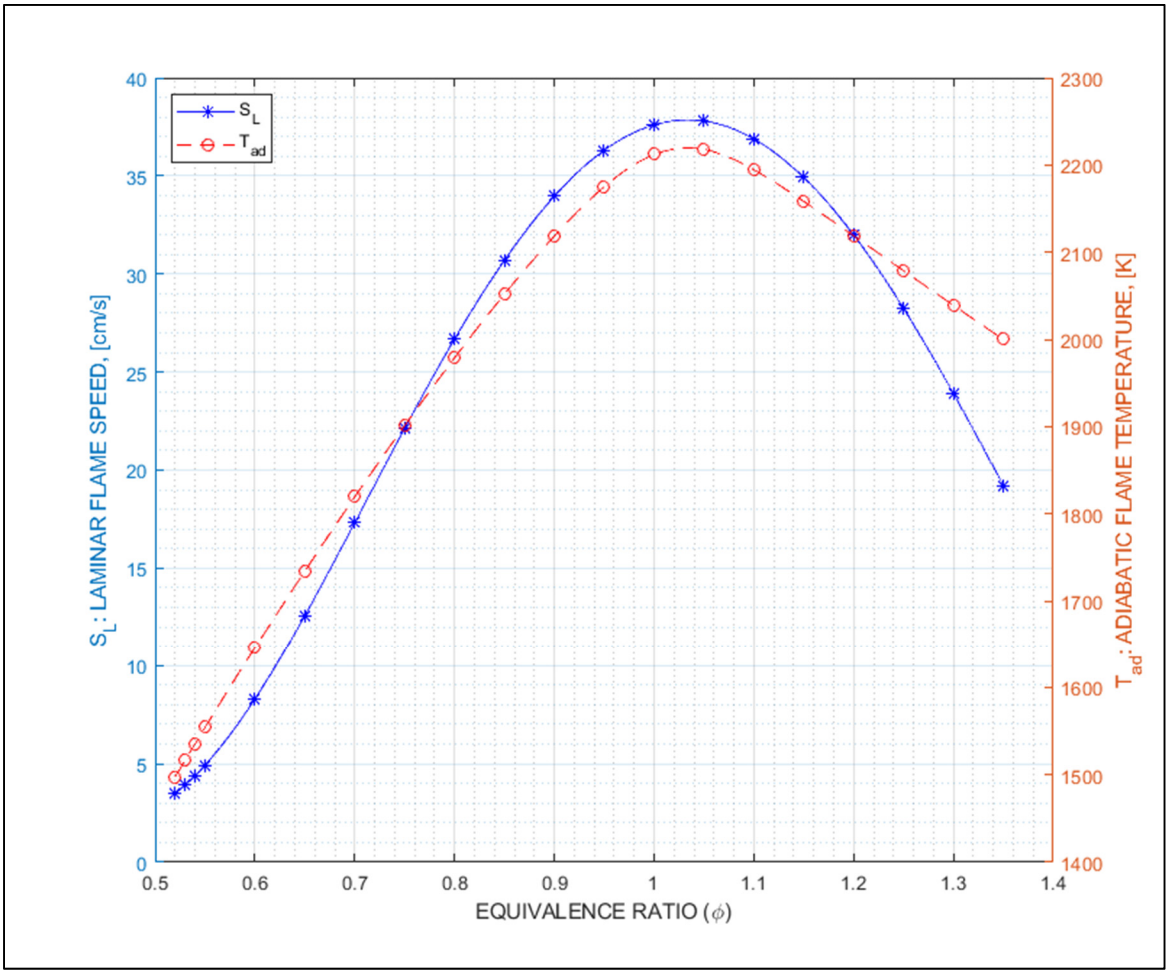

Figure 1.1 *CH₄/air* mixture: influence of equivalence ratio ϕ on laminar flame speed S_L (P. Ouimette & P. Seers, 2009) and flame temperature T_{ad} (R. Stone, A. Clarke, & P. Beckwith, 1998)

Another important characteristic of flame is the formation of species in combustion products. Below is the theoretical combustion equation for stoichiometric ($\phi = 1$) Eqn. (1.2), fuel-lean ($\phi < 1$) Eqn. (1.3) and fuel-rich ($\phi \geq 1$) Eqn. (1.4) mixtures (S. McAllister, J.-Y. Chen, & A.C. Fernandez-Pello, 2011).

$$CH_4 + 2(O_2 + 3.76N_2) \rightarrow CO_2 + 2H_2O + 7.52N_2 \quad (1.2)$$

$$CH_4 + \frac{2}{\phi}(O_2 + 3.76N_2) \rightarrow CO_2 + 2H_2O + \frac{7.52}{\phi}N_2 + \frac{2(1-\phi)}{\phi}O_2 \quad (1.3)$$

$$CH_4 + \frac{2}{\phi}(O_2 + 3.76N_2) \rightarrow \frac{1}{\phi}CO_2 + \frac{2}{\phi}H_2O + \frac{7.52}{\phi}N_2 + (1 - \frac{1}{\phi})CH_4 \quad (1.4)$$

The inevitable pollutant product produced during the combustion of hydrocarbons is carbon dioxide (CO_2), and for fuel-rich mixtures, the inevitable product is unburned hydrocarbons (UHC). However, in real-world applications, additional pollutants are formed, with the primary pollutants being carbon monoxide (CO), nitric oxides (NO_x), and UHC even for fuel-lean mixtures. Figure 1.2 represents the dependence of the main pollutant emissions on equivalence ratio.

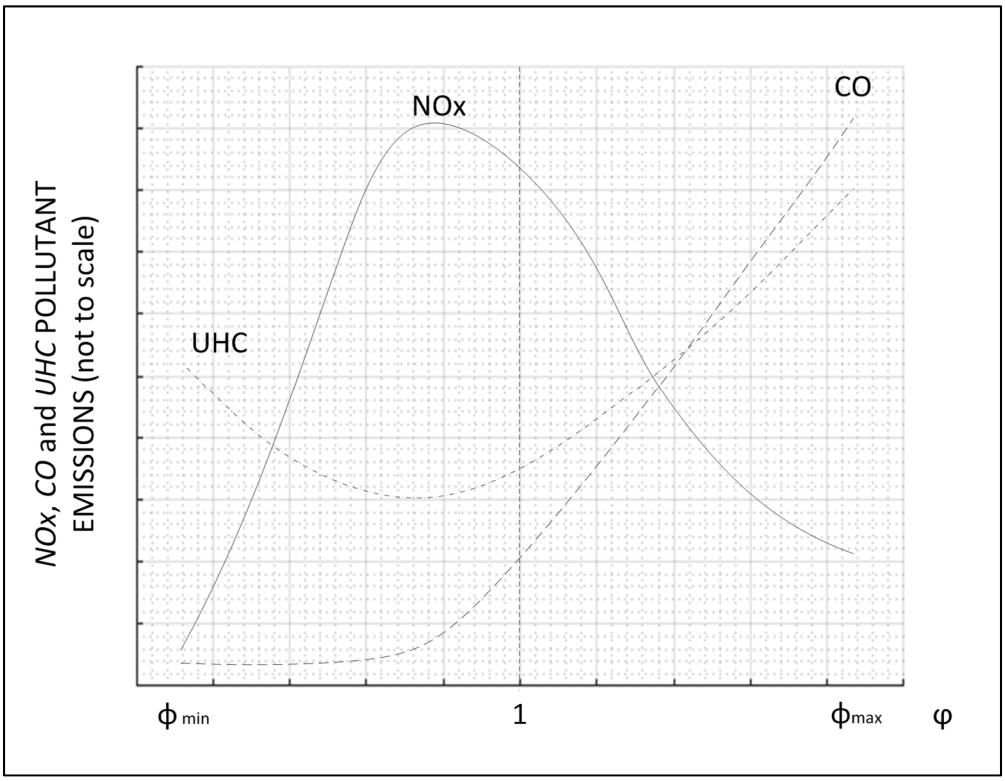

Figure 1.2 Pollutant emissions of *NOx*, *CO* and *UHC* as a function of fuel/air equivalence ratio
Adapted from J. B. Heywood (1988)

Formation of CO is mainly attributed to fuel-rich mixtures, and their concentration drops considerably by burning leaner mixtures (S. R. Turns, 2000). Formation of UHC is also mainly attributed to fuel-rich combustion, though UHC levels increase, while approaching flammability limits and quenching distances (S. R. Turns, 2000). NO_x formation in the premixed combustion of hydrocarbons is attributed for two main mechanisms. One is *prompt* NO, which occurs at low temperatures for fuel-rich mixtures, and the other is *thermal* NO_x, which occurs at high temperatures ($T > 1600$ ℃) (S. R. Turns, 2000). Combustion in PMB, due to burning leaner mixtures and high radiant emissions from the porous medium (PM), results in lower flame temperatures and, as a result, lower NO_x formation (S. Gauthier, A. Nicolle, & D. Baillis, 2008; A. Williams, R. Woolley, & M. Lawes, 1992).

1.2 Basic porous foam burner

In this section, we present the operating principles and research findings associated with combustion in porous medium burners.

Conventional gas burners (CGB) directly burn the incoming mixture by producing free open flames and releasing heat through a chemical reaction between fuel and oxidizer. PMB can be considered a modified CGB with an intermediary material allowing for the passage of the gas mixture and providing heat recirculation between the post- and pre-flame zones. Figure 1.3 shows the operational principle of the standard PMB consisting of two different PM, the subject of this thesis. The distinction between PMs is often made based on pore size, which is defined by the number of “pores per inch” (PPI) or “pores per centimetre” (PPC). The bigger the PPI/PPC value, the smaller the pores that allow for the passage of the mixture, resulting in a greater flow restriction. Thus, PMB consists of the downstream combustion region *C* (big pores and low PPI) and the upstream preheating region *A* (small pores and high PPI) as shown in Figure 1.3. The downstream region also plays the role of a radiant heater, whereas the upstream region plays the role of a flame arrestor, preventing the flame from going upstream towards the mixture inlet. The combustion heat that is emitted from the burner is partially recirculated from the downstream region to the upstream region by conduction,

while the remaining energy is available to heat by radiation; heat dispersion by convection and conduction is also possible with the burner exterior body.

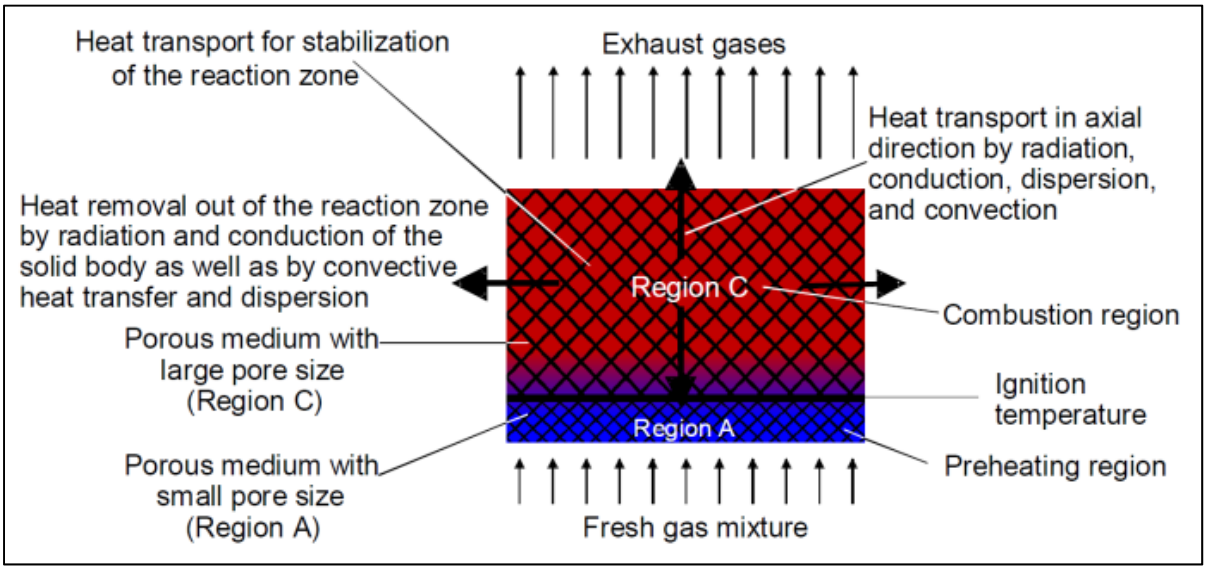

Figure 1.3 Heat transport in the two-stage porous burner
Taken from F. Avdic (2004)

Heat conduction from the downstream region to the upstream region allows for preheating by convection and radiation of the incoming reactants (air-fuel mixture). This allows the burner to obtain higher temperatures than it would without energy recirculation (D. R. Hardesty & F. J. Weinberg, 1974). The preheating of the mixture allows flame temperature to rise above T_{ad}. This configuration was studied by F. J. Weinberg (1971), who was one of the first to propose using the principle of excess enthalpy recirculation of combustion products to preheat incoming gases.

One advantage of using PMB is that preheating the fresh incoming mixture allows the burning operation range to increase. Figure 1.4 presents a comparison of flame stability diagrams for CGB and PMB. Abscissa (heat input) is proportional to the inlet gas velocity (V).

Flashback zone is defined as inlet velocities lower than S_L, such that a flame cannot be sustained and the flame front begins to propagate into the upstream section. A **quenching** distance (d_{cr}) exists for flames that is defined as the critical passageway below which flame cannot propagate. For safety reasons, flashback arresting devices with openings, which are smaller than d_{cr} but still allow for the passage of the mixture, should be employed.

Lifting flame zone is attributed to inlet velocities that are too high in comparison with S_L, and that cause the flame to be displaced downstream too far from the burner's edge. Further increases in V results in blow off of the flame. Combustion in PM results in higher flame speeds and inlet velocities.

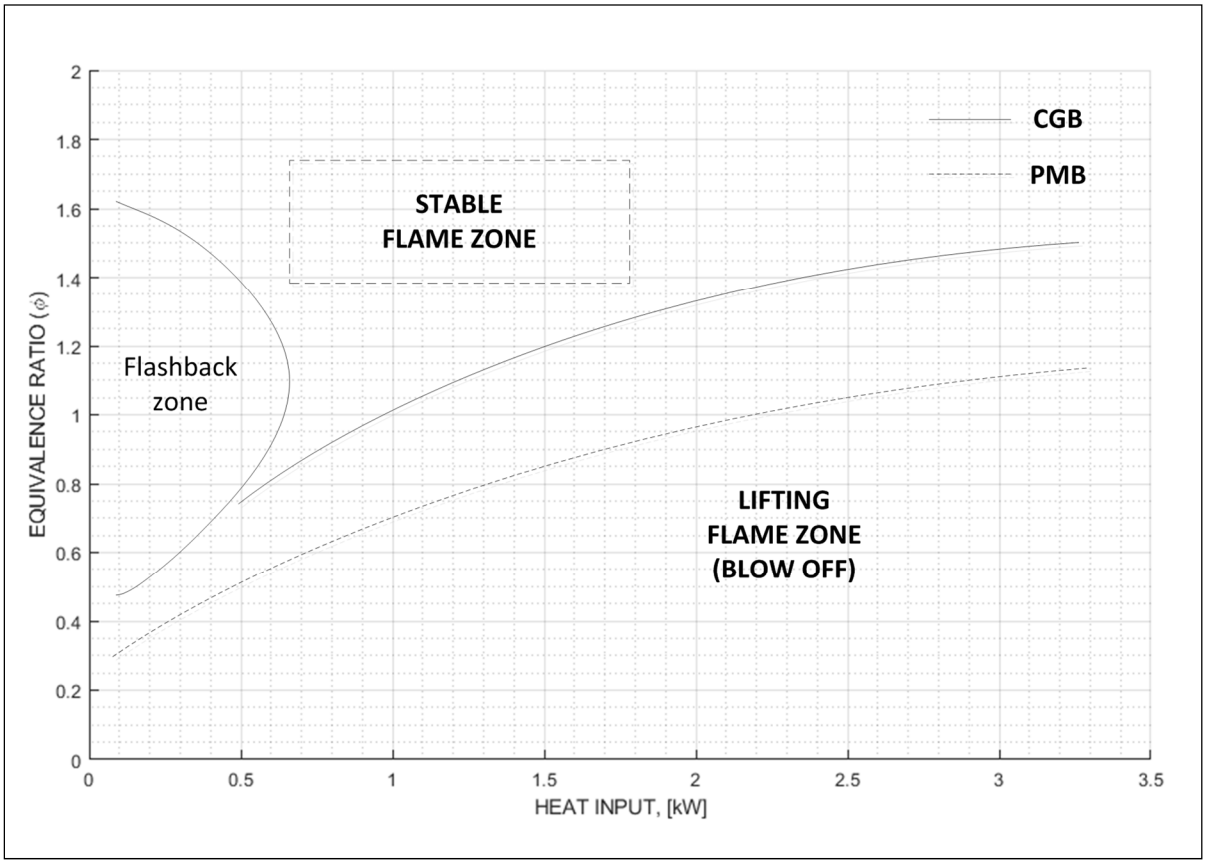

Figure 1.4 Stability diagram for CGB and PMB (CH_4/air)
Adapted from S. R. Turns (2000)

One of the first proposed designs for heat recirculation is shown in Figure 1.5, and was proposed by D. R. Hardesty and F. J. Weinberg (1974). The idea lies in the creation of adjacent walls between cold reactants and hot products pathways. Reactants enter the burner (blue) pathway and reach the combustion chamber where ignition occurs. Afterwards, they become hot combustion by-products that move through the exit (red) pathway. During this movement, hot gases preheat the adjacent walls through convection, which in turn through conduction, convection, and radiation start preheating the incoming reactants in the cold pathway.

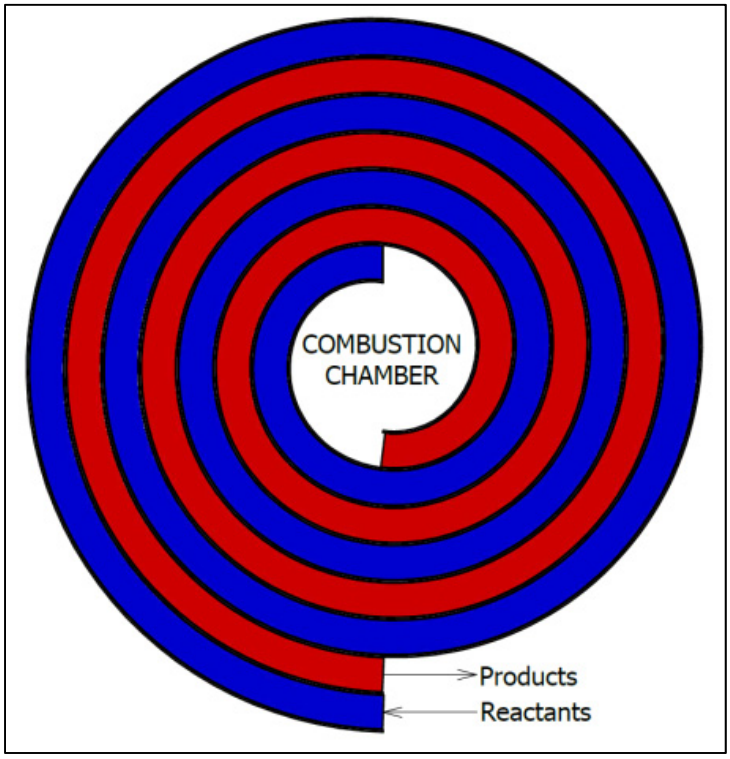

Figure 1.5 Section Cut of the Weinberg Burner
Adapted from
A. R. Jones, S. A. Lloyd, and F. J. Weinberg (1978)

T. Takeno and K. Sato (1979) continued work on excess enthalpy combustion and proposed using one-stage porous media with high thermal conductivity in the combustion zone, which would be used as flame support and a heat recirculation medium. Their numerical results showed that the flame could be sustained for increased flow rate limits (in comparison with

conventional burners), which resulted in higher power outputs. Moreover, they found that the heat transfer coefficient between a solid and a gas ($\kappa_{g,s}$) has a significant influence on flame structure. For high $\kappa_{g,s}$, the flame is located in the upstream section which forces combustion to occur before entering the solid. By lowering $\kappa_{g,s}$, on the other hand, the flame front is displaced to the downstream section and becomes more concentrated.

The research of J. Buckmaster and T. Takeno (1981), T. Takeno, K. Sato, and K. Hase (1981) revealed two critical flow rates in PMB, above (blow-off) and below (flashback) which combustion cannot be sustained. Further investigation by T. Takeno and K. Hase (1983) revealed that an increase in PM length resulted in an increase in the blow-off limit.

S. B. Sathe, R. E. Peck, and T. W. Tong (1990) examined various parameters for the performance of one-dimensional PM using a numerical model. They found that to maximize the radiant output, optical depth (τ) should be ~10, and the flame should be stabilized near the centre of the PM. Optical depth indicates how opaque a material is to passing radiation. To increase burner performance, the medium should be strongly emitting-absorbing and have a low scattering albedo (ω) which is found as:

$$\omega = \sigma_s/\sigma_e \tag{1.5}$$

where σ_s is a scattering coefficient and σ_e is an extinction coefficient.

Experimental investigation of one-stage porous burners was conducted by S. B. Sathe, M. R. Kulkarni, R. E. Peck, and T. W. Tong (1991) using a methane-air mixture at low equivalence ratios ($\varphi = 0.5 - 0.6$). It was revealed that radiant output, flame speed, and temperature increased with increasing equivalence ratio. The maximum radiant output was observed at the midplane of the burner.

V. S. Babkin, A. A. Korzhavin, and V. A. Bunev (1991) experimentally tested various porous materials and suggested that flame propagation might be characterized by a Péclet number

(Pe), which is a ratio of thermal energy convected to the fluid to thermal energy conducted within a fluid, and is given by Eqn. (1.6):

$$Pe = \frac{S_L \cdot d_{p,eff} \cdot c_{p,g} \cdot \rho_g}{k_g} = \frac{S_L d_{p,eff}}{\alpha_g} \tag{1.6}$$

where $d_{p,eff}$ is an effective pore diameter, $c_{p,g}$ is gas specific heat capacity, ρ_g is gas density, k_g is gas thermal conductivity, and α_g is gas thermal diffusivity.

Its critical value (Pe_{cr}) was found to be around 65, such that for $Pe_{cr} \geq 65$, flame propagation was observed, while for $Pe_{cr} < 65$, the flame was quenched.

Numerical and experimental investigation of two-stage PMB with high PPI in the upstream section and small PPI in the downstream section was performed by P.-F. Hsu, W. D. Evans, and J. R. Howell (1993). This conceptual design is the main configuration investigated in the literature, where upstream (region *A*) and downstream (region *C*) sections act in tandem as preheating and stable combustion regions (see Figure 1.3). In their experiments, the flammability limits of CH_4/air combustion were investigated at different equivalence ratios. When a two-stage PMB was used, in comparison with free flame, they found higher maximum flame speeds and lower equivalence ratios at which flame could be sustained.

From the above-mentioned works and the information in section 1.1, we can conclude that there is promising potential in the burning of lean mixtures in PMB, which leads to higher flammability limits, higher heat outputs, and lower pollutant emissions (due to the possibility of stable burning at low equivalence ratios). Therefore, the following investigations were mainly focused on lean combustion and in particular: Temperature distribution, flammability limits and quenching, pollutant emissions, pressure drop and permeability, durability of porous materials, and the practical applications of PMB.

1.3 Temperature, radiant output and thermal efficiency

The experiment conducted by V. Khanna, R. Goel, and J. L. Ellzey (1994) revealed that with increasing equivalence ratio ($\phi = 0.6 - 0.87$) and increasing flame speed, maximum temperature (T_{max}) and heat output (Q) also increase. However, the radiant thermal efficiency (η) increased with both lowering ϕ and lowering V. Various PMB designs were tested in heat exchangers and overall efficiency of the system was found to be more than 90% (D. Trimis & F. Durst, 1996), (F. Avdic, 2004).

1.4 Flammability limits and quenching

Flammability limits

The flammability limits of PMB were experimentally studied by P.-F. Hsu et al. (1993), who observed that maximum flame speed (V_{max}) in PMB was much higher in comparison to adiabatic laminar flame speed (S_L). With an increase in equivalence ratio, V_{max} also increased, whereas minimum flame speed (V_{min}) was not substantially affected by equivalence ratio. By decreasing pore size (and increasing PPI) in the downstream section, they observed a decrease in V_{max} and an increase in V_{min}, which resulted in a lower dynamic range ($\Delta V = V_{max} - V_{min}$) of the PMB.

In another design of a two-stage porous burner, authors (R. Mital, J. P. Gore, & R. Viskanta, 1997) observed flashback tendencies resulted from higher-than-expected preheating and a broader reaction zone. In analyzing the dimensions of the chosen porous foams, they hypothesized that this may have been due to their insufficient upstream and downstream thicknesses. (A. J. Barra & J. L. Ellzey, 2004) investigated burners with different foam lengths. They found that for circular radiant configuration, the safe and reasonable ratio of the foam's length (L) to its diameter (D) is $L/D \geq 0.5$.

The influences of various parameters were numerically examined by A. J. Barra, G. Diepvens, J. L. Ellzey, and M. R. Henneke (2003). It was determined that V_{min} and V_{max} were mainly controlled by upstream and downstream sections, respectively. By varying different parameters to maximize dynamic range, it was found beneficial to use material with low thermal conductivity (k) and high volumetric heat transfer coefficient (h_v) in the upstream section. In the downstream section, on the other hand, it is advantageous to use materials with high k and high h_v. A high radiative extinction coefficient (κ_{rad}) was found to be important in the upstream section, which corresponds to small pore size. Additionally, with increasing ϕ, they observed an increase in the burner's dynamic range ($\Delta V = V_{max} - V_{min}$).

(N. Djordjevic, P. Habisreuther, & N. Zarzalis, 2012a) investigated the influence of air inlet temperature on firing rate limits. By preheating the air, they found that they could burn leaner mixtures with higher firing rates. By comparing two ceramic materials, Al_2O_3 and $SiSiC$, they found that SiSiC demonstrated better flame stabilization due to its higher heat transport properties, but had a lower temperature operation limit.

Investigation of the operational ranges of different porous materials and pore sizes was made by H. B. Gao, Z. G. Qu, X. B. Feng, and W. Q. Tao (2014). V_{min} in the downstream section was not sensitive to material; however, V_{max} increased in the order of Al_2O_3, ZrO_2, SiC, $FeCrAl$, which correlates with each material's thermal conductivity. By increasing pore size in the downstream section, V_{min} increased, and that increase was accompanied by a simultaneous decrease in V_{max} resulting in a decrease of total dynamic range (ΔV).

Quenching

(V. S. Babkin et al., 1991) experimentally confirmed that flame extinction is characterized by critical Péclet number (Pe_{cr}) equal to 65, such that for $Pe < Pe_{cr}$, flame quenches, and for $Pe > Pe_{cr}$, flame propagates. After examining Eqn. (1.6), they concluded that for a given mixture (α_g) and flow regime (S_L), a corresponding critical pore diameter ($d_{p,cr}$) exists.

$$Pe_{cr} = \frac{S_L \cdot d_{p,cr}}{\alpha_g} \tag{1.7}$$

This fact motivates to the determination of materials with appropriate pore diameters in the upstream and downstream regions, satisfying flame quenching and flame propagation conditions, respectively. However, in the case of high temperature in the medium (T_s), flame propagation is possible, which is attributed to the fact that reactions are not extinguished by cold walls. This process is called filtration combustion.

A number of research efforts were undertaken to verify the criterion $Pe_{cr} = 65$. (D. Trimis & F. Durst, 1996) investigated Pe_{cr} for sphere packing at stoichiometric regime ($\phi = 1$, $S_L = 40\ cm/s$) by varying pebble diameters (δ), and found the critical value (δ_{cr}) to be $9\ mm$, which fit well with the criterion $Pe_{cr} = 65$. Pore diameter of sphere packing in this case was evaluated based on the assumption of flame quenching in the narrow tubes with a diameter equal to the maximum pores (G. A. Lyamin & A. V. Pinaev, 1987):

$$d_p = \frac{\delta}{2.77} \tag{1.8}$$

(D. Trimis & K. Wawrzinek, 2004) continued experiments with spheres. In their work, three different pebble diameters were chosen and the equivalence ratio varied by reaching fuel-lean (ϕ_{min}) and fuel-rich (ϕ_{max}) limits until quenching occurred. Variation in ϕ resulted in variation of S_L (see Figure 1.1), such that two different critical Péclet numbers were found, corresponding to lean ($Pe_{cr,l} \approx 38$) and rich ($Pe_{cr,r} \approx 92$) limits, which resulted in mean $Pe_{cr} = 65 \pm 27$. Another important discovery was the influence of mixture type on the Pe_{cr} by Lewis-number (Le), which is the ratio of thermal (α_g) to mass (D_i) diffusivity:

$$Le = \frac{\alpha_g}{D_i} = \frac{k_g}{\rho_g c_{p,g} D_i} \tag{1.9}$$

Evaluation of Le for various mixtures and equivalence ratios is described by J. K. Bechtold and M. Matalon (2001) and P. Ghanbari-Bavarsad (2008). For CH_4/air at various ϕ, Le might be considered constant and equal to unity (D. Lapalme, R. Lemaire, & P. Seers, 2017), whereas for certain gases, Le changes with equivalence ratio. It should be taken into account that for $Le \geq 1$, the value of Pe_{cr} was found to be approximately equal to 65, and that for gases with $Le < 1$, Pe_{cr} decreases. As an example, Pe_{cr} for fuel-rich C_3H_8/air ($Le \approx 0.8$), fuel-lean H_2/air ($Le \approx 0.4$), and fuel-lean $H_2/Cl_2/HCl$ ($Le \approx 0.3$) mixtures were found to be 27, 17, and 6.5, respectively.

The influence of various configurations of porous materials on flame quenching and flame propagation was investigated by H. I. Joo, K. Duncan, and G. Ciccarelli (2006). Flame arresting properties were compared between various ceramic mediums, and their efficiencies order from most to least effective as follows: Drilled plates, packed spheres, and foams. The criterion of effectiveness was evaluated based on Pe_{cr} (with the higher being the better). It was found that packed spheres had superior (28% better) flame arresting properties in comparison to ceramic foams, which was attributed to the foam's higher void fraction. Additionally, they confirmed the existence of two Pe_{cr} corresponding to lean and rich limits.

In various resources with experimental data, authors combine flashback and quenching results together which complicates analysis. P.-F. Hsu et al. (1993) indicated that flame during flashback was possible to quench only by means of 65 PPI PSZ foam at $\phi = 0.55$, which corresponded to $Pe_{cr} \approx 1.4$. Such low Pe_{cr} value might be attributed to filtration combustion due to increased temperature in the medium after continuous preheating. In contrast, W. M. Mathis and J. L. Ellzey (2003) provided results of flashback, which corresponded to $Pe_{cr} \approx 14$ and H. B. Gao et al. (2014) to $Pe_{cr} \approx 4.5 - 13.5$ (in both cases, downstream region was considered critical). However, it was not specified whether the flame was quenched or not.

Represented discrepancies in calculated Pe_{cr} were also analyzed by N. Djordjevic, P. Habisreuther, and N. Zarzalis (2011), who proposed a method where two Péclet-numbers,

based on laminar flame speed (Pe_{S_L}) and on minimum velocity corresponding to blow off in PMB (Pe_{PMB}), were taken into account:

$$Pe_{PMB} = const\left(Pe_{S_L}\right)^2 \tag{1.10}$$

$$\frac{V_{min} d_p}{\alpha_g} = const\left(\frac{S_L d_p}{\alpha_g}\right)^2 \tag{1.11}$$

Linear correlations of $\log Pe_{PMB} = f(\log[Pe_{S_L}^2])$ for Al_2O_3 and $SiSiC$ PMs were obtained. However, certain coefficients should be determined for each burner separately. Figure 1.6 amalgamates the information from the various resources and demonstrates that for the chosen porous material and mixture type, critical Péclet-number and critical pore diameter can be found by defining lean and rich flammability limits. However, after reviewing the literature, we found discrepancies in the evaluation of Pe_{cr}, and further research in this field needs to be conducted. During operation, flame velocity should be set to an appropriate level such that the foam's temperature (T_s) at the upstream section does not increase to the level when flame propagation towards the inlet region occurs.

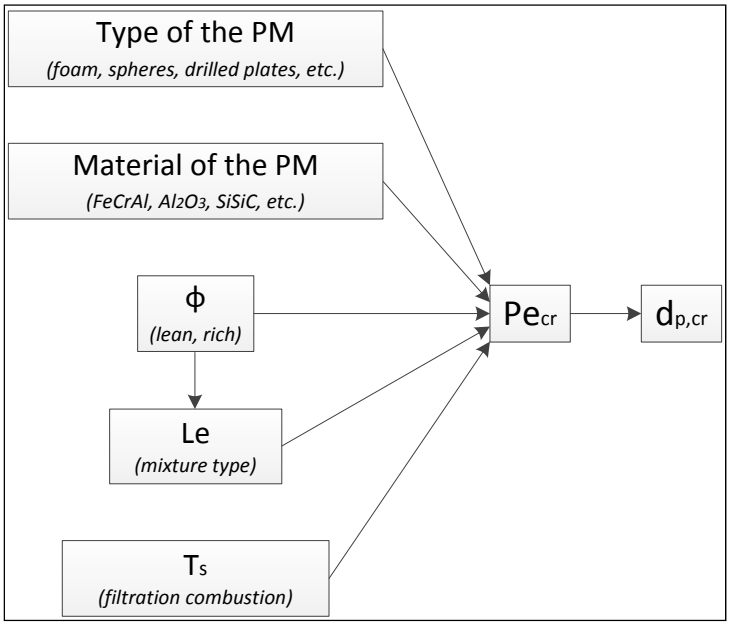

Figure 1.6 Influence of various parameters on Pe_{cr}

1.5 Pollutant emissions

CO emission

(V. Khanna et al., 1994) experimentally investigated a two-stage burner with a CH_4/air mixture. It was found that CO emissions mainly increased with increasing ϕ. However, for fixed ϕ, the minimum value of CO emission was found at the intermediary flame speeds located between V_{min} and V_{max}. Maximum CO emission was found for V_{max}. Under these conditions, the flame front was located at the downstream exit plane and provided less time for CO oxidation. Similar results were obtained by M. T. Smucker and J. L. Ellzey (2004) and C. Keramiotis, B. Stelzner, D. Trimis, and M. Founti (2012).

F. Avdic (2004) compared a conventional natural gas burner with PMB in a household application (using a boiler). This experiment showed considerable CO emission reduction in the PMB at the tested power ranges.

The majority of investigations were made with CH_4/air mixtures and several attempts were made to burn other fuels. G. J. Rørtveit, K. Zepter, Ø. Skreiberg, M. Fossum, and J. E. Hustad (2002) investigated the addition of H_2 to CH_4 in a number of PMB designs, and found no considerable effect of fuel type on CO emission levels. S. K. Alavandi and A. K. Agrawal (2008) tested CO and H_2 addition (in the same proportion) to the CH_4 mixture and observed a slight decrease in CO emission with a higher concentration of H_2 in the fuel. This experiment also investigated the dependence of CO emission in the transverse location, and found that pollution concentration was lower at the centre (corresponding to higher temperatures) and higher near the walls (corresponding to lower temperatures).

N. Djordjevic, P. Habisreuther, and N. Zarzalis (2012b) investigated the influence of the adiabatic flame temperature (T_{ad}) of CH_4/air mixture and found that CO emission increased with increasing T_{ad}, a finding that agrees with supported theory. By investigating CO

emission in the axial direction, authors found that CO emission decreased from the burner exit, which was attributed to the post-flame CO oxidation.

In the majority of experiments, CO emission was low and less than 60 ppm.

NO_x emission

In lean combustion, thermal NO_x is the main source of pollutant formation. In the experiment conducted by V. Khanna et al. (1994), the authors found that NO_x was less sensitive to flame speed, but mainly increased with equivalence ratio, which was in direct relation to T_{max}. C. Keramiotis et al. (2012) and D. Trimis and F. Durst (1996) confirmed these results through their own research. In the majority of cases, emissions were less than 30 ppm and often even less than 5 ppm or below the equipment detection limits.

UHC emission

R. Mital et al. (1997) investigated that UHC emission increased in proportion to an increase in equivalence ratio, and a decrease in firing rate. The same finding was observed by W. M. Mathis and J. L. Ellzey (2003). In the majority of cases, this value was low (less than 15 ppm). In the work of H. B. Gao et al. (2014), who used a perforated plate and 3 mm balls in the upstream section, high values of UHC emission (500-2500 ppm) were obtained at a low equivalence ratio ($\phi = 0.6$). UHC emission decreased with increasing flame speed. Increased flame speed leads to higher flame temperatures that lower the UHC formation at low ϕ.

1.6 Pressure drop and permeability

Pressure drop through the foam is important to understand the flow regime and energy dissipation mechanisms, and to evaluate heat transfer/reaction rates (N. Dukhan, Ö. Bağcı, & M. Özdemir, 2014). J. T. Richardson et al. (2000) investigated pressure drop for various foams and found that they follow the Forchheimer equation:

$$\frac{\Delta p}{L} = \alpha_0 V + \alpha_1 V^2 \tag{1.12}$$

where Δp is pressure drop, L is the length of the medium, V is the flow velocity, and α_0 and α_1 are constants.

The constants α_0 and α_1 were taken from Sabri Ergun and A. A. Orning (1949) and required correlations depending on the obtained pore diameter (d_p) and porosity (ε). As predicted, pressure drop increased with flow velocity and pore size (PPI).

Comparison between cold states and operational states in PMB was provided by M. T. Smucker and J. L. Ellzey (2004). Pressure drop (Δp) was higher for a hotter reaction flow (as opposed to a cold flow) and in all cases, Δp increased with ϕ and flow speed. However, for the reacting flow at high velocities ($> 70\ cm/s$), pressure drop experienced a plateau.

H. B. Gao et al. (2014) also observed higher Δp in hot states, though the difference between the two states in this research was not as prominent as the difference in M. T. Smucker and J. L. Ellzey (2004). By comparing Δp for foams with 10 PPI and 30 PPI, the latter had a slightly higher Δp. J. A. Wharton, J. L. Ellzey, and D. G. Bogard (2005) compared pressure drop for 10 PPI and 60 PPI foams at various velocities. They reported that with the 60 PPI foam, they observed a much higher Δp and higher non-linearity with increasing V.

Pressure drop through metal foam and various flow regimes was studied by N. Dukhan et al. (2014). They distinguished four flow regimes: Pre-Darcy, Darcy, Forchheimer, and turbulent. The modified Forchheimer equation was used:

$$\frac{\Delta p}{LV} = \frac{\mu}{\kappa_{perm}} + \frac{\rho F}{\sqrt{\kappa_{perm}}} V \tag{1.13}$$

where $\Delta p/LV$ is reduced pressure drop, μ is viscosity, κ_{perm} is the permeability coefficient measured in Darcy regime, ρ is density, and F is the Forchheimer coefficient. From this equation, reduced pressure drop becomes a linear function and dependent only on V, which

allows for the determination of permeability and the Forchheimer coefficient, which define and characterize porous medium structure.

1.7 Durability of porous materials

The main materials used in PMB for flame support and heat recirculation are ceramic foams. Due to their high temperature operation limits ($T_{op} > 1400\,℃$) and high thermal conductivity. However, ceramics are brittle materials by nature and prone to crack formation when exposed to high temperature gradients (P. J. Elverum, J. L. Ellzey, & D. Kovar, 2005) and thermal shocks (F. R. A. Mach, F. V. Issendorff, A. Delgado, & A. Ortona, 2009). These are the primary disadvantages of using ceramic materials in PMB designs. J. A. Wharton et al. (2005) investigated a two-stage PMB design, and after extensive use found that the foam degraded in the upstream section (small pore size, high PPI). This might be attributed to the fact that small foam struts are more susceptible to failure during thermal shocks and temperature gradients. Authors V. R. Vedula et al. (1999) confirmed this assumption, and determined that damage in ceramic foams is generally due to the propagation of pre-existing cracks and is strongly dependent on cell size, such that with a decrease in cell size the probability of damage increases.

The main parameters that characterize the capability of the material to withstand structural failure are thermal shock resistance parameter (R) and fracture toughness (K_{1C}). K_{1C} characterizes the ability of the material to withstand crack propagation (X.-K. Zhu & J. A. Joyce, 2012), whereas R characterizes the ability of the material to withstand temperature gradients and is found, according to J. W. Zimmermann, G. E. Hilmas, and W. G. Fahrenholtz (2008), as:

$$R = \frac{\sigma_t(1-\nu)}{E \cdot \alpha_t} \tag{1.14}$$

where σ_t is tensile strength, ν is Poisson's ratio, E is Young's modulus, and α_t is the thermal expansion coefficient.

The higher the R and the higher the K_{1C}, the more a material can withstand extreme temperature gradients and maintain structural consistency. According to N. R. Bose (2013), "Ceramic materials have a greater thermal shock sensitivity than metals and can suffer catastrophic failure due to thermal shock because of their unfavourable ratio of stiffness and thermal expansion to strength and thermal diffusivity, and their limited plastic deformation". This leads to the hypothesis that the application of metal foams in the upstream section (the region of average temperatures and high temperature gradients) might be advantageous, since these materials have a higher resistance to crack propagation.

1.8 Practical applications

The best proof of PMB feasibility is its practical application in heat exchangers, which has been investigated by D. Trimis and F. Durst (1996). Trimis and Durst demonstrated: High efficiency ($\eta > 90\%$), high dynamic range (20:1), low pollutant emissions, more stable combustion, and much smaller size of PMB as compared to conventional burners. In the work of F. Durst, D. Trimis, and K. Pickenäcker (1997), the authors enhanced the power output and elaborated the porous burner integrated with the heat exchanger, which worked in the wide dynamic range (3-30 kW) with low NO_x and CO emission. Application of PMB was demonstrated in one-piston and three-piston engines developed by S. Mößbauer, F. Durst, D. Trimis, and T. Haas (2001). F. Avdic (2004) presented an elaborated design of a PMB in a boiler system with both high efficiency and low pollutant emissions. Comparison of PMB with conventional burners in the household application was provided by M. A. Mujeebu et al. (2011). Once again, it demonstrated high efficiency and significant fuel savings (up to 80%) with much lower NO_x emissions. However, their design yielded higher CO emissions for PMB, but still within the range of global standards.

PMB application in stationary gas turbines was investigated by N. Djordjevic et al. (2012b) and N. Djordjevic et al. (2012a). These experiments demonstrated extremely low CO and NO_x concentrations, as well as a wide range of stable firing rates.

Such works demonstrate important potential for the development of future PMB designs.

1.9 Hypothesis and objectives

Based on the above-mentioned works, Figure 1.7 graphically illustrates the main advantages of combustion using PMB.

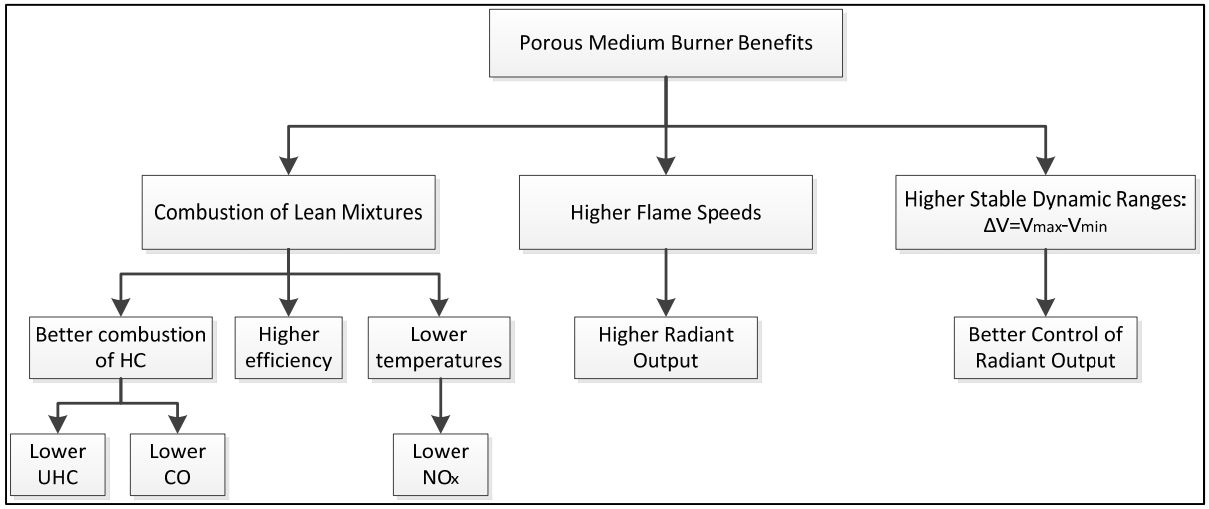

Figure 1.7 Advantages of PMB

Despite these advantages, there are several drawbacks to current designs. One of them is the use of ceramic foams. Though ceramic foams have a very high temperature operation range, they have low resistance to thermal shocks and temperature gradients which causes crack formation and structural failure. Moreover, discrepancies between ceramic specimens of the same manufacturer and type exist (due to the specificity of the manufacturing process and pore clogging) (J. A. Wharton et al., 2005), which results in unpredictable cell distribution (J. T. Richardson et al., 2000). Application of these reticulated structures with uncertain morphologies makes it difficult to predict essential parameters (i.e. thermophysical properties, pressure drops, etc.) with reasonable precision (J. R. Howell, M. J. Hall, & J. L. Ellzey, 1996).

One of the proposed solutions is to use lattice structures with high open porosity (A. Ortona, C. D'Angelo, S. Gianella, & D. Gaia, 2012), (S. Gianella, 2013). The application of diamond lattices provides simplicity for numerical simulation during preliminary design, so that the results obtained for a limited number of unit cells might be extrapolated to the whole uniform structure (A. Ortona, S. Pusterla, et al., 2012).

It may also be beneficial to use metal materials in the upstream section with low thermal coefficients (k), high volumetric heat transfer coefficients (h_v), and large radiative extinction coefficients (κ_{rad}) (A. J. Barra et al., 2003).

Hence, the application of additive manufacturing, in particular laser powder bed fusion (LPBF) of metals, may be beneficial in creating optimized porous materials with desired and predictable parameters. This approach would potentially allow for the improvement of PMBs' efficiency and reduce their pollutant emissions.

It was demonstrated that the selection of an appropriate d_p plays a crucial role in determining flammability limits and in the safety of the equipment. However, in the literature review no satisfactory methods were found to determine applicable $d_{p,cr}$ with a sufficient level of accuracy. Moreover, based on experimental results, the criterion of $Pe_{cr} = 65$ for CH_4/air mixtures should be verified, and so additional research in this field is necessary. Nonetheless, the determination of Pe_{cr} is out of the scope of the current research which is limited only to the determination of d_p in porous materials.

Thus, let's recall the general objective that was defined in section 0.3:
Study the impact of the material properties and porous media geometry on the performances of additively manufactured porous medium burners.

To reach this general objective, specific project objectives were specified as follows:

1) Analyse conventional ceramic foams using advanced visualization and image treatment techniques;

2) Design diamond lattice PM with flow characteristics similar to those of the conventional ceramic foams
3) Design and manufacture the diamond lattice PMB using selective laser melting additive manufacturing technique;
4) Compare, experimentally, the performances of the foam and diamond lattice PMBs made of two different materials (SiSiC ceramics and CoCr metallic alloy).

CHAPTER 2

METHODOLOGY

This section describes the process of selecting and characterizing ceramic foams, as well as the approach used to design diamond lattice structures. We present methods of geometric analysis of ceramic foams and propose an approach of selecting patterned porous media (PM) with flow characteristics similar to those of the foam. This section also describes the experimental setups and the nature of the tests that were performed.

2.1 Selection of porous materials and definition of experimental setups

This subsection explains how we selected suitable PMB ceramic foams and explains our decision to replace the foam's geometry with the diamond lattice structure. Moreover, this section also discusses the motivations for selecting our experimental setups.

2.1.1 Overview of ceramic foams

To establish a clear understanding of what a ceramic foam is, it is necessary to define a few basic terms, as there is some ambiguity around the definition of **"pore".** To avoid uncertainty, the definition used by manufacturers is employed in this thesis, where a "**pore**" is defined as the 2D opening, and a "**cell**" is defined as the 3D space surrounding the pore (D883-17 ASTM, 2017) (see Figure 2.1).

Foams have complex morphologies with widespread cell and pore size distributions (K. M. Lewis, I. Kijak, K. B. Reuter, & J. B. Szabat, 1996). According to one of the leading ceramic foam manufacturers (ERG Materials and Aerospace Corp.), one cell consists of approximately 14 pores of various shapes and sizes. This is simplified by averaging pores to find a mean diameter (d_p) of an equivalent circular pore. Initially, ceramic foams were applied in the filtering of molten metals. As a result, it was logical to define d_p as a

characteristic size through which impurities might be filtered. Manufacturers of ceramic foams provide one important parameter called "pore density," which is the number of pores per linear inch (PPI) or linear centimetre (PPC). Pore density indicates how many pores of an average diameter are able to fit along the reference distance. Thus, higher PPI/PPC values are associated with materials with a lower d_p.

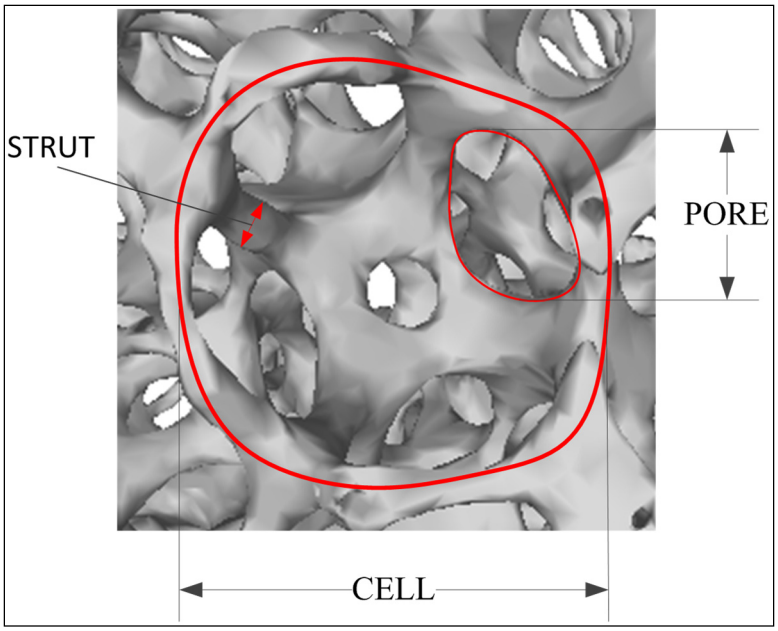

Figure 2.1 Definition of "pore," "cell," and "strut"
Adapted from ERG Materials and Aerospace Corp.

In the ceramic foam manufacturing process, a replication of polymer specimens made of one of the following materials is produced: Polyurethane (PU), polyvinyl chloride (PVC), or polystyrene (PS) (M. Scheffler & P. Colombo, 2005). The basic flowchart of foam manufacturing is illustrated in Figure 2.2. Initially, the foam polymer template is impregnated with ceramic slurry. It then undergoes pyrolysis (after which the initial polymer matrix is removed and the ceramic carcass is left), and the freed from polymer void spaces are finally infiltrated with ceramic material.

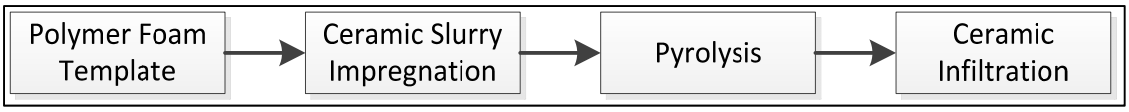

Figure 2.2 Flowchart of the ceramic foam manufacturing process
Adapted from A. Ortona, C. D'Angelo, et al. (2012)

Unfortunately, the main drawback of ceramic foam production is that the final specimen's geometry inevitably varies between specimens, even if they are produced by the same manufacturer (X. Fu, X. F. Viskanta, & J. P. Gore, 1998). This is due primarily to variability among the parent templates used, and at the stage of slurry coating. The latter occasionally results in the formation of closed pores (J. A. Wharton et al., 2005) that prevent fluid flow. This fact might be crucial for combustion, and informs research of alternative shapes that can be used with more predictable and controllable open-cellular structures.

2.1.2 Selection of foams and alternative ordered porous structures

This section explains the reasoning behind our choices of foam media for PMBs. SiSiC foams from EngiCer SA were selected based on their higher thermal conductivity compared to other ceramics (S. Gianella & A. Ortona, 2010). They were also selected based on their availability and successful applications by other researchers N. Djordjevic, P. Habisreuther, and N. Zarzalis (2009); J. Kiefer et al. (2009).

As mentioned in the previous section, ceramic foams have complex morphologies with widespread cell size distribution and low repeatability. The resulting inconsistencies have motivated the investigation of structures with open porosity—similar to the foam—but with definite geometry. In our case, regularly distributed porous structures represent an interesting alternative. To define such an alternative structure, we use the *Geometry-Material-Manufacturing* paradigm (see Figure 2.3).

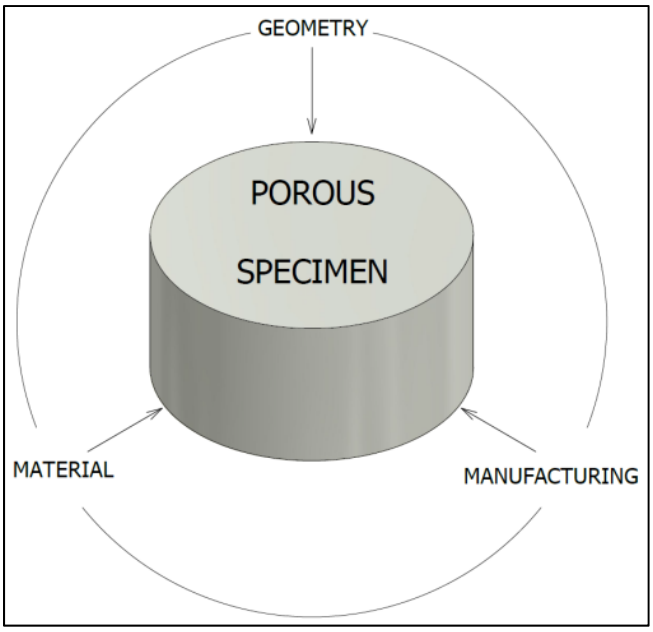

Figure 2.3 Geometry-Material-Manufacturing paradigm

From a *geometric* perspective, the specimen's structure should possess both open porosity (ensuring passage of the flow) and regular cellular distribution with definite morphology (allowing for the prediction of pore and cell sizes, foam rigidity, heat transfer characteristics, etc.). One potential structure is the diamond lattice, shown in Figure 2.4. This structure has been previously studied in the LAMSI laboratory at École de technologie supérieure. The advantage of using such a structure is that it offers favourable mechanical resistance (B. Jetté, V. Brailovski, M. Dumas, C. Simoneau, & P. Terriault, 2018) and is easy to produce using 3D printing. AM, or 3D printing, has significantly evolved in recent years and has matured enough as a technology to be used for complex engineering tasks (B. P. Conner et al., 2014). We were able to generate the structure using a MATLAB script written by M. Dumas (2016), while having the entire control on the geometrical parameters (strut size, cell size, etc.).

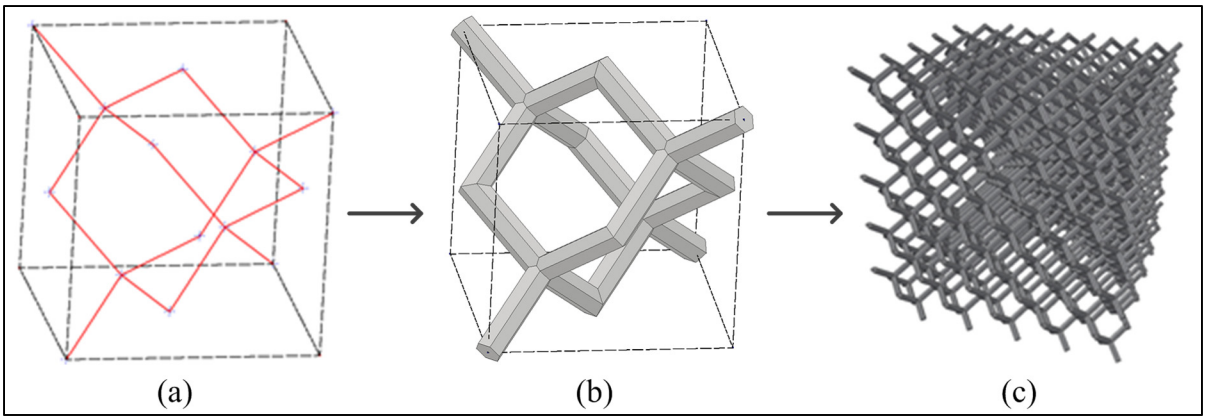

Figure 2.4 Diamond: (a) Unit cell structure;
(b) Unit cell with struts; (c) Lattice
Adapted from M. Dumas et al. (2017)

An appropriate *material* for PMB should possess high operational temperature ($T_{max,op}$) as well as high thermal shock resistance (R) and fracture toughness (K_{1C}), which inevitably turns our attention towards metals and metallic alloys.

From a *manufacturing* point of view, this geometry should be fabricated in complex shapes with high precision, which we can do using a 3D printer. As a result, we selected the metal alloy EOS CobaltChrome MP1 (CoCr), that allowed us to 3D print a diamond lattice by means of EOSINT M280 (LPBF technology) with high precision (±50 μm), high $T_{max,op}$ (1150 ℃), and superior R and K_{1C}, when compared to SiSiC (see Table 2.1). The reported material properties were taken from data sheets (EngiCer; EOS, 2011) and open sources ("CeramTec Rocar® SiF Silicon Carbide, SiSiC," 2018). CoCr, as a material, has promising characteristics, especially for use in the upstream section due to its low thermal conductivity (A. J. Barra et al., 2003) and high temperature limit (taking into consideration that the upstream section plays the role of the preheater and is not susceptible to the extreme temperatures found in the downstream region).

Table 2.1 SiSiC versus EOS CobaltChrome MP1 (CoCr), parameters of bulk materials

Parameter	Value	
	SiSiC	**CoCr**
Density, ρ $[g/cm^3]$	2.8	8.3
Maximum operational temperature, $T_{max,op}$ [°C]	1400	1150
Thermal conductivity (20 °C), k $[W/(m{\cdot}K)]$	110	13
Thermal conductivity (1000 °C), k $[W/(m{\cdot}K)]$	42	33
Thermal expansion coefficient, α_t $[\mu m/(m{\cdot}K)]$	4.8	14.4
Tensile strength, σ_t $[MPa]$	210	1100
Young's modulus, E $[GPa]$	270	200
Poisson's ratio, ν	0.17	0.29
Thermal shock resistance parameter, R $[K]$	150[a)]	271[a)]
Fracture toughness, K_{IC} $[MPa{\cdot}m^{1/2}]$	2.5[b)]	100[c)]

a) See Eqn. (1.14).
b) (Z. Fu, L. Schlier, N. Travitzky, & P. Greil, 2013)
c) (E. Ahearne, S. Baron, S. Keaveney, & G. Byrne, 2015)

2.1.3 Definition of the experimental setups

From our survey of the literature, a two-staged radial PMB configuration with a foam of high PPI in the upstream section (acting as flame arrestor) and low PPI in the downstream section (acting as flame support) was the most commonly investigated design and, as a result, was chosen in the current work. To conduct our research, we selected six experimental setups which are illustrated in Figure 2.5.

Setup #1 is considered a reference, and is commonly seen in the literature as a representation of two ceramic foams in the upstream and downstream regions. Setup #2 allowed us to investigate how using metal material (CoCr) instead of ceramics influenced the burning parameters. In setup #3, the same metal material was used, however reticulated foam was replaced by a diamond lattice. Setup #3 allowed us to understand the influence of the pore organization (ordered or random) on combustion. Finally, setups #4, #5, and #6 represent various arrangements of metal/ceramic materials and random/regular pore geometries in the downstream and upstream sections.

To implement this experimental plan, 10 PPI (large pores) and 60 PPI (small pores) SiSiC foams with the same overall dimensions were obtained from EngiCer.

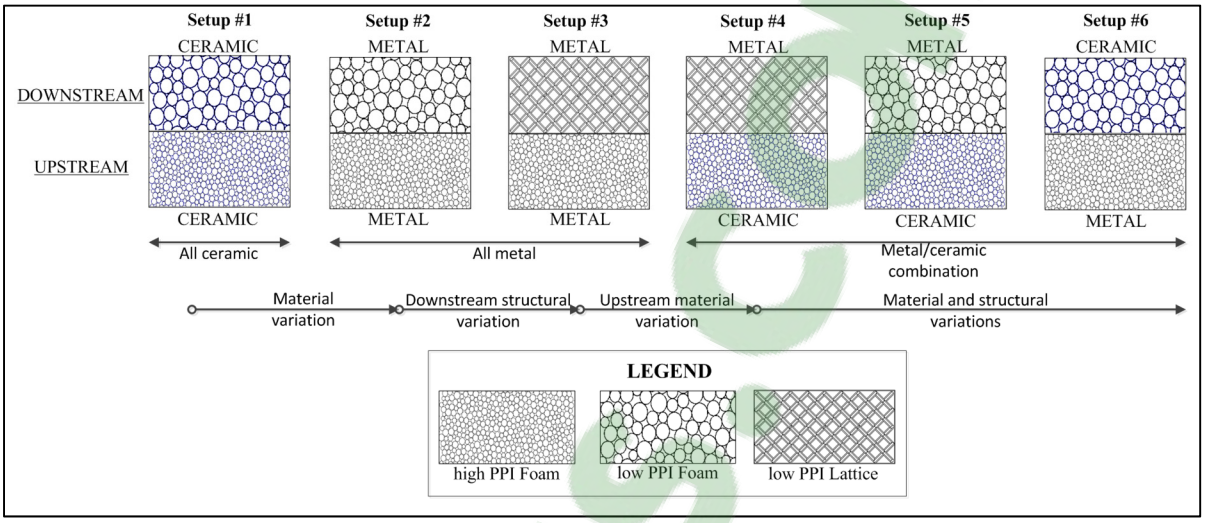

Figure 2.5 Tree of experimental setups

Finally, 30 PPI SiSiC foam was obtained from the same manufacturer to study in greater detail the influence of pore density (PPI) on foam morphology. Note that each foam type was acquired in a set of two pieces to study discrepancies among samples with identical PPI.

2.2 Analysis of ceramic foams

2.2.1 X-ray Computed Tomography (CT)

It is necessary to precisely determine the foam's geometry to predict combustion processes in the medium and to develop numerical models based on experimental data. The structural irregularities of ceramic foams make them difficult to reconstruct with conventional computer aided design (CAD) tools. Thus, using an approach that allows us to obtain accurate foam geometry is necessary to achieve accurate results. For this task, we chose X-ray Computed Tomography (CT), representing a non-destructive form of geometric analysis. A CT scan takes a series of X-ray measurements of a given object under various angles and

combines the results into cross-sectional images (an image stack) with the further possibility of recreating the object's volume (S. L. Wellington & H. J. Vinegar, 1987).

The main steps undertaken during CT scan of foam specimens are described below:

1) The specimen was installed into Nikon XT H 225 X-ray μ-CT system (Nikon, Brighton, MI, USA). Data was obtained with 220 kV tube voltage and 350 μA current, and complemented with a 1 mm-thick copper filter.
2) Obtained volume was reconstructed using the CT Pro 3D software (Nikon, Brighton, MI, USA) and a stack of image slices was obtained for each foam.
3) The image stack was imported afterwards into VG Studio MAX 3.0 (VG) software (GmbH Volume Graphics, 2016). Surface, based on the greyscale threshold, was determined and the volume was recreated.

Figure 2.6 shows a comparison between "As received" and "Digitally reconstructed" states for foams of each PPI type. As was mentioned earlier, each foam's PPI had two specimens, and these were marked as #1 and #2, respectively. However, in this work, the graphical representation of results will be provided for specimens marked as #1 only.

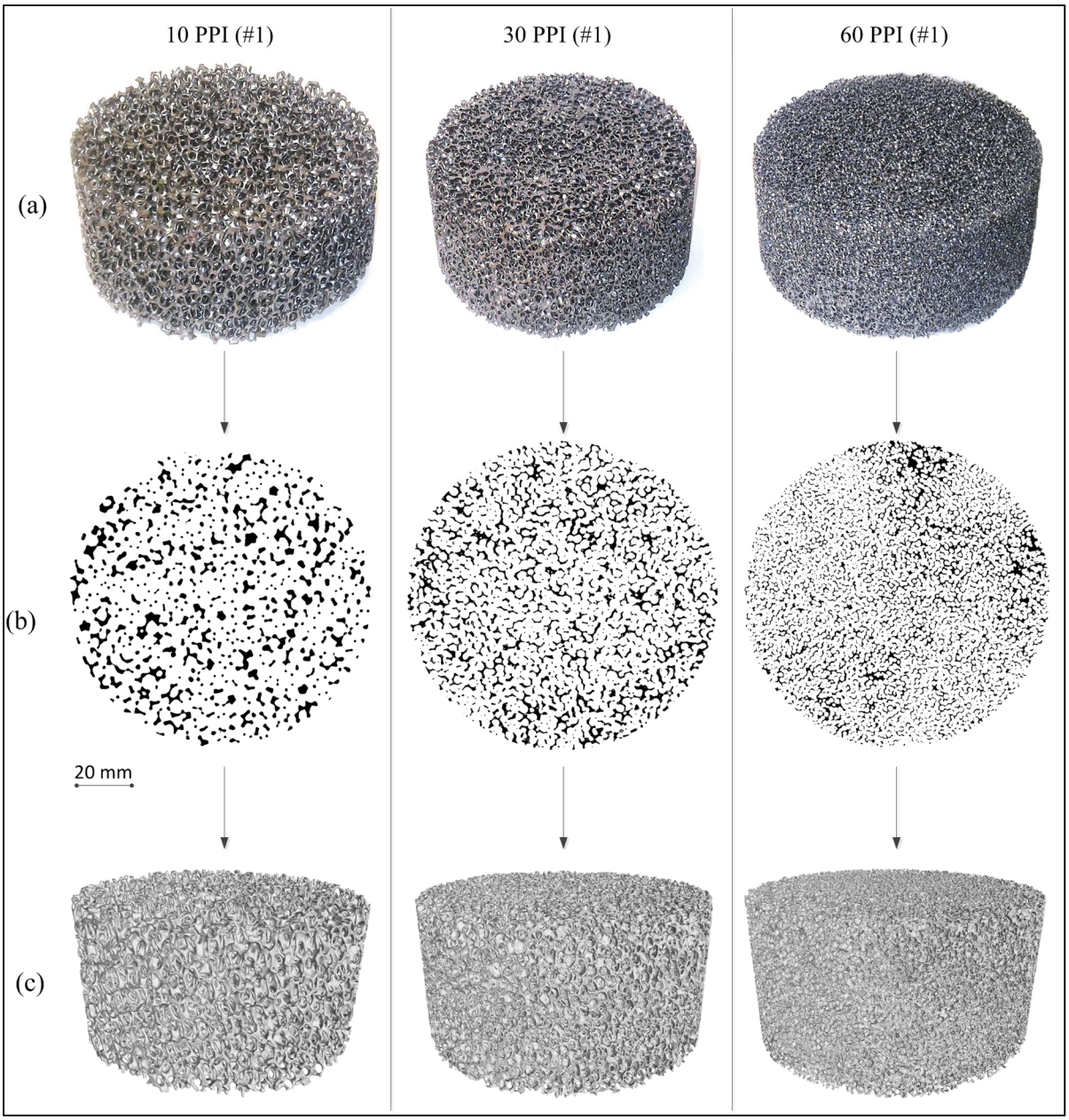

Figure 2.6 Ceramic foams: (a) As received; (b) Typical cross-section image slice; (c) Digitally reconstructed volume

2.2.2 Geometric analysis

The importance of foam geometric analysis is dictated by the necessity to predict combustion processes in the medium. Two of the main parameters influencing the burner's performance

are pore diameter (d_p) and porosity (ε) (A. P. Horsman, 2010). Moreover, selection of a suitable d_p plays an important role in stable combustion regimes and in the safety of the equipment by preventing flashback towards the inlet section. Additionally, d_p and ε play an important role in characterizing the flow passage through the medium, which might be expressed in terms of permeability (κ_{perm}) (W. Xu, H. Zhang, Z. Yang, & J. Zhang, 2008).

Therefore, it is reasonable to find a relationship between geometry and fluid flow. Based on the cross-sectional image stack obtained by CT scan and volume re-creation, it is possible to investigate the influence of structural parameters (ε, and d_p) on flow characteristics (κ_{perm}).

The current section examines methods of porosity (ε) analysis based on the Archimedes' principle and on the 3D volume re-creation in VG. Different cell size (d_c) determination techniques are presented which, in combination with the tetrakaidecahedron model (L. J. Gibson & M. F. Ashby, 1997), allows for the calculation of the foam's pore diameter (d_p). Absolute permeability analysis ($\kappa_{perm,f}$) was provided in VG and compared with d_p. Values for these parameters were obtained through different methods.

2.2.2.1 Porosity analyses

The following methods were concurrently used for porosity analysis (ε):

1) Archimedes' principle;
2) 3D analysis of volumes in VG;
3) 2D analysis of cross-section slices in MATLAB.

Archimedes' principle

Porosity, by definition, is the ratio of the void fracture to the total volume under study:

$$\varepsilon = \frac{V_{void}}{V_{tot}} = 1 - \frac{V_s}{V_{tot}} \tag{2.1}$$

where V_{void} represents the volume of the void part; V_s represents the volume of the solid part; $V_{tot} = V_{void} + V_s$ represents the total volume under study.

First, we made an attempt to determine porosity by using Archimedes' principle (B962-15 ASTM, 2015). Total porosity ($\varepsilon_{Ar,tot}$) of any part might consist of both open ($\varepsilon_{Ar,op}$) and closed ($\varepsilon_{Ar,cl}$) states:

$$\varepsilon_{Ar,tot} = \varepsilon_{Ar,op} + \varepsilon_{Ar,cl} \tag{2.2}$$

From the examination of image slices, the closed porosity of foams ($\varepsilon_{Ar,cl}$) was small and for simplicity of analysis assumed to be zero. Thus, it was taken that $\varepsilon_{Ar,tot} = \varepsilon_{Ar,op}$.

To find porosity using Archimedes' principle, we chose water as the penetrating medium. From the above-mentioned assumptions, porosity using Archimedes' principle was found as:

$$\varepsilon_{Ar,tot} = 1 - \frac{V_{s+cl.p}}{V_{tot}} \tag{2.3}$$

where $V_{s+cl.p}$ is the volume of the solid with closed pores found as:

$$V_{s+cl.p} = \frac{m_{air} - m_w}{\rho_w} \tag{2.4}$$

where m_{air} and m_w are the masses of the specimen weighed in air and water, respectively, and ρ_w is the density of water.

As a result, the apparent specimen's density might be found as:

$$\rho_{app} = \frac{m_{air}}{V_{s+cl.p}} \tag{2.5}$$

To obtain weight measurements, we used the OHAUS Adventurer Pro AV313 scale, and our results are presented in Table 2.2. During the experiments, we found that it was difficult to

obtain complete water penetration for specimens with high pore densities (30 PPI and 60 PPI), which resulted in underestimated values. We obtained corrected values through volume re-creation using VGStudio Max 3.0 software, which is described in the following subsection.

Table 2.2 Results of measurements using Archimedes' principle

Pore Size	**10 PPI**		**30 PPI**		**60 PPI**	
Specimen	**#1**	**#2**	**#1**	**#2**	**#1**	**#2**
m_{air}, $[g]$	165.0	173.5	212.2	287.2	140.1	121.3
m_w, $[g]$	104.7	110.2	128.1	163.2	72.2	63.8
ρ_{app}, $[g/cm^3]$	2.73	2.74	2.52	2.31	2.06	2.10
$\varepsilon_{Ar,tot}$, $[\%]$	85.3	84.6	79.5	69.8	83.5	86.0

VGStudio Max 3.0 (3D analysis)

To evaluate the porosity of foams with high PPI, for which the application of Archimedes' principle failed, VGStudio Max 3.0 software (VG) was employed to analyze the reconstructed volumes from the CT scan data. During reconstruction, there were two main parameters that influenced the final 3D model: "Pixel resolution" and "grey threshold" value. Pixel resolution is a scaling factor, defined during the generation of the image stack or calculated from a cross-section image as the ratio of known physical length to its length in pixels. Each pixel of the greyscale image has its value, and by applying a given grey threshold, the pixel's domain becomes separated on the void and solid phases. Application of "pixel resolution" and "grey threshold" values result in volume recreation with correct overall dimensions and creates a correctly reconstructed shape.

To accurately apply grey threshold, porosity should be a known parameter. One method to properly apply grey threshold is to use the previously described Archimedes' principle and compare its porosity calculation ($\varepsilon_{Ar,tot}$) with the porosity of the digitally reconstructed part (ε_{rec}). If porosities in both cases are equal, then the grey threshold has been applied correctly (see Figure 2.7).

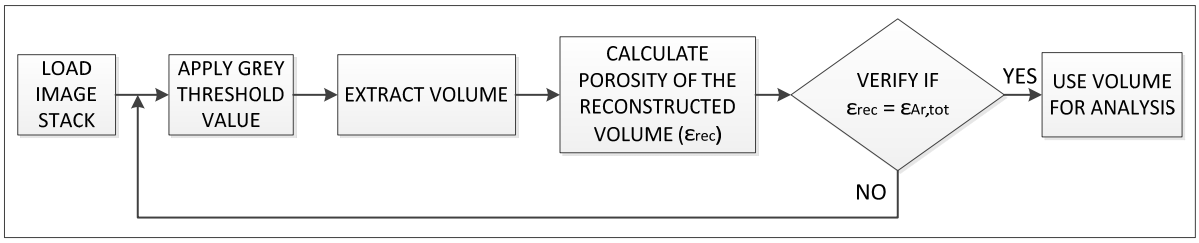

Figure 2.7 Adjusting grey threshold to an image stack

To conduct our analysis, we prepared image stacks of the foam specimens (675 cross-sections each, resolution 0.06919 mm/pixel). The number of image slices corresponded to corrected height ($H_{corr} = 46.7\ mm$), which was lower than actual, or unadjusted, height ($H = 50.8\ mm$). Specimen edges that were out of focus after a CT scan were cropped. For the following calculations, corrected masses were used ($m_{air,corr} = H_{corr}/H \cdot m_{air}$). First, the 10 PPI (#1) sample was analyzed in VG. Grey threshold value was chosen as the mean value from the presented grey threshold histogram in VG. Determined surface (S_{surf}), provided distinct fit according to material contours from image slices. After the specimen's reconstruction and volume determination (V_s), foam density was evaluated ($\rho_f = m_{air,corr}/V_s$) as well as porosity ($\varepsilon_{tot,VG}$) (see Eqn. (2.1)). Results of these analyses are presented in Table 2.3.

Table 2.3 Parameters of reconstructed solids in VG

Pore Size	**10 PPI**		**30 PPI**		**60 PPI**	
Specimen	**#1**	**#2**	**#1**	**#2**	**#1**	**#2**
$m_{air,corr}$, $[g]$	150.8	159.5	195.1	264.0	128.8	111.6
ρ_f, $[g/cm^3]$	2.80					
Greyscale threshold	21876	20165	25407	24494	20229	12567
$V_s \cdot 10^{-4}$, $[mm^3]$	5.38	5.69	6.96	9.42	4.59	3.98
$S_{surf} \cdot 10^{-5}$, $[mm^2]$	2.01	1.94	3.60	3.60	4.55	4.06
$\varepsilon_{tot,VG}$, $[\%]$	85.8	85.0	81.6	75.1	87.9	89.5

The porosity for 10 PPI #1 foam obtained by VG ($\varepsilon_{tot,VG} = 85.8\%$, see Table 2.3) was in agreement with Archimedes' principle ($\varepsilon_{Ar,tot} = 85.3\%$, see Table 2.2). Discrepancies in the results are due the fact that applied Archimedes' principle does not account for closed pores,

which were detected in small amount for 10 PPI specimens from image slices. Eventually, it was decided to use the reconstructed volume of the 10 PPI (#1) foam with $\varepsilon_{tot,VG} = 85.8\%$. The specimen's density (ρ_f) was found to be 2.8 g/cm^3, which was in excellent agreement with what was indicated by the manufacturer (see Table 2.1).

During volume reconstruction of the other specimens, obtained ρ_f was considered constant. By knowing the masses of each specimen, target volumes were calculated according to the relationship $m_1/m_2 = V_1/V_2$, where m_1 and V_1 corresponded to values for the 10 PPI (#1) foam specimen and m_2, V_2 for the target part. After determining target volumes for all other specimens, we adjusted appropriate grey threshold values and calculated corresponding porosities.

Cross-section slices (2D analysis)

Porosities of cross-section slices (ε_{cs}) were evaluated primarily for comparative analysis with $\varepsilon_{tot,VG}$. The same image stacks used for volume reconstruction were binarized (converted into black and white images) with the same grey threshold values by means of the image-processing software Fiji (J. Schindelin et al., 2012). Afterwards, a MATLAB script was written to treat each image stack and to calculate the corresponding mean porosities. Table 2.4 summarizes the porosity values obtained by different methods. Archimedes' principle ($\varepsilon_{Ar,tot}$) was useful for only 10 PPI specimens with large pores, whereas for 30 PPI and 60 PPI samples it provided slightly underestimated values. The obtained values of ε_{cs} provided slightly underestimated values in comparison to volumetric porosity ($\varepsilon_{tot,VG}$), but were in the range of reasonable discrepancy. Finally, for further analysis, values of porosity obtained in VG ($\varepsilon_{tot,VG}$) were taken as a reference.

Table 2.4 Results of porosity analysis by different methods
(shaded is the selected set of values)

Method	Pore Size	10 PPI		30 PPI		60 PPI	
	Specimen	#1	#2	#1	#2	#1	#2
Archimedes'	$\varepsilon_{Ar,tot}$, [%]	85.3	84.6	79.5	69.8	83.5	86.0
VGStudio 3D	$\varepsilon_{tot,VG}$, [%]	85.8	85.0	81.6	75.1	87.9	89.5
MATLAB 2D	ε_{cs}, [%]	85.6	84.8	81.4	75.0	87.6	89.2

2.2.2.2 Cell and pore diameter analyses

The following methods were used to determine cell diameters (d_c):

1) 2D analysis of cross-sections by the watershed method;
2) 3D analysis of reconstructed volumes in VG by the watershed method;
3) A method of maximal inscribed spheres using VG;
4) 2D cross-sectional analysis based on ASTM D3576-15.

Values of d_c were then used to determine pore diameters (d_p) based on the tetrakaidecahedron model (L. J. Gibson & M. F. Ashby, 1997) (see APPENDIX I, p. 95 for more details).

Watershed method (2D analysis)

One approach used to determine a foam's cell size, which is widely used, is watershed segmentation (A. P. Mangan & R. T. Whitaker, 1999). This method uses the analogy of a geological watershed and applies it to foam, transforming an image into a topographic map with corresponding basins and peaks (see Figure 2.8). The main steps of the watershed image segmentation technique are shown in Figure 2.9. The initial image (Figure 2.9, a) is transformed into a map (Figure 2.9, b) that represents the distance from each void pixel (white) to the nearest material pixel (black), and the obtained distances are interpreted as geological depth. Afterwards, the pixels are filled from most to least deep. When corresponding "flows" from various basins meet, dividing watershed lines are created,

forming segmented cells (see Figure 2.9, c). The initial material is then added, and the area of each cell (A_c) is calculated (see Figure 2.9, d). By using the described principle, we applied watershed segmentation for each image stack by writing a MATLAB script.

For the evaluation of cell diameters ($d_{c_{w,2D}}$), cell areas were considered to be of a circular shape:

$$d_{c_{w,2D}} = \sqrt{4A_c/\pi} \tag{2.6}$$

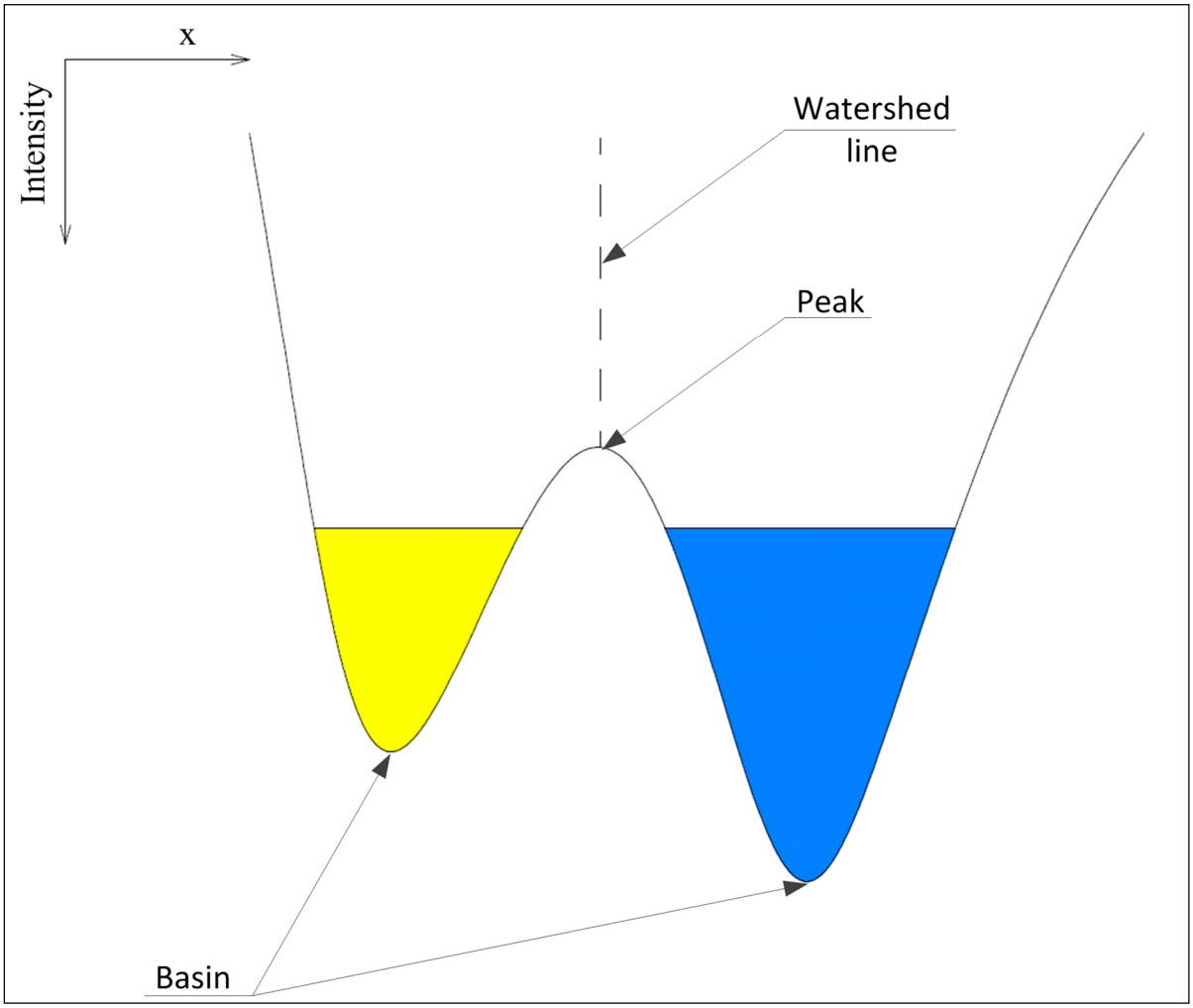

Figure 2.8 Principles of watershed segmentation
Adapted from A. Videla, C.-L. Lin, and J. D. Miller (2006)

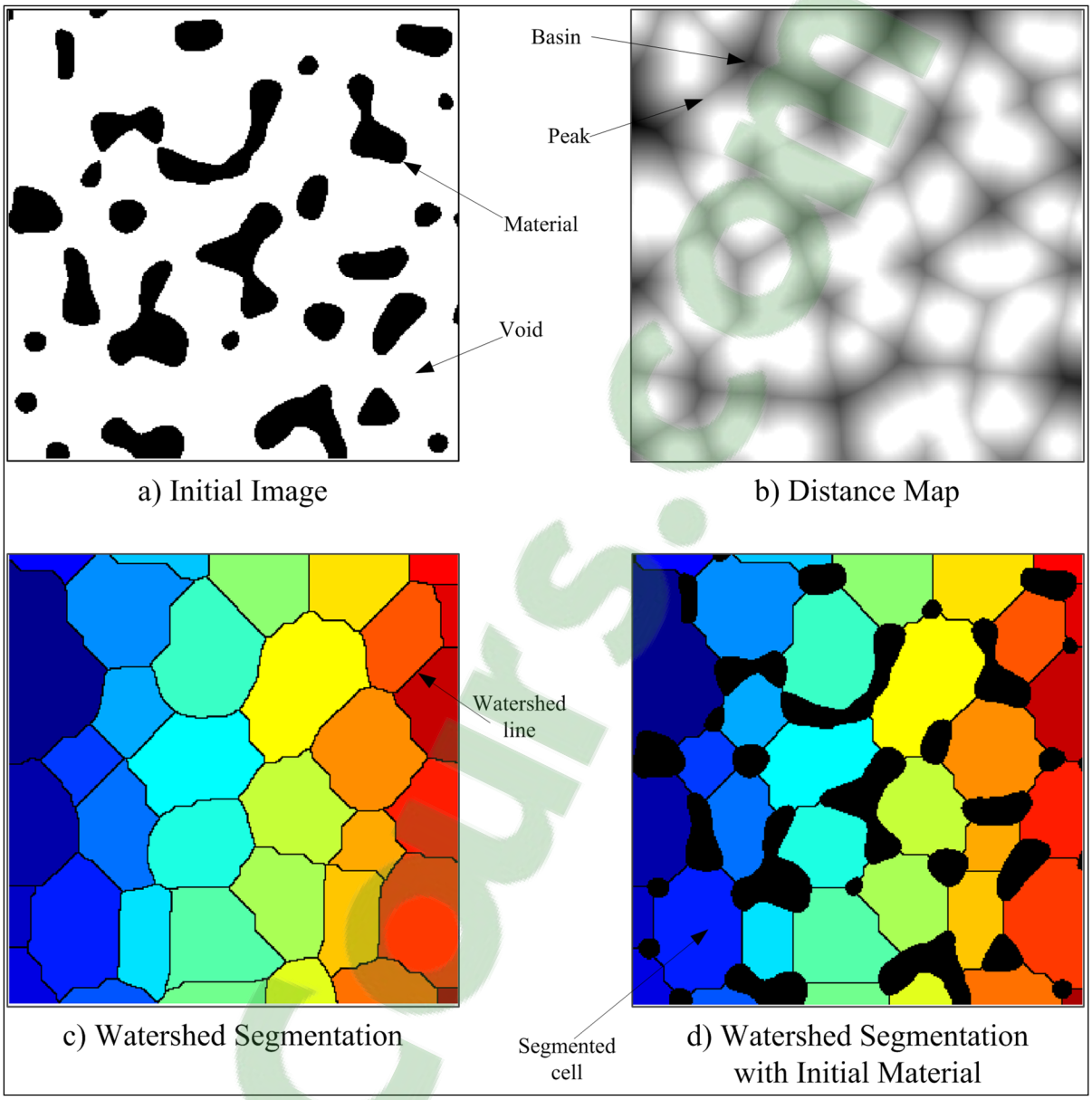

Figure 2.9 Watershed 2D segmentation:
MATLAB script (10 PPI #1 foam)

After analysis, we created distribution histograms of $d_{c_{w,2D}}$ for #1 specimens (see Figure 2.10). From the histograms, we can see that with an increase in PPI, cell size distribution becomes narrower and more homogeneous, which agrees with results obtained by F. Eichhorn et al. (2017).

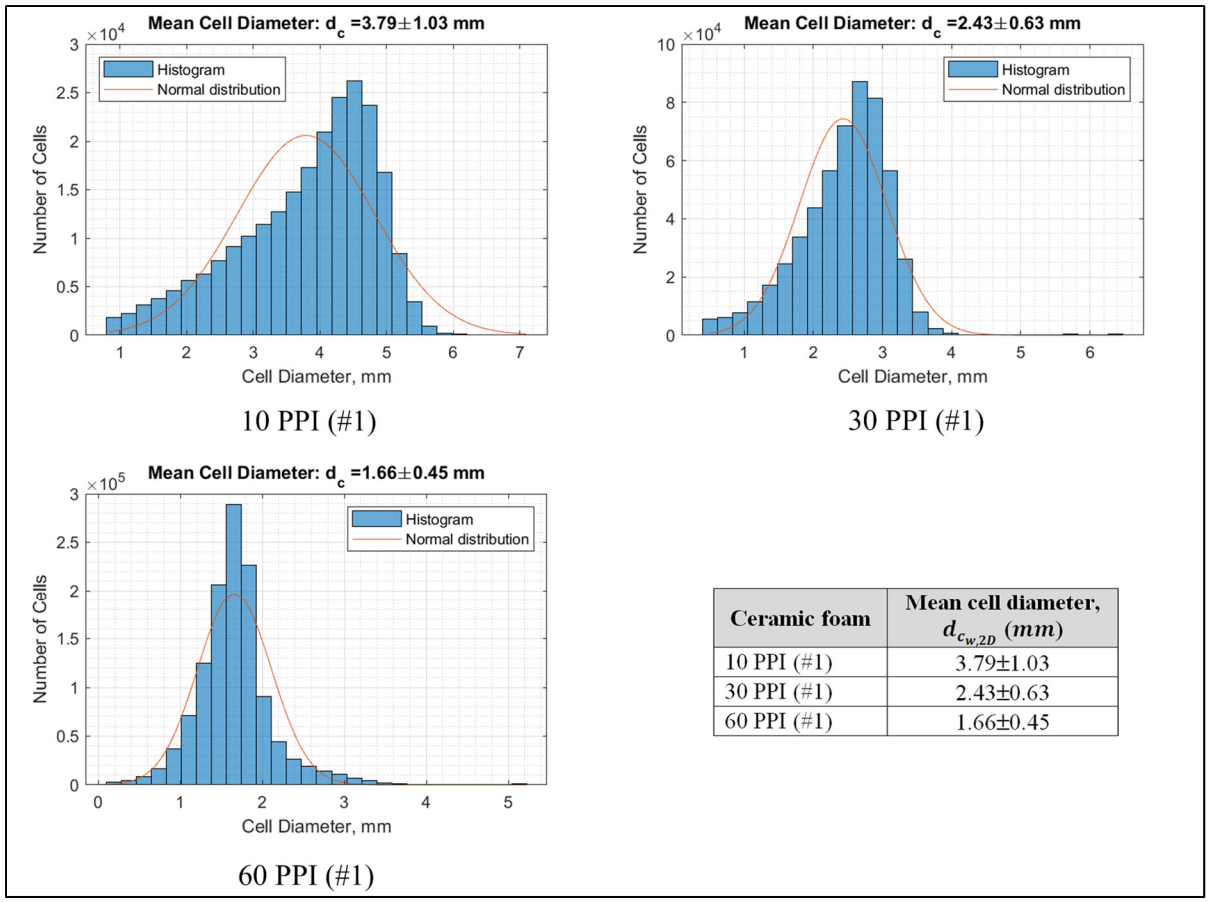

Ceramic foam	Mean cell diameter, $d_{c_{w,2D}}$ (mm)
10 PPI (#1)	3.79±1.03
30 PPI (#1)	2.43±0.63
60 PPI (#1)	1.66±0.45

Figure 2.10 Watershed 2D analysis:
Cell diameter distribution histograms, $d_{c_{w,2D}}$ (specimens #1)

The mean values of $d_{c_{w,2D}}$ for #1 and #2 specimens are shown in Table 2.5.

Table 2.5 Results of watershed method (2D analysis)

Parameter	10 PPI		30 PPI		60 PPI	
	#1	#2	#1	#2	#1	#2
$d_{c_{w,2D}}$, $[mm]$	3.79	4.03	2.43	2.32	1.66	1.67

VGStudio Max 3.0: Watershed method (3D analysis)

The "Foam Structure Analysis" module of the VG software uses a more sophisticated approach to provide 3D watershed segmentation (A. Videla et al., 2006). This is similar to

the previously described technique applied for 2D images, where pixels are replaced by their 3D volumetric analogues, voxels. VG creates a distance map from each void voxel (the 3D equivalent of a 2D pixel) to the nearest material voxel. The farther a void voxel is located, the deeper it lies within the "watershed." Like the method for 2D segmentation, void voxels are filled from most to least deep, until the corresponding cell volumes meet and watershed segmentation occurs. The software visualizes (see Figure 2.11) and provides detailed information about each cell that is found (volume, surface area, etc.).

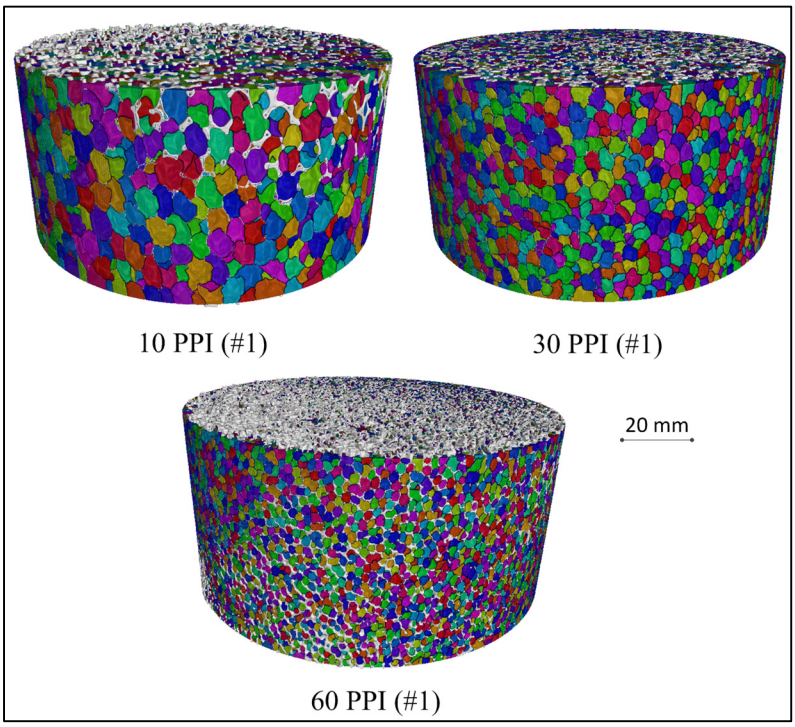

Figure 2.11 Watershed 3D segmentation:
VG "Foam Structure Analysis" (specimens #1)

If we consider the cell volume (V_c) as a sphere, then cell diameter ($d_{c_{w,3D}}$) might be found as:

$$d_{c_{w,3D}} = \sqrt[3]{6V_c/\pi} \tag{2.7}$$

Another approach is to consider cells as spheres with known volume (V_c) and outer surface (S_{surf}) which leads to equivalent cell diameter (S. Liu, A. Afacan, & J. Masliyah, 1994), that is defined as:

$$d_{c_{w,3D,surf}} = 6\frac{V_c}{S_{surf}} \tag{2.8}$$

After the "Foam Structure Analysis," we collected information on each cell volume (V_c) and outer surface (S_{surf}). From this, we created distribution histograms of $d_{c_{w,3D}}$ for #1 specimens (see Figure 2.12).

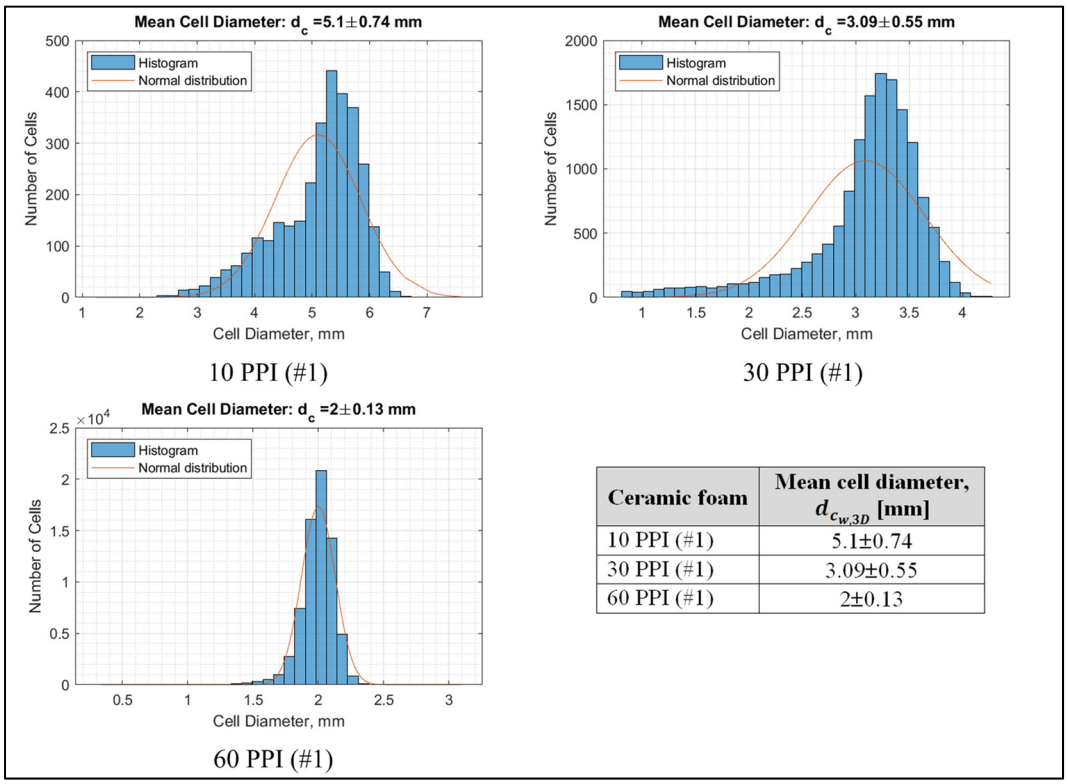

Ceramic foam	Mean cell diameter, $d_{c_{w,3D}}$ [mm]
10 PPI (#1)	5.1±0.74
30 PPI (#1)	3.09±0.55
60 PPI (#1)	2±0.13

Figure 2.12 Watershed 3D analysis:
Cell diameter distribution histograms, $d_{c_{w,3D}}$ (specimens #1)

The distribution histograms were typical for $d_{c_{w,3D}}$ and $d_{c_{w,3D,surf}}$ methods. However, the second approach ($d_{c_{w,3D,surf}}$) provided lower values of cell diameters, as it took into account cell shape irregularities. Irregularities can be characterized by sphericity (Ψ), which

demonstrates how closely the shape of an object approaches the shape of the sphere, and is found as:

$$\Psi = \frac{\pi^{\frac{1}{3}}(6V_c)^{\frac{2}{3}}}{S_{surf}} \tag{2.9}$$

From the results of sphericity (see Table 2.6) and the cell distribution histograms (see Figure 2.12), we see that with an increase in PPI, the cell's morphology approaches spherical shape and the size distribution histogram becomes more homogeneous.

The mean values of $d_{c_{w,3D}}$, $d_{c_{w,3D,surf}}$ and Ψ for #1 and #2 specimens are shown in Table 2.6.

Table 2.6 Results of watershed method (3D analysis)

Parameter	10 PPI		30 PPI		60 PPI	
	#1	#2	#1	#2	#1	#2
$d_{c_{w,3D}}$, $[mm]$	5.1	5.46	3.09	2.95	2	2.02
$d_{c_{w,3D,surf}}$, $[mm]$	4	4.28	2.47	2.39	1.69	1.72
Ψ	0.78	0.78	0.8	0.81	0.85	0.85

VGStudio Max 3.0: Maximal inscribed spheres method

The "Capillary Pressure Curve" module in VG allows for the computation of a mean cell diameter ($d_{c_{sph}}$), using the approach of maximal inscribed spheres. This approach uses spheres of various sizes as probes and inscribes them into the void space between struts until the corresponding maximal dimension is found.

We created distribution histograms of $d_{c_{sph}}$ for #1 specimens (see Figure 2.13).

From the histograms and $d_{c_{sph}}$, we noticed similarity to the results obtained with $d_{c_{w,3D,surf}}$ and a convergence with PPI increase.

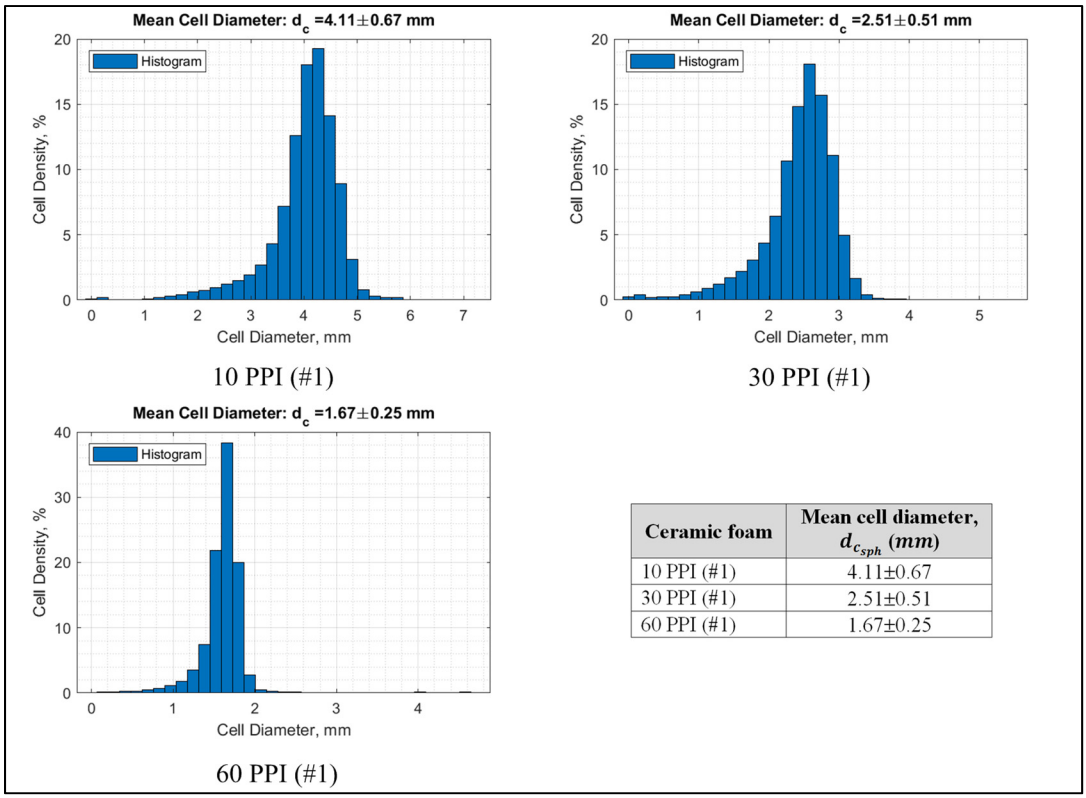

Ceramic foam	Mean cell diameter, $d_{c_{sph}}$ (mm)
10 PPI (#1)	4.11±0.67
30 PPI (#1)	2.51±0.51
60 PPI (#1)	1.67±0.25

Figure 2.13 VG Maximal inscribed spheres analysis:
Cell size distribution histograms, $d_{c_{sph}}$ (specimens #1)

The mean values of $d_{c_{sph}}$ for #1 and #2 specimens are shown in Table 2.7.

Table 2.7 Results of maximal inscribed spheres method (VG)

Parameter	10 PPI		30 PPI		60 PPI	
	#1	#2	#1	#2	#1	#2
$d_{c_{sph}}$, $[mm]$	4.11	4.45	2.51	2.35	1.67	1.69

Analysis of image cross sections based on ASTM D3576-15

Cross-sectional analysis, which is based on the standard D3576-15 ASTM (2015), is another method that can be applied to characterize foams. This standard was developed to determine the cell sizes of rigid plastics, which are used as templates in the production of ceramic foams. In this method, slices are analyzed by evaluating the average chord length (t_{ASTM})

found as the division of randomly drawn reference line length (l_{ref}) by the number of intersections with walls (n_{int}):

$$t_{ASTM} = \frac{l_{ref}}{n_{int}} \tag{2.10}$$

Finally, the value of the cell size ($d_{c,ASTM}$) is proposed to be found based on the relatively uniform distribution of cells with spherical shape:

$$d_{c,ASTM} = t_{ASTM}(1.623) \tag{2.11}$$

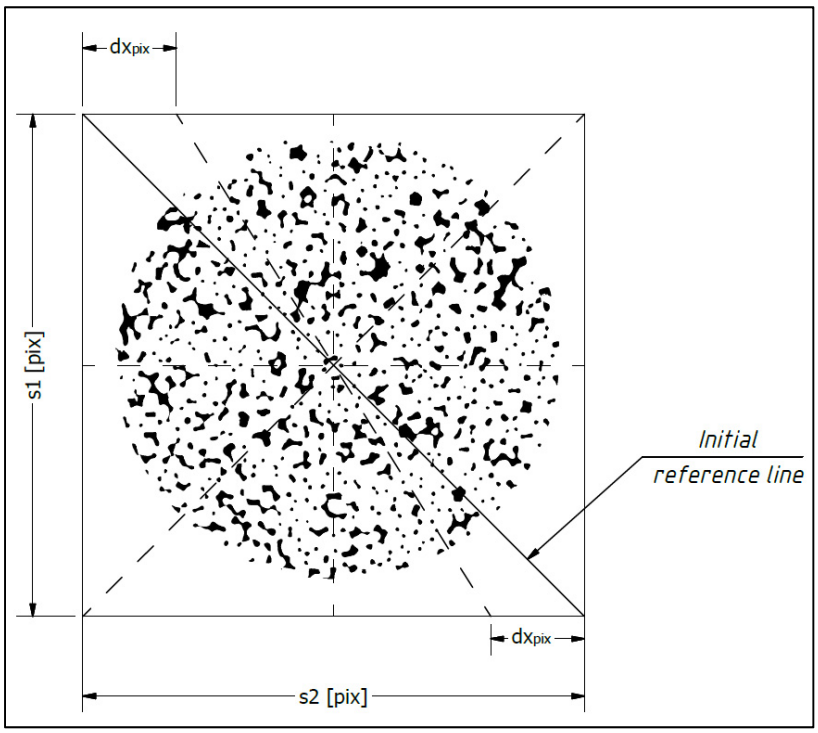

Figure 2.14 Determination of $d_{c,ASTM}$
according to D3576-15 ASTM (2015) (10 PPI #1 foam)

The MATLAB script was written such that for specific cross-section images with $s_1 x s_2$ pixels, a number of intersections with struts (n_{int}) and corresponding mean strut thickness (t_s) can be calculated by drawing a reference line (one pixel thick) passing through the disk's

centre (see Figure 2.14). We repeated the operation of drawing a reference line through rotation, according to the disk's centre, in consecutive increments of one pixel at the image border (dx_{pix}) until finally the whole image had been covered. The total number of reference lines is represented by $N_{tot,rl} = s1 + s2 - 2$ (for investigated images, it corresponded to ≈ 3000 reference lines per slice). By applying this approach to each image stack of foam specimens, we calculated the corresponding values of n_{int} and strut thicknesses (t_s). To calculate chord length (t_{ASTM}), reference line length (l_{ref}) was taken as the disk diameter $101.6\ mm$. We then created distribution histograms of $d_{c,ASTM}$ for #1 specimens (see Figure 2.15). The mean values of $d_{c,ASTM}$ for #1 and #2 specimens are shown in Table 2.8.

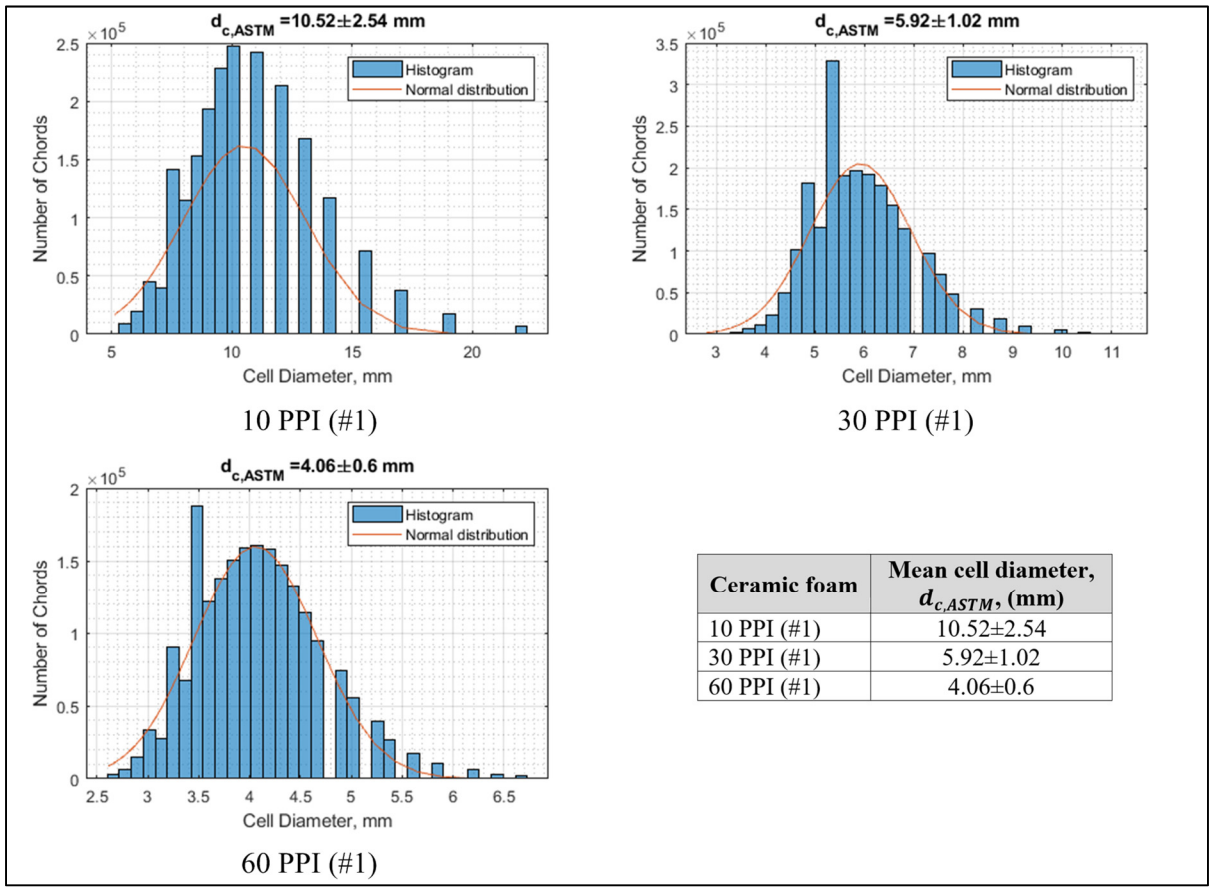

Ceramic foam	Mean cell diameter, $d_{c,ASTM}$, (mm)
10 PPI (#1)	10.52±2.54
30 PPI (#1)	5.92±1.02
60 PPI (#1)	4.06±0.6

Figure 2.15 Cross-sectional 2D analysis according to D3576-15 ASTM (2015): Cell diameter distribution histograms, d_c (specimens #1)

Table 2.8 Results of cross-sectional 2D analysis
(D3576-15 ASTM, 2015)

Parameter	10 PPI		30 PPI		60 PPI	
	#1	#2	#1	#2	#1	#2
n_{int}	15.64	14.77	27.8	28.15	40.49	36.88
t_s, $[mm]$	0.94	0.97	0.69	0.91	0.42	0.39
t_{ASTM}, $[mm]$	6.48	6.87	3.65	3.6	2.5	2.75
$d_{c,ASTM}$, $[mm]$	10.52	11.14	5.92	5.85	4.06	4.46
$d_{c_{cs}}$, $[mm]$	5.54	5.9	2.96	2.69	2.08	2.36

The calculated $d_{c,ASTM}$ greatly exceeded the values that were calculated through previously described methods (see Table 2.5, Table 2.6, Table 2.7). This was attributed to the corrective coefficient 1.623, which was derived for the sphere packing case. As well, the D3576-15 ASTM (2015) standard does not specify a required thickness for cross-section slices during measurements. As was noted by M. D.M. Innocentini, V. R. Salvini, A. Macedo, and V. C. Pandolfelli (1999), CT-scan images omit cell edges in thin planes, which results in overestimated values. Therefore, cross-section cell diameter ($d_{c_{cs}}$) should be similar to chord length (t_{ASTM}). Additionally, to evaluate $d_{c_{cs}}$, we had to consider strut thickness (t_s):

$$d_{c_{cs}} = \frac{l_{ref} - n_{int} \cdot t_s}{n_{int}} = t_{ASTM} - t_s \tag{2.12}$$

Here, values of $d_{c_{cs}}$ (see Table 2.8) demonstrated a better correlation with the previous methods used. All the results (except $d_{c,ASTM}$) are presented in Table 2.9.

Table 2.9 Cell diameters (d_c): Comparison between different methods

Applied method	10 PPI		30 PPI		60 PPI	
	#1	#2	#1	#2	#1	#2
Porosity, ε [%]						
VGStudio Max 3.0	85.8	85.0	81.6	75.1	87.9	89.5
Cell diameter, d_c [mm]						
Watershed (2D): $d_{c_{w,2D}}$	3.79	4.03	2.43	2.32	1.66	1.67
Watershed (3D): $d_{c_{w,3D}}$	5.10	5.46	3.09	2.95	2.00	2.02
Watershed (3D): $d_{c_{w,3D,surf}}$	4.00	4.28	2.47	2.39	1.69	1.72
Inscribed spheres: $d_{c_{sph}}$	4.11	4.45	2.51	2.35	1.67	1.69
Cross-section: $d_{c_{cs}}$	5.54	5.90	2.96	2.69	2.08	2.36

Nevertheless, from the obtained cell size results (d_c), it is difficult to determine which is the most representative method, as the manufacturer characterizes foams in terms of d_p (by providing PPI). To find the d_p of foams, L. J. Gibson and M. F. Ashby (1997) suggested replacing the *foam's* cell with a *tetrakaidecahedron* unit cell, which consists of 14 facets (8 hexagons and 6 squares) (see Figure 2.16).

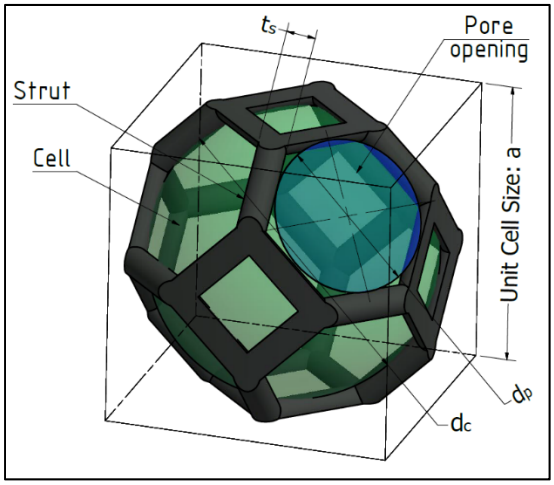

Figure 2.16 Tetrakaidecahedron unit cell

Thus, after determining mean cell sizes (d_c), the tetrakaidecahedron model was used for further evaluation of pore diameters (d_p) based on the developed correlation for the

equivalent diameter ($d_{p,eq}$) as a function of cell size and porosity (see APPENDIX I, p. 95 for detailed analysis):

$$d_{p,eq} = d_c(0.1306\varepsilon^{12.28} + 0.4114) \tag{2.13}$$

The results of $d_{p,eq}$ calculations using Table 2.9 data are presented in Table 2.10.

Table 2.10 Pore diameters (d_p): Comparison between different methods

Applied method	10 PPI		30 PPI		60 PPI	
	#1	#2	#1	#2	#1	#2
Pore diameter, d_p [mm]						
Watershed (2D): $d_{p_{w,2D}}$	1.62	1.72	1.02	0.96	0.69	0.71
Watershed (3D): $d_{p_{w,3D}}$	2.20	2.34	1.30	1.22	0.87	0.9
Watershed (3D): $d_{p_{w,3D,surf}}$	1.72	1.83	1.05	1.00	0.74	0.76
Inscribed spheres: $d_{p_{sph}}$	1.77	1.91	1.06	0.98	0.73	0.75
Cross-section: $d_{p_{cs}}$	2.39	2.53	1.25	1.12	0.91	1.05
Manual measurements in VG: $d_{p,VG}$	2.28		1.37		0.95	
Manufacturer: $d_{p_{man}}$	2.54		0.85		0.42	

Comments on the cell/pore diameters analyses

In their analysis of 2D slices, A. M. Williams, C. P. Garner, and J. G. P. Binner (2008) demonstrated that by considering cells as spheres, actual d_c can be found by dividing the average cell diameter found for 2D slices by 0.79. This value has been confirmed by comparing values between 2D and 3D watershed methods ($d_{c_{w,2D}}/d_{c_{w,3D}}$). For 10 PPI specimens, however, this factor was lower—in the range of 0.73-0.74—which was due to lower sphericity and more ellipsoidal cell geometry. It was observed that by increasing PPI, the cell's shape converged to a spherical shape and to the ratio of 0.79.

Difference in d_p among different methods reached up to 50%, which demonstrates the complexity in the analysis of ceramic foams and further uncertainty in the evaluation of

pores. By providing a comparison of our results, they can be presented in the order shown below:

$$d_{p_{w,2D}} <^{+5.6\%} d_{p_{w,3D,surf}} <^{+2.3\%} d_{p_{sph}} <^{+22.5\%} d_{p_{w,3D}} <^{+8.6\%} d_{p_{cs}}$$

The percentage values represent the average difference between the methods that were compared. The studied approaches may be further divided into two groups with result discrepancies less than 10%: "$d_{p_{w,2D}} <^{+5.6\%} d_{p_{w,3D,surf}} <^{+2.3\%} d_{p_{sph}}$" and "$d_{p_{w,3D}} <^{+8.6\%} d_{p_{cs}}$".

Other methods of cell and pore analysis that we found in the literature can be found in APPENDIX III (p. 103). By analyzing our results, we can conclude that values only correlated well for foams with low PPI (10 PPI). For higher PPI values (30 PPI and 60 PPI), various methods gave results that deviated from one another. The best convergence observed within this work was among values of $d_{p,cs}$ and J.-F. Despois and A. Mortensen (2005). However, use of the latter resulted in high discrepancies for structures with low porosity (i.e. 30 PPI #2 foam with $\varepsilon = 74.8$ %), which was rather an exception in our case.

By comparing the obtained results with the one indicated by the manufacturer ($d_{p_{man}}$), none of the forms of analysis provided good convergence for the whole PPI range. This moved us to use absolute permeability analysis to find which method of d_p determination might be chosen as characteristic for the foam's geometry.

2.2.2.3 Absolute permeability

Absolute permeability (κ_{perm}) is a medium's ability to transmit fluid through itself, and is a parameter characterized by the medium's geometry. κ_{perm} is found in the second-order Forchheimer equation, allowing definition of the pressure drop (Δp) through certain media:

$$\frac{\Delta p}{L} = \frac{\mu}{\kappa_{perm}} V + \frac{\rho F}{\sqrt{\kappa_{perm}}} V^2 \tag{2.14}$$

where μ represents the dynamic viscosity of the fluid, ρ represents the density of the fluid, V represents fluid velocity, F represents the Forchheimer coefficient, L represents the length of the medium.

The "Absolute Permeability Experiment" module in VGStudio Max 3.0 allows for the computation of permeability in the predefined volume. This method uses stationary low-Reynolds flow of an incompressible fluid through the voids of a porous material which are assumed to be completely flooded (GmbH Volume Graphics, 2016). This simulates the Stokes flow, or creeping flow, which is a simplification of the stationary Navier-Stokes equation for an incompressible fluid at low Reynolds numbers (i.e. low-flow velocity or high viscosity). According to Darcy's law, κ_{perm} is computed from the simulation result as:

$$\kappa_{perm} = V \cdot \mu \cdot L / \Delta p \tag{2.15}$$

By specifying L (found from the selected volume domain) and μ (fluid type), in the "Absolute Permeability Experiment" module of VG, there were two forms of analysis:

1) By specifying the total pressure drop (Δp), it provides results of the total flow rate ($\dot{Q}$) and recalculates it into the form of the flow speed (V) for each cross-section;
2) By specifying the total flow rate ($\dot{Q}$), it is recalculated into the form of the flow speed (V) for each cross-section and, finally, provides results for total pressure drop (Δp).

However, through sensitivity analysis (by varying initial conditions of Δp and $\dot{Q}$ in both cases), it was found that κ_{perm} is the geometry-only dependent parameter. The absolute permeability results of the foams $\kappa_{perm,f}$ are presented in Table 2.11.

Table 2.11 Absolute permeability of foams ($\kappa_{perm,f}$)

Parameter	10 PPI		30 PPI		60 PPI	
	#1	#2	#1	#2	#1	#2
$\kappa_{perm,f}$, $[10^8 \cdot m^2]$	30.83	32.68	9.97	7.73	4.39	6.13

Based on the notion that κ_{perm} is a geometric characteristic, it is of interest to find its dependence on geometric parameters (ε, d_p). We analyzed the dependence of $\kappa_{perm,f}$ on the provided PPI values (see Figure 2.17) and compared it with the $\kappa_{perm}(PPI)$ analyzed by M. D.M. Innocentini et al. (1999); J. T. Richardson et al. (2000), and K. Boomsma and D. Poulikakos (2001).

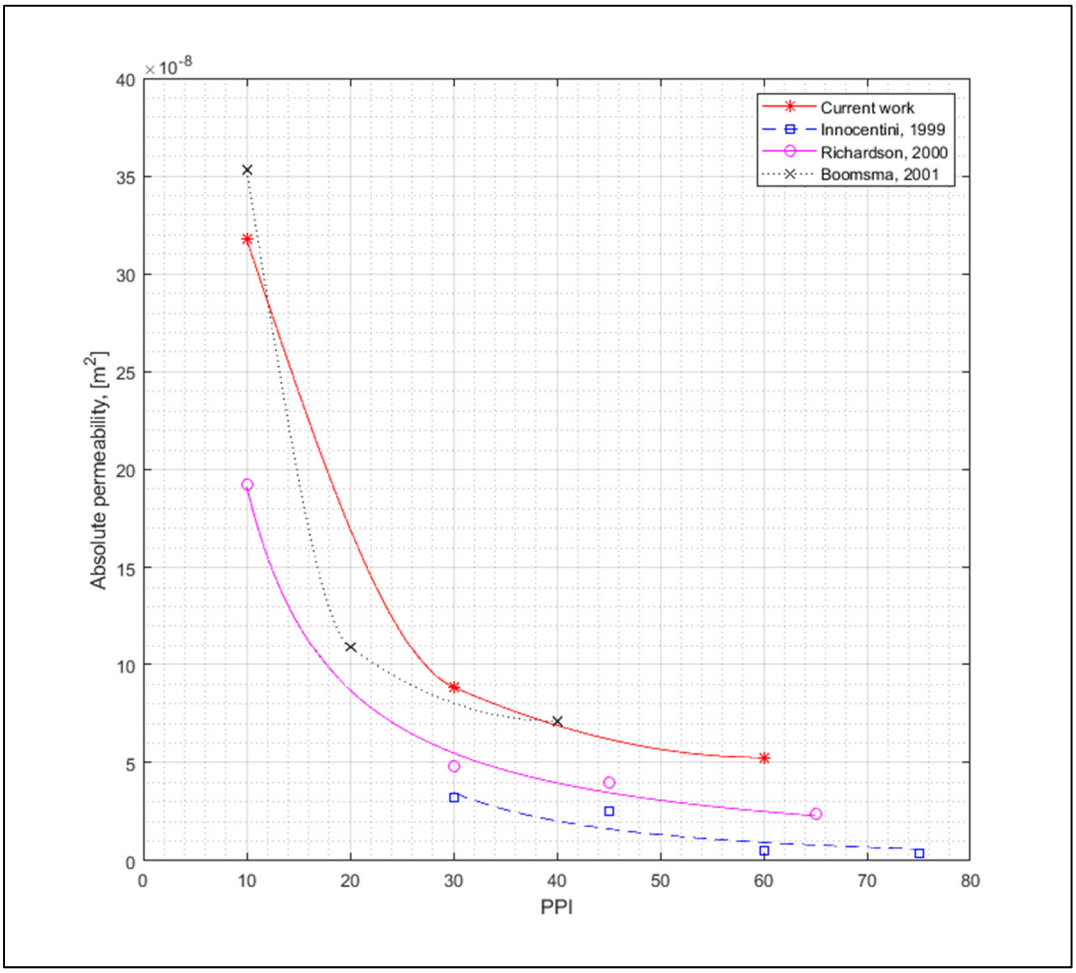

Figure 2.17 Comparison of the absolute permeability results with previous works

Generally, simulated data overpredicted the results from other works, which may be in part due to differences in foam properties (porosity, cell/pore size, etc.). However, the results were close to those found by K. Boomsma and D. Poulikakos (2001) and similar trends were observed. Thus, the method of κ_{perm} analysis provided by VG software can be considered applicable for comparative study between various geometries.

Afterwards, dependence of $\kappa_{perm,f}$ on the calculated pore diameters (see Table 2.10) was investigated (see Figure 2.18). As can be seen from Figure 2.18 the best fit for prediction of $\kappa_{perm,f}$ in the foam specimens (according to the R^2 coefficient) was obtained for the method of cross-section analysis ($d_{p_{cs}}$, $R^2 = 0.9990$).

Another parameter that is often used as a characteristic for the prediction of κ_{perm} is hydraulic diameter (d_h) (B. Dietrich, W. Schabel, M. Kind, & H. Martin, 2009; O. Pitois, E. Lorenceau, N. Louvet, & F. Rouyer, 2009). By definition, d_h is an equivalent diameter of the opening area (A) with wetted perimeter (P), found as:

$$d_h = 4\frac{A}{P} \tag{2.16}$$

To evaluate d_h, a MATLAB script was written that allowed for the calculation of A and P in each cross-section, and the mean values of d_h for each image stack were obtained (see Table 2.12).

Table 2.12 Hydraulic diameters of foams ($d_h/d_{h,c}$)

Parameter	10 PPI		30 PPI		60 PPI	
	#1	#2	#1	#2	#1	#2
d_h, $[mm]$	8.85	9.08	4.64	4.28	4.27	4.97
$d_{h,c}$, $[mm]$	6.46	6.64	3.43	3.16	2.93	3.32
ε, $[\%]$	85.8	85.0	81.6	75.1	87.9	89.5
S_v, $[m^{-1}]$	531	512	951	950	1202	1078

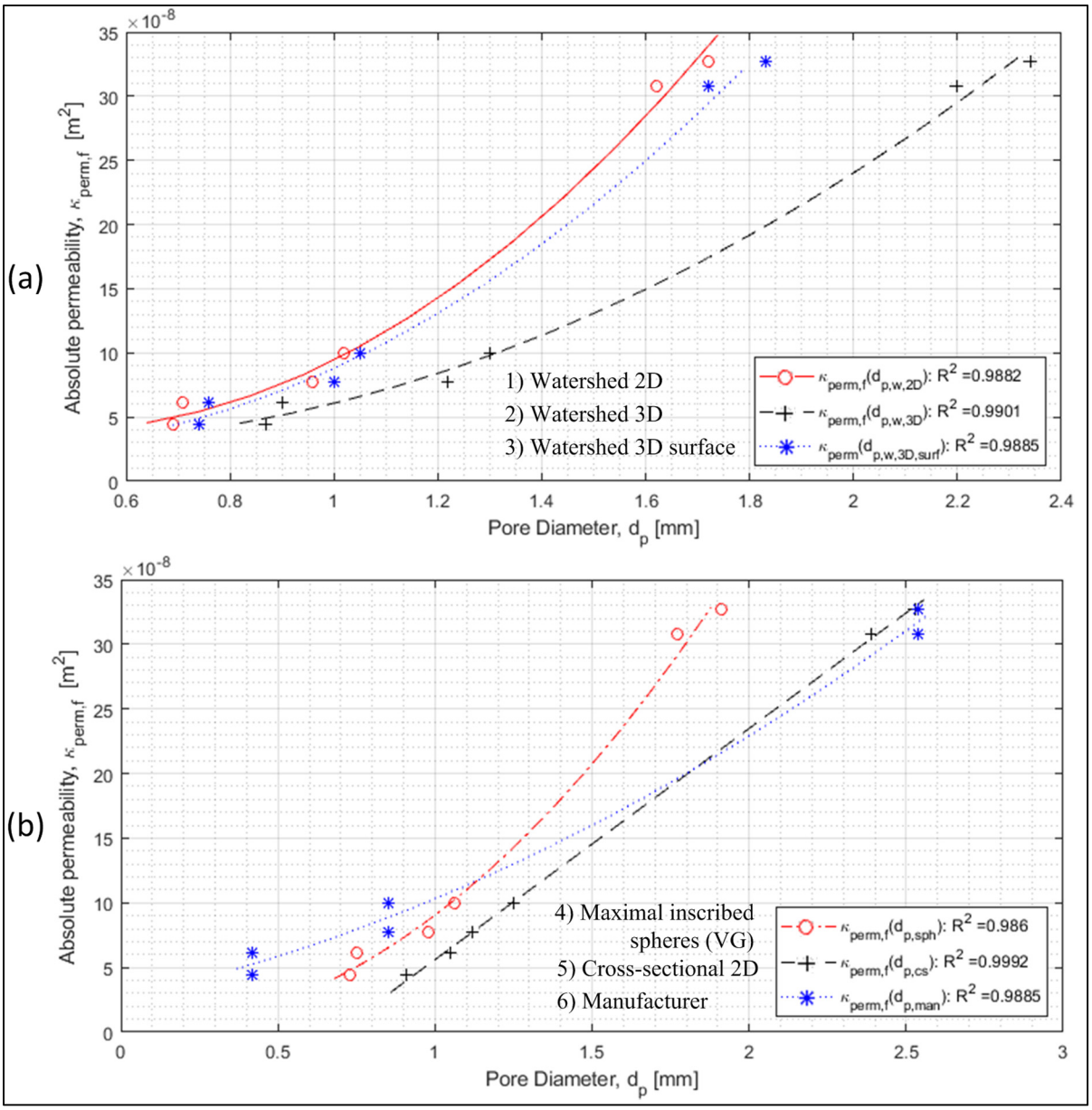

Figure 2.18 Dependence of absolute permeability ($\kappa_{perm,f}$) on pore diameters (d_p) determined using different techniques: (a) Watershed 2D ($d_{p_{w,2D}}$), watershed 3D ($d_{p_{w,3D}}$), watershed 3D (surface) ($d_{p_{w,3D,surf}}$); (b) Maximal inscribed spheres ($d_{p_{sph}}$), cross-sectional 2D ($d_{p_{cs}}$), manufacturer ($d_{p_{man}}$)

The alternative method for the evaluation of the hydraulic diameter is based on the assumption of the equivalent cylindrical diameter ($d_{h,c}$). According to A. Schlegel, P. Benz, and S. Buser (1993), this can be found as:

$$d_{h,c} = 4\frac{V_{void}}{S_{surf}} = 4\frac{\varepsilon}{S_v} \tag{2.17}$$

where $S_v = S_{surf}/V_{tot}$ is the specific surface.

By investigating pressure drops in porous foams with various PPI, (B. Dietrich et al., 2009) proposed the next correlation of the Forchheimer equation:

$$\frac{\Delta p}{L} = 110\frac{\mu}{\varepsilon \cdot d_{h,c}^2}V + 1.45\frac{\rho}{\varepsilon^2 \cdot d_{h,c}}V^2 \tag{2.18}$$

From which we can see that:

$$\kappa_{perm,D} = \frac{\varepsilon \cdot d_{h,c}^2}{110} \tag{2.19}$$

Figure 2.19 demonstrates the dependence of absolute permeability on hydraulic diameters. Results of d_h obtained from 2D image slices did not correlate well with $k_{perm,f}$ for 30 PPI and 60 PPI specimens. Due to this, it might be assumed that high PPI foams require image slices with higher resolution that allow for a more accurate determination of A and P [see Eqn. (2.16)]. Considering results for $d_{h,c}$, they provided a better fit for the prediction of k_{perm} and a good convergence between VG and the correlation proposed by B. Dietrich et al. (2009).

Finally, pore diameters found using the cross-sectional analysis method provided the best fit (based on the R^2 coefficient) to predict $\kappa_{perm,f}$. Thus, $d_{p_{cs}}$ was considered as the characteristic parameter of the foam specimens and was selected to design equivalent diamond lattices. Hence, correlation for $\kappa_{perm,f} = f(d_{p_{cs}})$ was found as:

$$\kappa_{perm,f} = 17.88 \cdot 10^{-5} \cdot d_{p_{cs}} - 12.28 \cdot 10^{-8}\ [m^2] \tag{2.20}$$

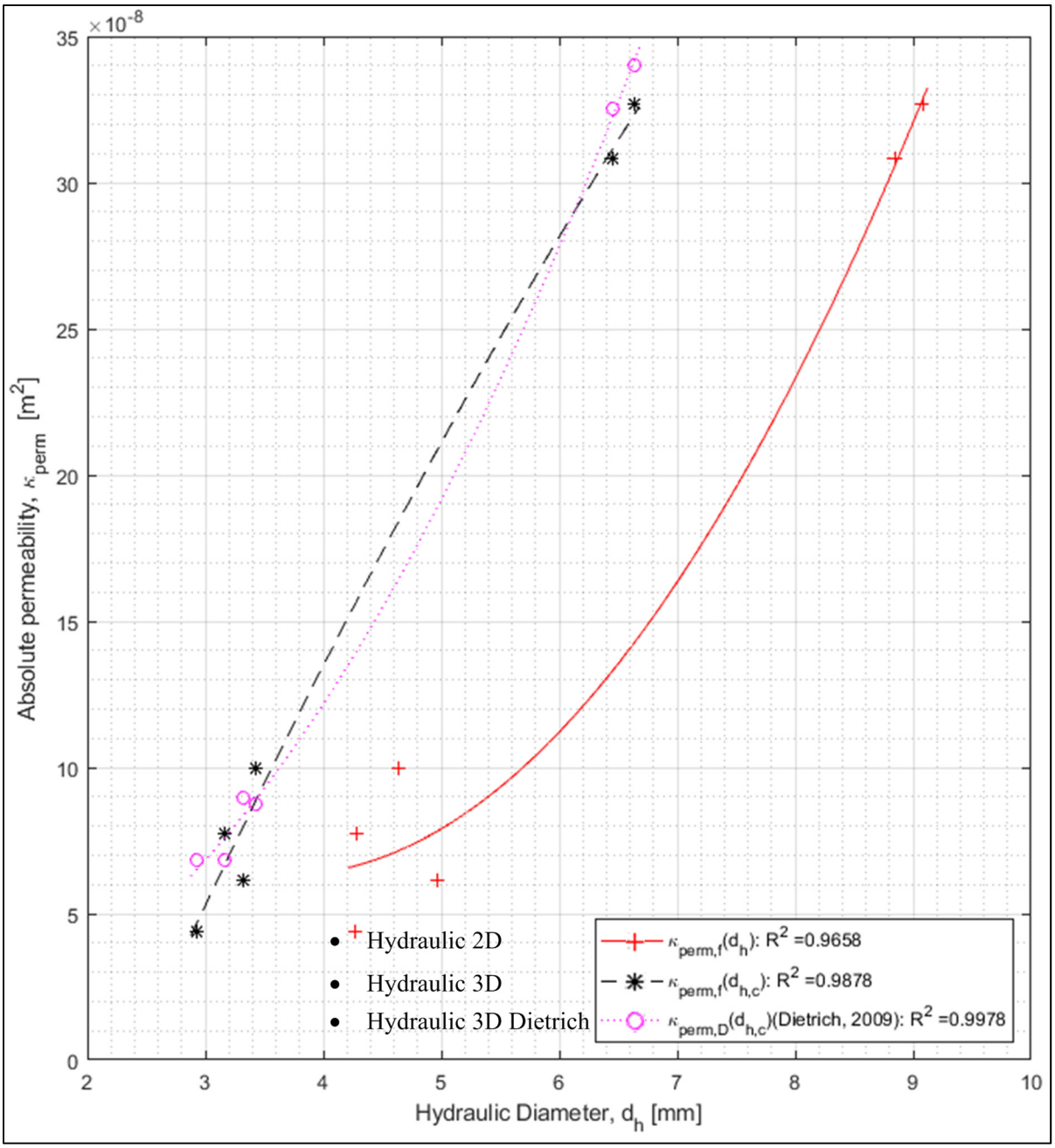

Figure 2.19 Dependence of absolute permeability (κ_{perm}) on hydraulic diameters (d_h)

Discrepancy among specimens of the same PPI was evaluated based on $d_{p_{cs}}$ parameter and represented 5.9 %, 11.6 %, and 15.4 % for 10 PPI, 30 PPI and 60 PPI foams, respectively. From these values it might be concluded that discrepancy among specimens having the same

porosity increases with increasing PPI. This result suggests that control over pore size becomes more difficult as pore size decrease. This observed discrepancy favourably supports our approach of using diamond lattice to obtain controlled and predictable foam geometry for PMB.

2.3 Diamond lattice design and analysis

Figure 2.20 illustrates three main phases of the diamond lattice structure generation using a MATLAB script written by M. Dumas et al. (2017). Two sets of input data are used (Figure 2.20a): 1. an STL-file of a body to be filled with lattices, which, in our case, corresponds to the disk-like ∅101.6*x*50.8 *mm* volumes, and 2. a series of data related to the diamond lattice structure: the strut thickness (t_s), the size of a single diamond unit cell (a), and the replication number of unitary cells in x-, y-, and z-directions (n_x, n_y, n_z). Next, voxelization of the volumetric domain takes place (Figure 2.20b), and, finally, the voxels are replaced by diamond cells to form a disk-shaped specimen filled with diamond lattices of a given geometry (Figure 2.20c).

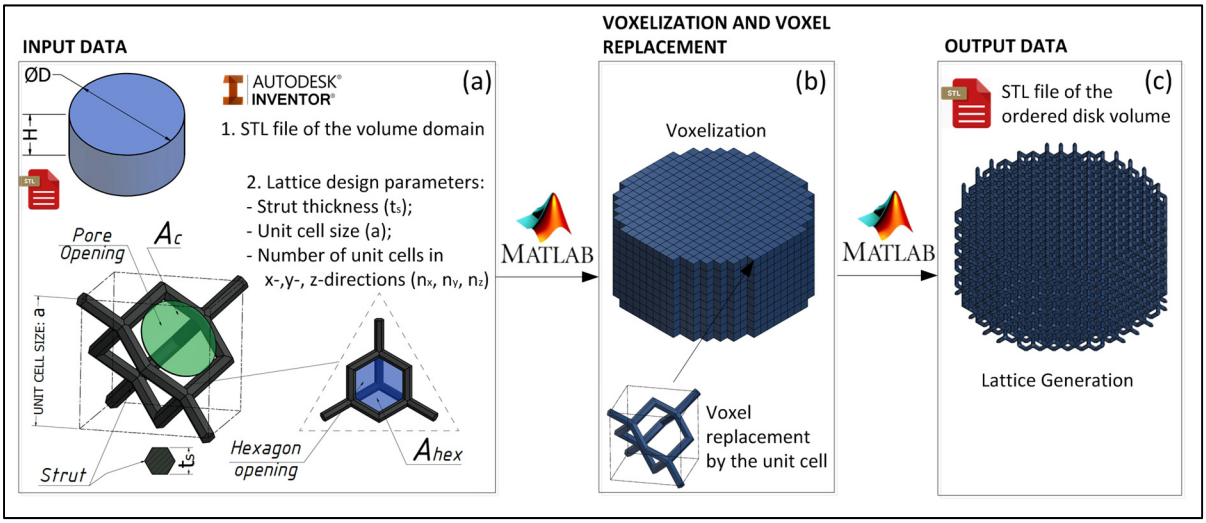

Figure 2.20 Voxelization and lattice generation :
(a) Input data: volume domain and unit cell definition; (b) voxelization and voxel replacement; (c) lattice generation
Adapted from B. Jetté et al. (2018)

Prior to analysis, the geometry of the diamond lattice was investigated and relationships of interest were found (see APPENDIX II, p. 99). This allowed us to find all the required geometric parameters (ε, n_x, n_y, n_z, etc.) by defining unit cell size (a) and strut thickness (t_s).

To find the equivalent to the foam lattice design, three criteria of equivalency were established: the first being absolute permeability ($\kappa_{perm,f}$), which characterizes flow behaviour, and the second and third being porosity ($\varepsilon_{tot,VG}$) and pore diameter ($d_{p,cs}$), respectively, which characterize overall lattice geometry.

By treating a unit cell size "a" as a scaling factor, we obtained solutions for a structure with $a = 1$ and the dimensionless parameter a/t_s. Further, the results could easily be expanded into a general form by applying the corresponding scaling factor "a^n".

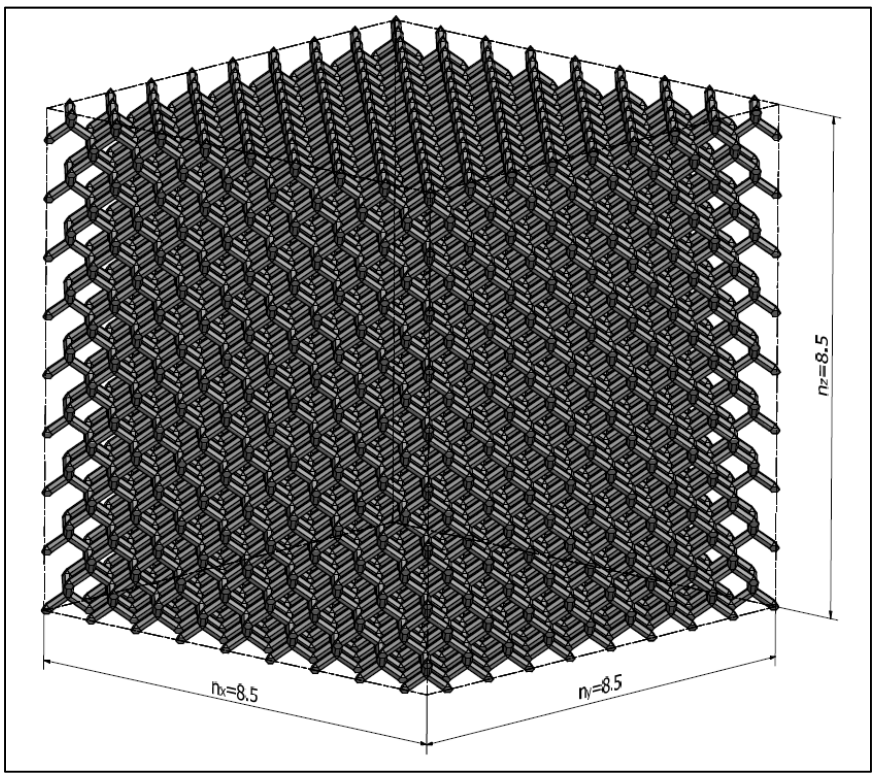

Figure 2.21 Characteristic diamond lattice volume for absolute permeability analysis

For our analysis, we used a diamond lattice with unit cell size $a = 1$ and $8.5x8.5x8.5$ unit cells (see Figure 2.21). Geometric parameters varied by varying strut thickness (t_s). After geometries with different a/t_s parameters were modelled, they were imported into VG and the corresponding absolute permeabilities $\kappa_{perm,lat} = f(a, t_s)$, porosities $\varepsilon_{lat} = f(a, t_s)$ and pore diameters $d_{p,lat} = f(a, t_s)$ were evaluated:

$$\kappa_{perm,lat} = \left(2.248(\frac{a}{t_s}) - 4.59\right) a^2 \cdot 10^{-3}\ [m^2] \tag{2.21}$$

$$\varepsilon_{lat} = 1.004 - 2.908\left(\frac{t_s}{a}\right)^{1.64} \tag{2.22}$$

$$d_{p,lat} = 0.744a - 1.217t_s \tag{2.23}$$

Figure 2.22 demonstrates the influence of "a/t_s" on dimensionless absolute permeability (κ_{perm}/a^2) and (ε). Higher a/t_s values are characteristic of geometries with more open porosities and, as a result, higher permeabilities.

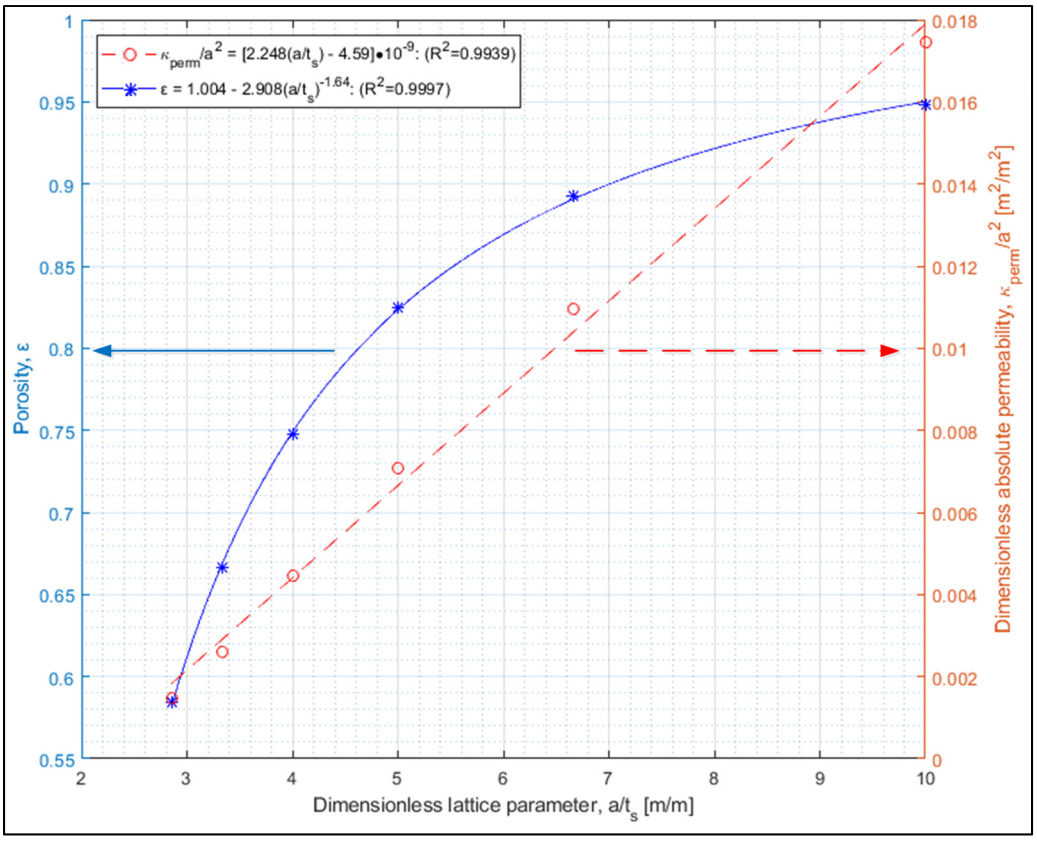

Figure 2.22 Dependence of dimensional absolute permeability (κ_{perm}/a^2) and porosity (ε) on the dimensionless diamond lattice parameter (a/t_s)

As was previously shown, the parameters of $\kappa_{perm,lat}$, ε_{lat}, and $d_{p,lat}$ were obtained as $f(a, t_s)$. From here, we were able to find three equivalent structures:

a) Equivalent permeability ($\kappa_{perm,f} = \kappa_{perm,lat}$) and porosity ($\varepsilon_{tot,VG} = \varepsilon_{lat}$);

b) Equivalent permeability ($\kappa_{perm,f} = \kappa_{perm,lat}$) and pore diameter ($d_{p,cs} = d_{p,lat}$);

c) Equivalent pore diameter ($d_{p,cs} = d_{p,lat}$) and porosity ($\varepsilon_{tot,VG} = \varepsilon_{lat}$).

The following equation systems were solved [Eqn. (2.24), Eqn. (2.25), and Eqn. (2.26)], which lead to the determination of appropriate a and t_s values for each case. Results are presented in Table 2.13:

$$\begin{cases} \kappa_{perm,f} = [2.248(a/t_s) - 4.59]a^2 \cdot 10^{-3} \\ \varepsilon_{tot,VG} = 1.004 - 2.908(a/t_s)^{-1.64} \end{cases} \quad (2.24)$$

$$\begin{cases} \kappa_{perm,f} = [2.248(a/t_s) - 4.59]a^2 \cdot 10^{-3} \\ d_{p,cs} = 0.744a - 1.217t_s \end{cases} \quad (2.25)$$

$$\begin{cases} \varepsilon_{tot,VG} = 1.004 - 2.908(a/t_s)^{-1.64} \\ d_{p,cs} = 0.744a - 1.217t_s \end{cases} \quad (2.26)$$

Figure 2.23 represents 10 PPI (#1) foam and corresponding diamond lattices with three different criteria of equivalency.

Table 2.13 Parameters of equivalent diamond lattices

Parameters	**10 PPI (#1)**	**60 PPI (#1)**
a) Equivalency: permeability ($\kappa_{perm,f}$) and porosity ($\varepsilon_{tot,VG}$)		
Target parameters		
$\kappa_{perm,f}$, $[10^8 \cdot m^2]$	30.83	4.39
$\varepsilon_{tot,VG}$, $[\%]$	85.8	87.9
Calculated parameters		
a, $[mm]$	5.78	2.04
t_s, $[mm]$	0.94	0.3
$d_{p,lat}$, $[mm]$	3.16	1.15
Δ_{d_p}, $[\%]$	32.06	26.67
b) Equivalency: permeability ($\kappa_{perm,f}$) and pore diameter ($d_{p,cs}$)		
Target parameters		
$\kappa_{perm,f}$, $[10^8 \cdot m^2]$	30.83	4.39
$d_{p,cs}$, $[mm]$	2.39	0.91
Calculated parameters		
ε_{lat}, $[\%]$	95.46	95.35
a, $[mm]$	3.72	1.42
t_s, $[mm]$	0.31	**0.12**
c) Equivalency: pore diameter ($d_{p,cs}$) and porosity ($\varepsilon_{tot,VG}$)		
Target parameters		
ε_{lat}, $[\%]$	85.8	87.9
$d_{p,cs}$, $[mm]$	2.39	0.91
Calculated parameters		
$\kappa_{perm,f}$, $[10^8 \cdot m^2]$	17.68	2.76
a, $[mm]$	4.38	1.61
t_s, $[mm]$	0.71	**0.24**

Analysis of the obtained data showed that equivalency in terms of $\kappa_{perm,f}$ and $d_{p,cs}$ provided structure with excess porosity and the smallest strut thicknesses, which are out of the equipment's manufacturing range ($t_s < t_{s,min} = 0.3\ mm$). Equivalency in terms of $d_{p,cs}$ and $\varepsilon_{tot,VG}$ also provided struts with $t_s < t_{s,min}$ for 60 PPI specimens, which were the subject of our research. Moreover, the obtained values of permeability for $d_{p,cs}$ and $\varepsilon_{tot,VG}$, when compared to the foam's geometry, had elevated discrepancies in the range of $55\% < \Delta_{\kappa_{perm}} < 155\%$. We chose equivalency in terms of $\kappa_{perm,f}$ and $\varepsilon_{tot,VG}$, which provided the appropriate strut thicknesses of $t_s \geq 0.3$ for all cases. Values of pore diameters had discrepancies in the range of $25\% < \Delta_{d_p} < 60\%$ (when compared to the foam's geometry).

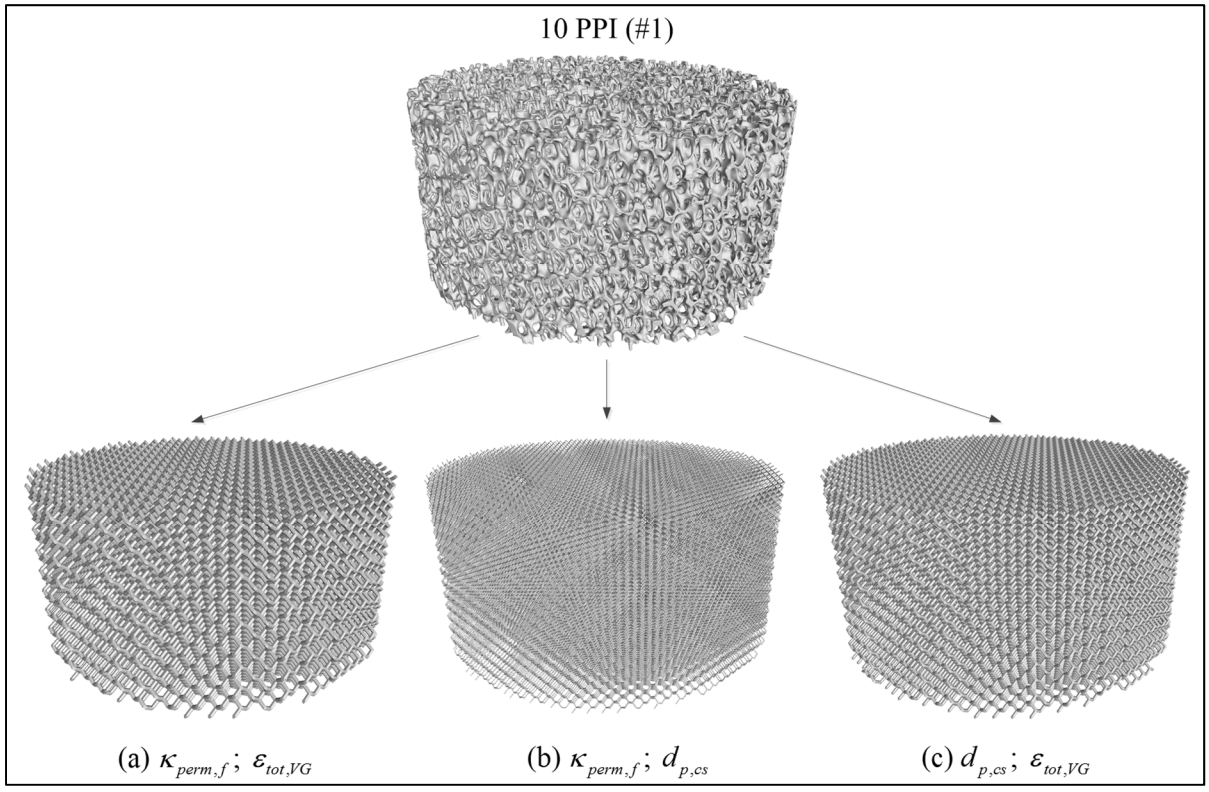

Figure 2.23 10 PPI (#1) foam. Diamond lattices with various criteria of equivalency: (a) Permeability and porosity; (b) Permeability and pore diameter; (c) Pore diameter and porosity

Finally, diamond lattices, which are equivalent to foams, were chosen. Table 2.14 summarizes the parameters of foams and lattices selected for additive manufacturing.

Table 2.14 Final design parameters of diamond lattices
and parameters of their foam equivalents

Parameter	10 PPI		60 PPI	
	Foam #1	Diamond lattice	Foam #1	Diamond lattice
Lattice n_x x n_y x n_z	-	17.5x17.5x8.5	-	49.5x49.5x24.5
Absolute permeability, κ_{perm} $[10^8 \cdot m^2]$	30.83	30.91*	4.39	4.32*
Porosity, ε $[\%]$	85.8	85.5*	87.9	87.3*
Unit cell size, a $[mm]$	-	5.81	-	2.05
Strut thickness, t_s $[mm]$	1.02	0.95	0.37	0.31
Pore diameter, d_p $[mm]$	2.39	3.17	0.91	1.15
Specific surface, S_v $[m^{-1}]$	531	508	1202	1366

* Slight difference due to structural adjustment of the overall dimensions

A flowchart of the design process of equivalent diamond lattices compared to the ceramic foams, is presented in Figure 2.24.

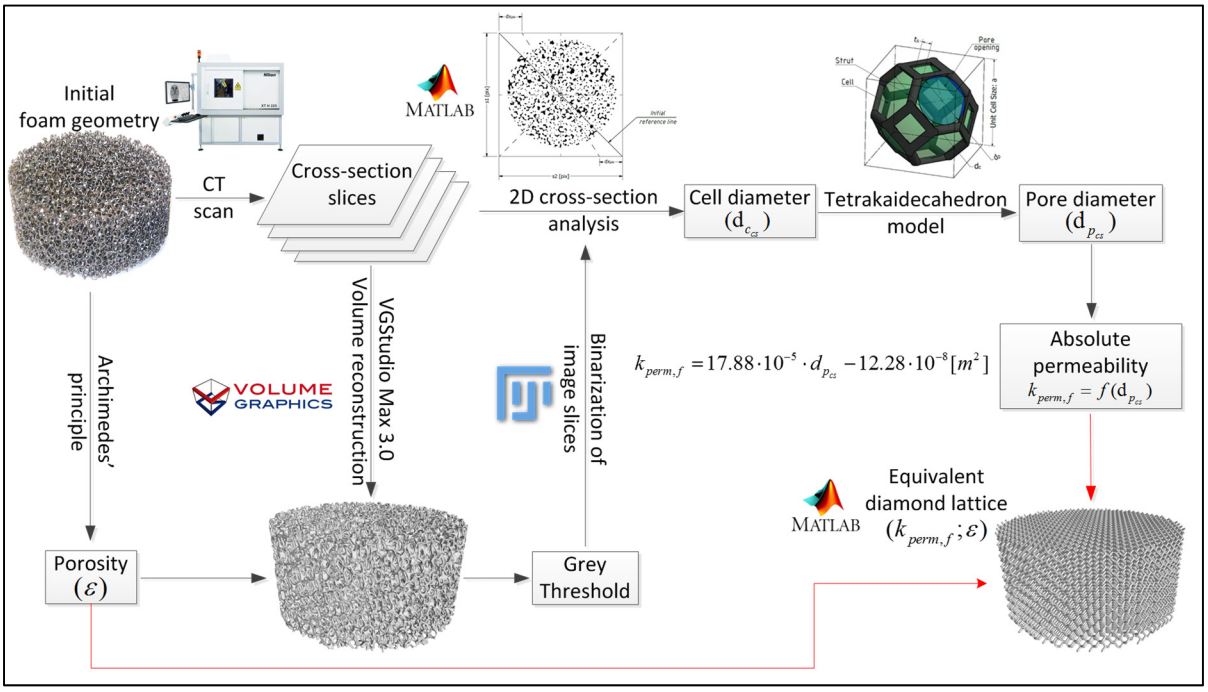

Figure 2.24 Process of the equivalent diamond lattice design

Figure 2.25 demonstrates that dimensionless absolute permeability (κ_{perm}/a^2) is dependent on dimensionless specific surface ($S_v \cdot a$). A higher $S_v \cdot a$ corresponds to a structure with a higher outer surface, and might be considered to be a frictional parameter that prevents the passage of the flow.

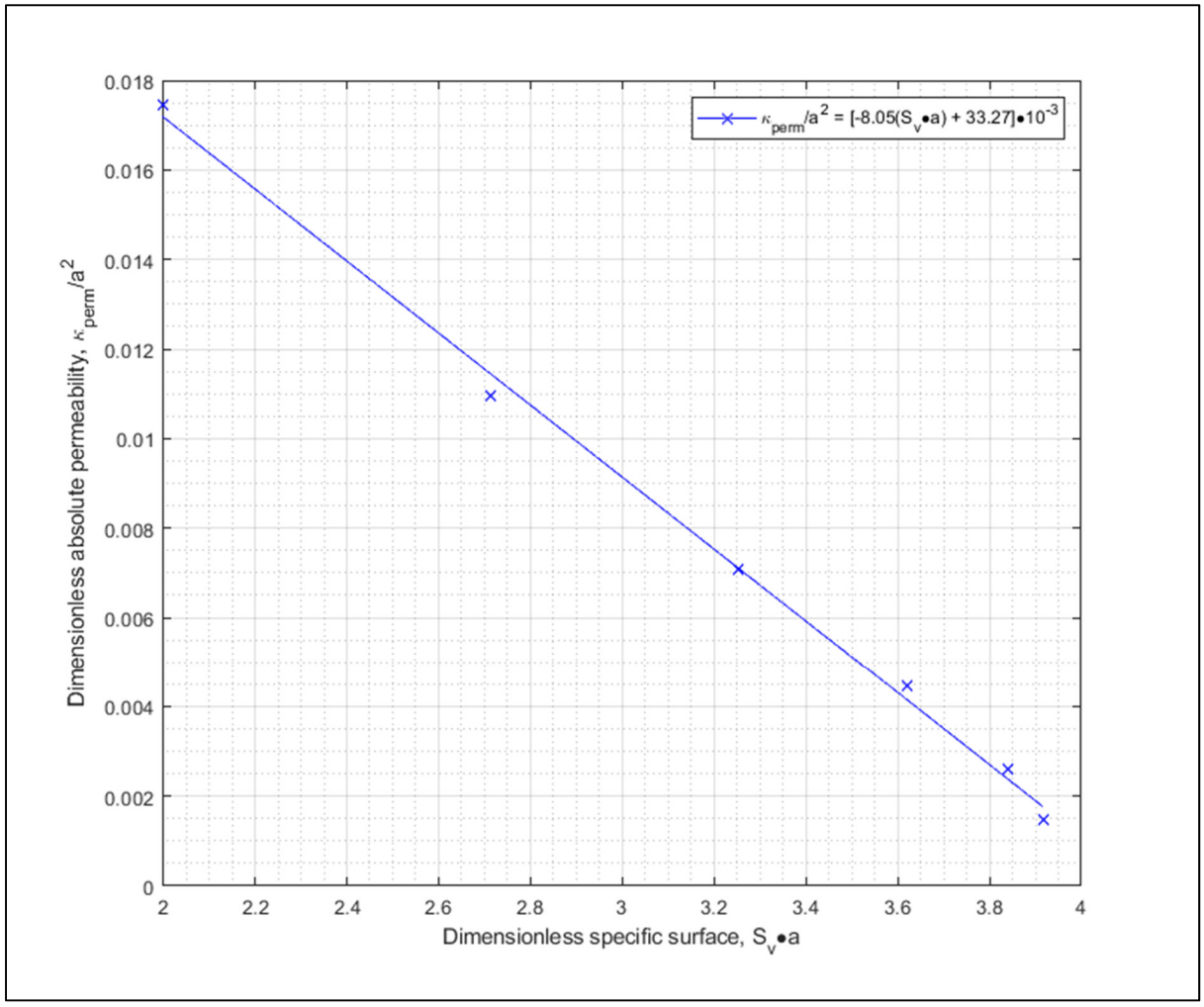

Figure 2.25 Dependence of dimensionless absolute permeability (κ_{perm}/a^2) on dimensionless specific surface ($S_v \cdot a$)

2.4 Additive manufacturing

After the geometric parameters of equivalent diamond lattices were determined, the next step was to prepare four specimens for additive manufacturing (see Table 2.14). A flowchart

representing the steps taken from the preparation of digital prototypes to the point where the specimens were ready for experimentation is presented in Figure 2.26.

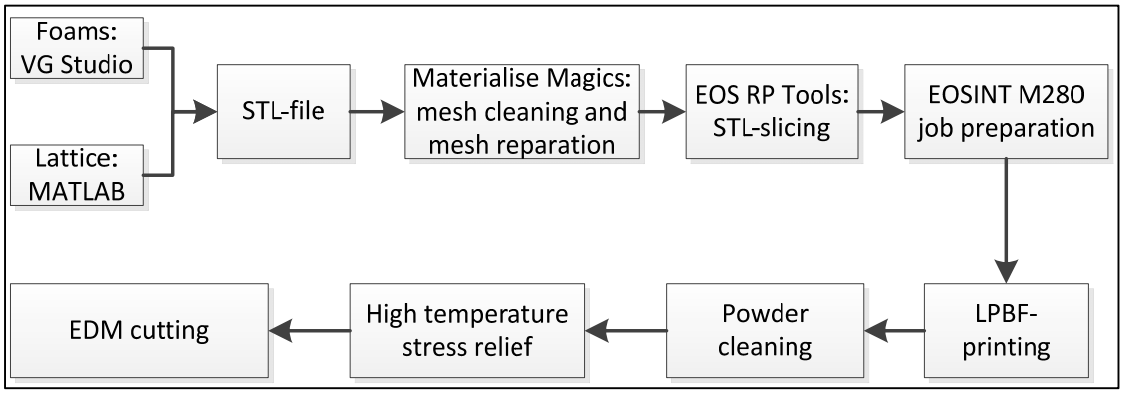

Figure 2.26 Additive manufacturing flowchart

First, STL-files of the four specimens were generated by means of VG for foams and a MATLAB script for diamond lattices. In the current work, the MATLAB script was improved by introducing parallel computing and generation of binary STL-files. This reduced the time and file size required to generate structures with a high number of elements (i.e. for 60 PPI lattice, generation time was x5.5 faster, and file size x4 smaller; tested on Intel® Xeon® CPU E5-2660x2, 28 cores). Each STL-file was then imported into the Materialise Magics software for mesh cleaning and for error reparation (flipped normals, overlapping triangles, etc.). Afterwards, each repaired STL-file was treated by the proprietary EOS RP Tools slicer, and the obtained files were used for final job preparation.

Next, the EOSINT M280 machine was filled with CoCr powder and the LPBF-printing process began. We unfortunately encountered some difficulties during the manufacturing of the *49.5x49.5x24.5* diamond lattice due to the jamming of the 3D printer's recoater with numerous thin struts (0.31 mm). This part was excluded from production. The application of a carbon brush recoater could overcome this problem in the future.

As a result, 3 specimens for CoCr were printed: 10 PPI Foam (#1), 60 PPI Foam (#1) and 10 PPI Diamond Lattice (17.5x17.5x8.5). Specimens were then cleaned of residual powder and

underwent subsequent stress relief of the parts by heat treatment (6 hours at 1150 °C under inert an argon atmosphere). Parts on the building plate post-heat treatment can be seen in Figure 2.27.

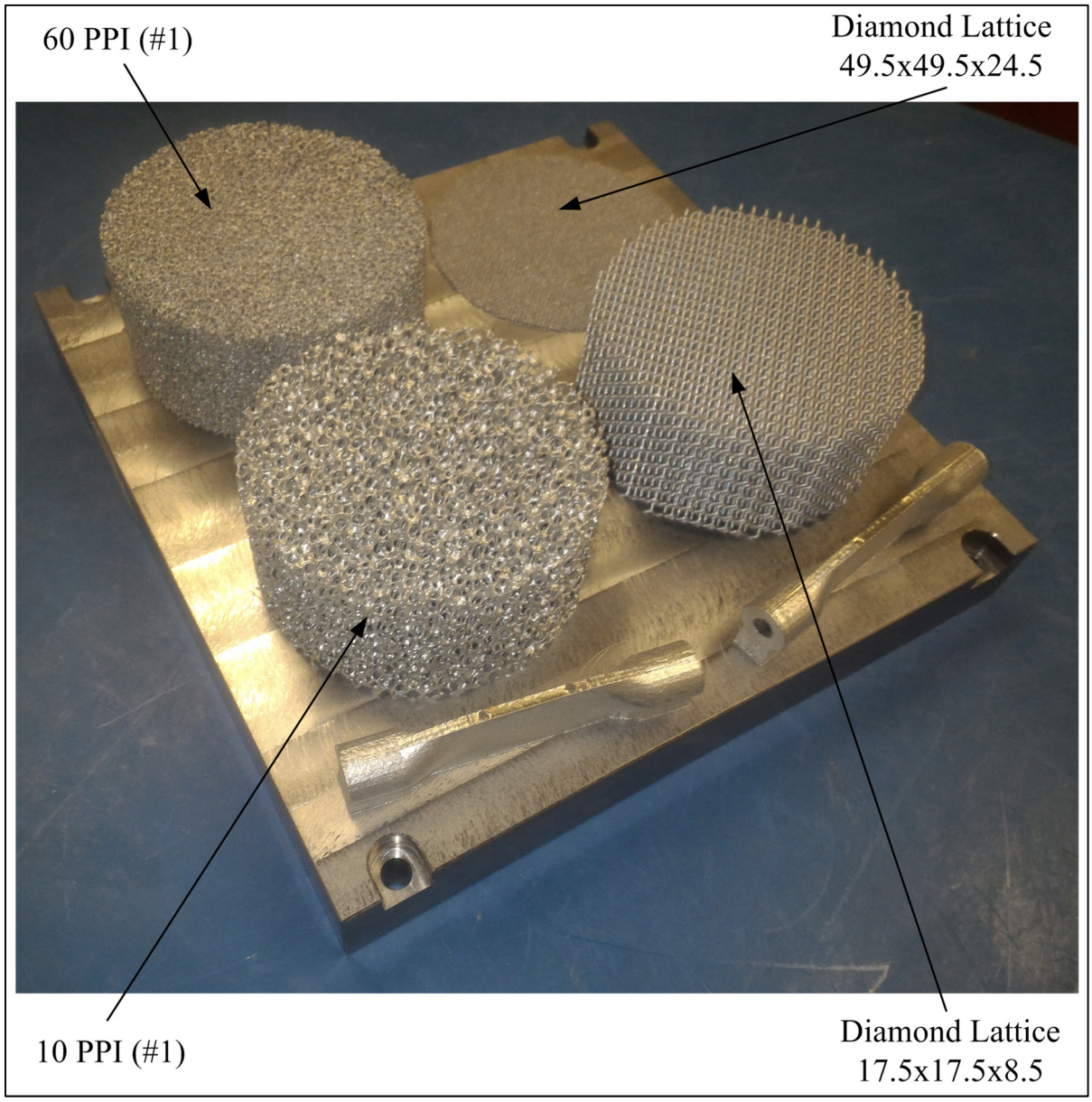

Figure 2.27 CoCr specimens after printing, cleaning and heat treatment

The parts were then cut from the building plate via electrical discharge machining (EDM) and each specimen was weighed (results are presented in Figure 2.28).

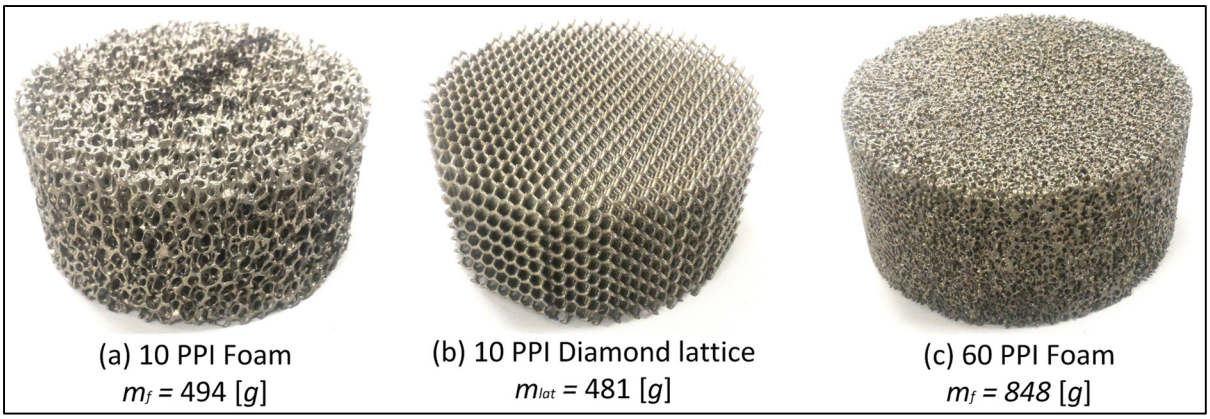

Figure 2.28 CoCr specimens after EDM cut

From the obtained values, we found that 10 PPI CoCr Foam and 10 PPI CoCr diamond lattices had similar relative masses ($m_f = 494\ g$ and $m_{lat} = 481\ g$, respectively), and thus porosities ($\varepsilon = 85.5\%$ and $\varepsilon = 85.9\%$, respectively). The discrepancies in porosity between obtained values and the design parameters ($\varepsilon = 85.8\%$ and $\varepsilon = 85.5\%$, respectively, see Table 2.14) can be attributed to possible error during the manufacturing process (STL file preparation, 3D printing, EDM cut, etc.). Moreover, the 60 PPI CoCr foam was overly dense and had a porosity of approximately $\varepsilon = 75.2\%$ compared to its theoretical value of $\varepsilon_{theor} = 87.9\%$. This was due to the sintering of additional CoCr powder caused by close positioning of strut elements. Similar results were obtained by R. Vrana, D. Koutny, and D. Paloušek (2016). The obtained results require the application of specific printing parameters that take into account the close arrangement of strut elements.

2.5 Test bench design

The conceptual design of the porous medium burner (PMB) was chosen as proposed by W. M. Mathis and J. L. Ellzey (2003). The burner's overall dimensions are shown in Figure-A IV-I (see APPENDIX IV, p. 105). A schematic of the experimental apparatus is shown in Figure 2.29. Air is fed from the compressed air source (1) and methane from the bottle (2). Methane is controlled by two mass flow controllers (MFC) Omega FMA 5400/5500 (3) with flow range of 0-15 lpm (calibrated for N2). Air is controlled by one MFC Azbil MQV0200

(4) with flow range of 0-200 lpm, and one Cole-Parmer impact-resistant flowmeter (IRF) RK-32900-54 (5) with flow range of 10-100 lpm (both calibrated for air). The flashback arrestor SGD 8491-F (6) was installed prior to the mixing chamber (7). Two porous mediums were installed in the upstream (8) and downstream (9) sections with respectively high and low pore densities.

Porous materials were wrapped in the "Industries 3R ceramic wool 3R2900" insulation blanket (10) and inserted into the stainless steel case. On the one side of the case, holes were drilled to insert twelve Omega K-type thermocouples (d=0.032'') (11) which, in turn, were inserted into ceramic sleeves and pierced through the insulation blanket. Above the burner, a probe was placed (12) so that the sampling path first leads to the cooling system with the water trap (13) and then to the gas analyzers (14) measuring CO, NO_x, CH_4, O_2, and CO_2 emissions. Accuracy and operation ranges of the equipment used are presented in Table-A V-1 (APPENDIX V, p. 107), and concentrations of calibration gases for gas analyzers are presented in Table-A V-2 (APPENDIX V, p. 107).

Prior to the upstream section of the burner, we installed a water manometer (15) for pressure drop measurements. The operational program was written in LabVIEW to control and read MFC's flow rates for various equivalence ratios to read the corresponding data from the thermocouples and gas analyzers. The test bench wiring diagram is shown in Figure-A VI-I (APPENDIX VI, p. 111). During each experiment, the corresponding data was written into a log file in 1-second intervals.

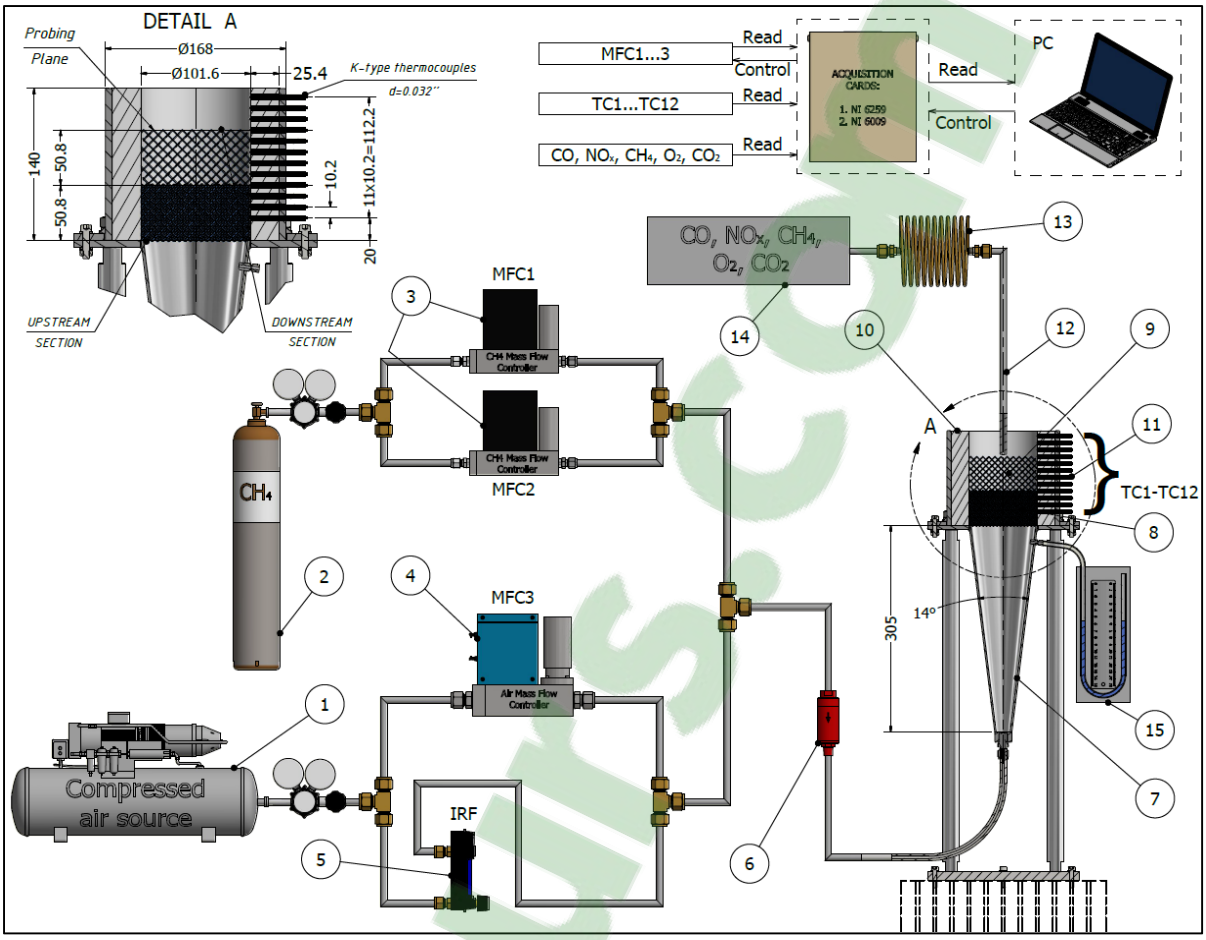

Figure 2.29 Schematic of experimental apparatus

1 – Compressed air source; 2 – CH_4 methane bottle; 3 – Omega FMA 5400/5500 mass flow controller (0-15 lpm, N_2); 4 – Azbil MFC MQV0200 (0-200 lpm, Air); 5 – Cole-Parmer IRF RK-32900-54 (10-100 lpm, Air); 6 – Flashback arrestor SGD 8491-F; 7 – Mixing chamber; 8 – Foam (high pore density); 9 – Foam/Diamond lattice (low pore density); 10 – Insulation blanket "Industries 3R ceramic wool 3R2900"; 11 – Omega K-type thermocouples (d=0.032''); 12 – Probe; 13 – Gas cooling system with water trap; 14 – Gas analyzers: CO (CAI Model 200), NO_x (CAI 600 Series), CH_4 (CAI 600 Series), CO_2 and O_2 (ABB Multifid URAS 14) ; 15 – Water Manometer.

2.6 Testing procedures

Temperature profiles and pollutant emissions of the CH_4/air mixture for all six setups (see Figure 2.5) were examined at the same flow regime. Parameters of the flow ($\phi = 0.6$; $V = 34.6$ *cm/s*) were chosen based on our review of the literature and the range of stable operation limits (M. T. Smucker & J. L. Ellzey, 2004). Flame speed (V) was taken according to V. Khanna et al. (1994) and assumed as a ratio of total flow rate ($\dot{Q}$) to the cross-section area (A) of the porous material:

$$V = \frac{\dot{Q}}{A} \tag{2.27}$$

Each experiment was preceded by preparative measures, such as a leak test, an equipment warm-up phase (2.5 hours), and the calibration of gas analyzers. O_2 and CO_2 emissions were measured for various ϕ to check for correct composition of the CH_4/air mixture controlled by LabVIEW. The measured values of the products agreed with theoretical values. After undergoing these preparative procedures, each experiment began with the preheating of the burner at $\phi = 0.75 - 0.8$ for 10-20 minutes. The flame front at these conditions was located near the edge of the downstream section. 50 *lpm* of air was provided at a constant rate during each test. After the preheating phase, equivalence ratio and total flow rate steadily decreased, until the flow was stabilized at $\phi = 0.6$ and $V = 34.6$ *cm/s*. The location of the flame front was observed just downstream from the interface of the two sections.

After reaching a steady-state regime, a probe took samples at 9 critical points just above the downstream section (centre and around the perimeter, see Figure 2.30). Each point was probed for a period of 1 minute to measure pollutant deviations. During our first attempt of measurements, we detected an increase in CH_4 emission level at several points around the perimeter. Upon examination, we found that this was due to the to measure these deviations tight insulation wrapping around the porous material. We corrected for this by adding

additional layers of insulation. Once we had verified that the burner was operating properly, temperature, pollutant emissions, and pressure drop measurements were taken.

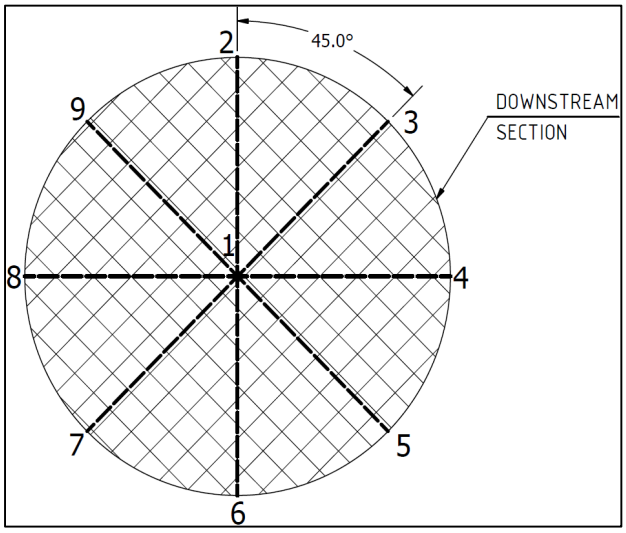

Figure 2.30 Emission probing points

2.7 Summary of the design methodology

In this chapter, we describe the steps leading to the final PMB test bench design. Three types of ceramic SiSiC foams with different pore sizes (10 PPI, 30 PPI, and 60 PPI) were chosen. This resulted in the selection of six experimental setups that allowed for comparison between irregular foam and patterned diamond lattice geometries, as well as between ceramic SiSiC and metal CoCr materials. Based on the X-ray CT scan data, different methods of foam morphology analysis were used to determine porosity, strut thickness, cell/pore size, and absolute permeability. By comparing the pore size results obtained from the different approaches with the results of direct measurements from 3D reconstructed volumes, the closest fit was attributed to $d_{p,cs}$ (which is found through a combination of the adapted cross-section analysis method (d_{cs}) and the tetrakaidecahedron model). Moreover, values of $d_{p,cs}$ provided the best fit for prediction of absolute permeability obtained from simulations in VGStudio Max software.

Based on the results of foam analysis, equivalent diamond lattices were designed in terms of their porosity and absolute permeability. As a result, three specimens (10 PPI foam, 10 PPI diamond lattice, and 60 PPI foam) were printed from CoCr material by means of the LPBF method. 10 PPI foam and lattice specimens had the anticipated porosities and geometries, whereas the porosity of the 60 PPI foam was lower than what was predicted, due to sintering of additional material during manufacturing and the resulting smaller pores. Adapting the AM for the production of diamond lattices with high PPI could solve this discrepancy.

Finally, the test bench was assembled and the required equipment was connected by tubing and wiring. The control program was written in LabVIEW, which allowed us to read and control the parameters of the flowmeters, thermocouples, and gas analyzers.

CHAPTER 3

EXPERIMENTAL RESULTS

This section presents our experimental results. The primary goal was to compare reference setup #1 (SiSiC foams in the upstream and downstream sections) and setups with 3D-printed CoCr porous specimens in terms of their temperature profiles, pollutant emissions, and stable operation. Additionally, we investigated the structural durability of porous materials.

3.1 Experimental results

3.1.1 Temperature

Temperature measurements were taken by inserting 12 thermocouples into ceramic sleeves and piercing them through an insulation blanket (see Figure-A IV-I, APPENDIX IV, p. 105). All temperature measurements—due to thermal equilibrium between the thermocouple hot junction, the gas, and the solid phase—should be understood as a mean value between the gas and solid phases (R. W. Francisco Jr., F. Rua, M. Costa, R. C Catapan, & A. A. M. Oliveira, 2009; R. Huang, L. Cheng, K. Qiu, C. Zheng, & Z. Luo, 2016). Results of the temperature profiles represent the same moment corresponding to 10-minute intervals after the flame had been stabilized near the interface of the upstream and downstream sections. Figure 3.1 provides information on average temperatures (T_{av}; Figure 3.1a) and temperature profiles for all six setups. The setups are divided in two categories for the upstream section namely SiSiC foam in Figure 3.1b and CoCr foam in Figure 3.1c.

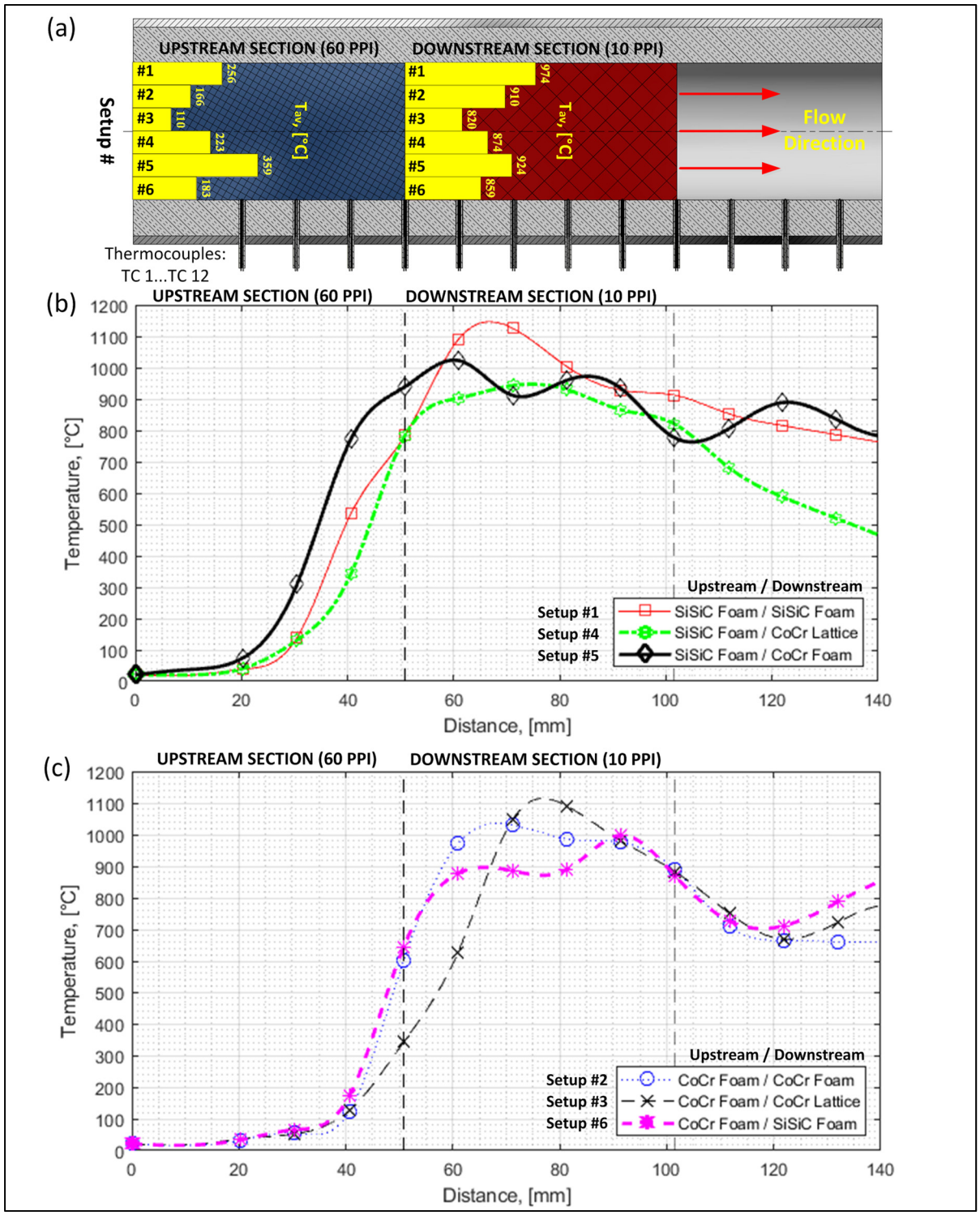

Figure 3.1 Temperature profiles:
(a) T_{av} in the upstream and downstream section;
(b) First case: 60 PPI SiSiC and three PM;
(c) Second case: 60 PPI CoCr and three PM

The first case (Figure 3.1b; setups #1, #4, and #5) represents 60 PPI SiSiC foam in the upstream section and three porous media (10 PPI SiSiC foam (#1), 10 PPI CoCr lattice (#1), and 10 PPI CoCr foam) in the downstream section. It is difficult to make a certain conclusion based on temperature profiles in the first case, as after approximately 10 minutes of stable operation, the flame front tended to shift towards the upstream section without quenching and produced flashback. This phenomenon corresponds to filtration combustion, which was also observed by P.-F. Hsu et al. (1993). One might conclude that the operational regime ($\phi = 0.6$; $V = 34.6$ *cm/s*) that was chosen from the literature was unstable for the setup with ceramic 60 PPI SiSiC foam in the upstream section, and may require a higher flame speed (V) at the chosen equivalence ratio of $\phi = 0.6$. However, the general trend that was observed, is that reference setup #1 (all-ceramic) provided the highest T_{max} in comparison with setups #4, and #5 which had CoCr specimens in the downstream section. Such result might be explained by higher k_s of SiSiC compared to CoCr.

The second case (Figure 3.1c; setups #2, #3, and #6) represents 60 PPI CoCr foam in the upstream section with the same three porous materials in the downstream section at the same flow conditions ($\phi = 0.6$; $V = 34.6$ *cm/s*) that were seen in the first case. From the experiment, by replacing SiSiC with CoCr in the upstream, we observed a general trend where the flame front shifted towards the centre of the downstream region. Moreover, it was observed that after stabilization, the flame front stayed at the same position without temperature fluctuation for an extended period of time (>20 minutes). Table 3.1 summarizes information on the T_{av}, T_{max} and flame front position (x_f) with standard deviations calculated on a 10-minute interval of stable operation. Variation in temperature measurements and flame location did not exceed 3% and for that reason were considered as stable operation regime.

Table 3.1 Average temperature (T_{av}), maximum temperature (T_{max}) and flame front location

Setup #	Average temperature, T_m [°C]		Maximum temperature, T_{max} [°C]	Flame front location, x_f [mm]
	Upstream Section	Downstream Section		
2: CoCr foam	166±12	910±20	1037±23	68.5±1
3: CoCr lattice	110±14	820±16	1108±17	77±1
6: SiSiC foam	183±13	859±11	998±12	91.5±1

In comparing the temperature profiles of setup #2 and setup #6, similar temperature profiles were obtained in the upstream section and during transition to the downstream section. However, near the flame front's location, the SiSiC material (setup #6) provided lower temperatures when compared to the CoCr material (setup #2). Since the thermal conductivity (k_s) of both materials differs by less than 28% (see Table 2.1), we expected no significant change in maximum temperature according to numerical analysis provided by A. J. Barra et al. (2003), who changed k_s by 1000%, and according to the experimental results obtained by H. B. Gao et al. (2014), who varied k_s by 155%. Therefore, the results of Figure 3.1c are consistent with the literature and with the results from Table 3.1, which shows that the average downstream temperature differs by only 6% between SiSiC and CoCr foams. Replacing foams (setup #2) with lattices (setup #3) resulted in the downstream shift of the flame front and in higher T_{max}, which may be attributed to higher d_p in the lattice structure.

By comparing two cases, higher k_s of SiSiC in the upstream section (setups #1, #4, and #5) may be responsible for unstable operation and flame displacement towards the inlet section, which corresponds with the numerical analysis provided by A. J. Barra et al. (2003), such that higher k_s in the upstream results in a higher V_{min} and lower dynamic range. This observation is supported by Table 2.1, which shows the difference in k_s between SiSiC and CoCr materials for high and low temperatures. It might be concluded that differences in heat transport properties are more influential at lower temperatures (corresponding to the upstream section), whereas for higher temperatures (corresponding to the downstream section), thermal properties are of the same order, and should be less influential on flame properties.

3.1.2 Flame stability

During operation, various flame instabilities were observed prior to finding operational regimes. For SiSiC in the upstream region, we detected undesirably high energy recirculation to the upstream section, which resulted in steady flame propagation towards the inlet section. This phenomenon was not observed with CoCr in the upstream region. The obtained result confirmed what was numerically predicted by A. J. Barra et al. (2003) in terms of an advantageous application of the material with low thermal conductivity (k_s) and high radiative extinction coefficients (κ_{rad}) in the upstream section. As a result of the lower k and slightly higher κ_{rad}, which according to P.-F. Hsu and J. R. Howell (1992) is higher for lower pore diameters, printed 60 PPI CoCr foam had superior flame arresting and stabilization properties.

3.1.3 Pollutant emissions

In all cases, emission profiles were close to the detection limit of the equipment. CO, $NO_{x,}$, and HC emissions are presented in Figure 3.2.

CO emissions were at the detection limit of the equipment, and did not exceed 325 ppm. We would suggest using more precise equipment to improve measurement precision. This might explain why, depending on the setup configuration, obtained values were higher than or similar to what was reported in previous research with different foams (H. B. Gao et al., 2014; C. Keramiotis et al., 2012). Lower values of CO were obtained for setups with 60 PPI CoCr foam in the upstream region, which corresponded to lower average temperature of the downstream region (see Table 3.1). Lower temperatures in the downstream region can also be linked to lower CO, as seen in H. B. Gao et al. (2014).

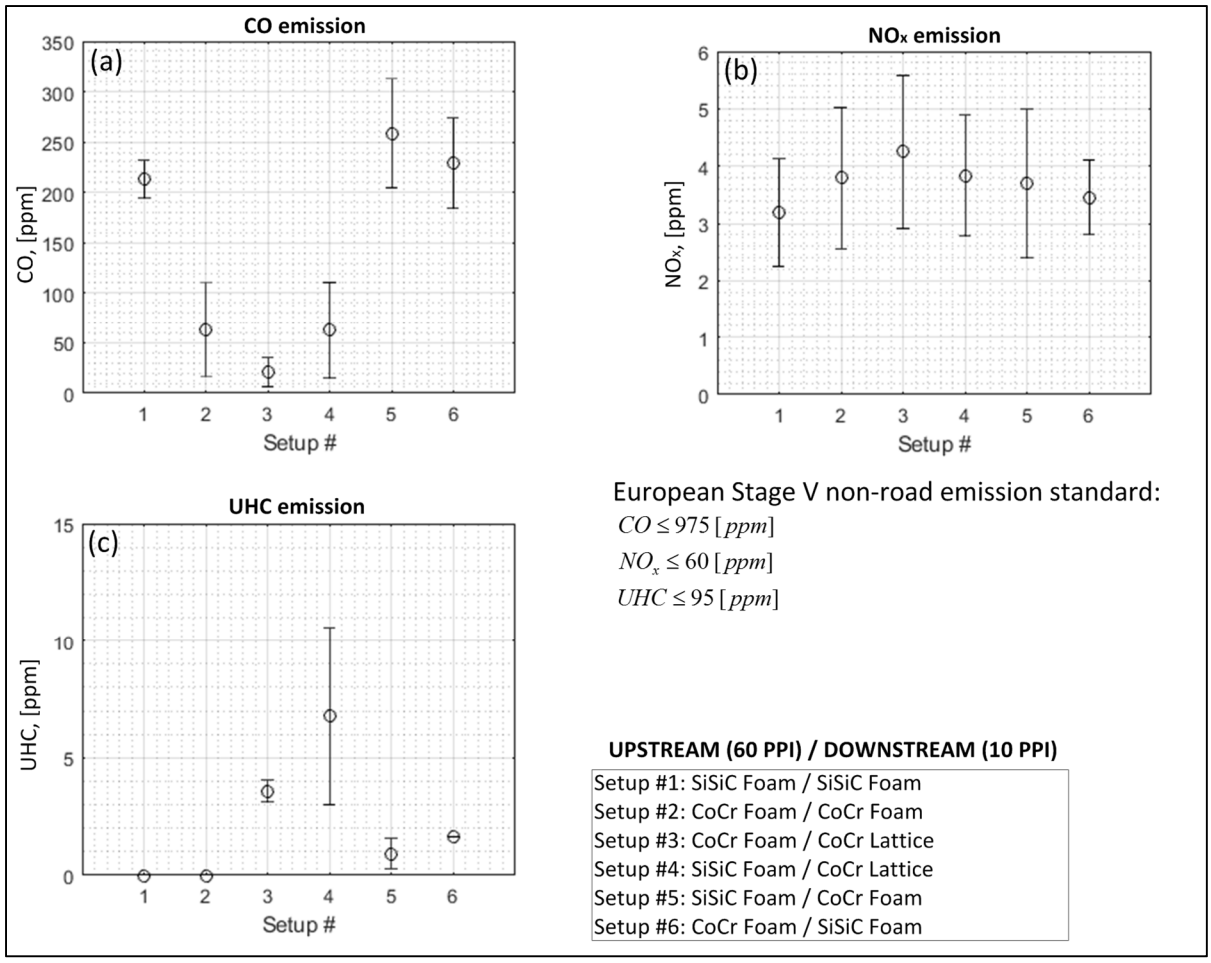

Figure 3.2 Results of pollutant emissions: (a) *CO*; (b) NO_x; (c) *UHC*

Our results for NO_x emissions were low and did not exceed 6 ppm, which is also near the detection limit of the equipment. These results correlated well with previous works (N. Djordjevic et al., 2012b; V. Khanna et al., 1994), and were attributed to operation at lean conditions ($\phi = 0.6$) with low flame temperatures ($T < 1600$ ℃), which ensured low thermal NO_x (the main source of emission at such a regime) (F. Avdic, 2004).

Similarly, HC emission was low and generally below 10 ppm. It was mainly attributed to complete combustion at lean limits.

Table 3.2 provides comparison of pollutant emissions between the current work and a "European stage V non-road emission standard" (Z. Shao & T. Dallmann, 2016)

[conversions from [g/kWh] to [ppm] in the standard were made according to TJ Pilusa, MM Mollagee, and Edison Muzenda (2012)]. The current PMB design demonstrated an approximately pollution-free operation which agrees well with our hypothesis.

Table 3.2 Comparison of pollutant emissions between the current work and "European stage V non-road emission standard"

Pollutant emissions	**Current work (Maximum)**	**European stage V non-road emission standard**
CO, [ppm]	310	975
NO_x, [ppm]	6	60
HC, [ppm]	11	95

3.1.4 Pressure drop

We also took pressure drop measurements of cold air for various flow velocities ($V = 0 - 72\ cm/s$). We used a water manometer as a measuring device, shown in Figure 2.29 (pos. 14). For each case, it was verified that at the beginning and at the end of the experiment, flow speed would be equal to zero ($V = 0\ cm/s$) and water level would remain the same.

Because single 10 PPI and 30 PPI specimens have very low pressure drop values, configurations involving two porous media (as was the case during the combustion experiment) were used. As some foams were damaged, 60 PPI CoCr foam was used in combination with other porous specimens for the pressure drop experiments.

Figure 3.3 demonstrates the dependence of pressure drop (Δp) on flow velocity (V). From the results we obtained in setup #4 and setup #5, we noticed similarities in the geometry of the acquired 10 PPI SiSiC foam and the printed replica 10 PPI CoCr foam, which demonstrates the replica's quality. From these setups, we could also see a similarity between foam and diamond lattice geometries in terms of absolute permeability (κ_{perm}).

Through comprehensive foam and diamond lattice analysis, mean pore diameters were evaluated, which allowed us to study the dependence of Reynolds number (Re) on pressure drop (Δp) (see Figure 3.4). Re was found as:

$$Re = \frac{V \cdot d_p}{\mu_{air}} \tag{3.1}$$

where V is flow velocity, d_p is pore diameter, and μ_{air} is air viscosity.

Table 3.3 shows the pore sizes used during evaluation of Re. Pore diameter of 60 PPI CoCr foam was adjusted to $\varepsilon = 75.2$ % according to Eq. (A I-10) and Eq. (A I-11), assuming unit cell size a to be constant. Pore diameters of setup #4, setup #5, and setup #6 were taken as mean diameters between the two foams in the setup.

Table 3.3 Pore diameters of specimens

Specimen	d_p, $[mm]$
60 PPI CoCr foam	0.75
10 PPI SiSiC foam	2.39
10 PPI CoCr foam	2.39
10 PPI CoCr lattice	3.17

Operational regime during the experiment ($\phi = 0.6$; $V = 34.6$ *cm/s*) provided similar pressure drop values ($\Delta p \approx 11\ Pa$) for setups #4, #5, and #6 (see Figure 3.3). Pressure drop is often presented in this way in the literature, since average pore diameter is usually unknown. However, thanks to Re based on the average pore diameter—the advanced measurement technique used herein—this number was used to illustrate the difference in the geometric characteristics of each porous media (PM) on flow.

The convenience in considering Re rather than velocity is that flow characteristics in PM are, in general, characterized and identified by Re, which allows us to distinguish between different flow regimes (Darcy, Forchheimer, etc.). Thus, Figure 3.4 illustrates the same results as Figure 3.3, but shows pressure drop as a function of Re. Contrary to Figure 3.3,

where few differences were observed in a pressure drop for any given velocity, Figure 3.4, which used Re, shows that setup #6 had lower pressure drop values at equivalent Re when compared to setups #4 and #5 (foam in SiSiC and its replica in CoCr, respectively). Combustion tests were conducted at a constant inlet velocity, which resulted in a higher Re for setup #6 and, in turn, increased heat transfer by convection. Higher heat transfer by convection for setup #6 impacted the burner temperature profile which might in part explain the higher temperature observed in Figure 3.3 for that setup. Nevertheless, more experiments and numerical simulations are needed to confirm this hypothesis.

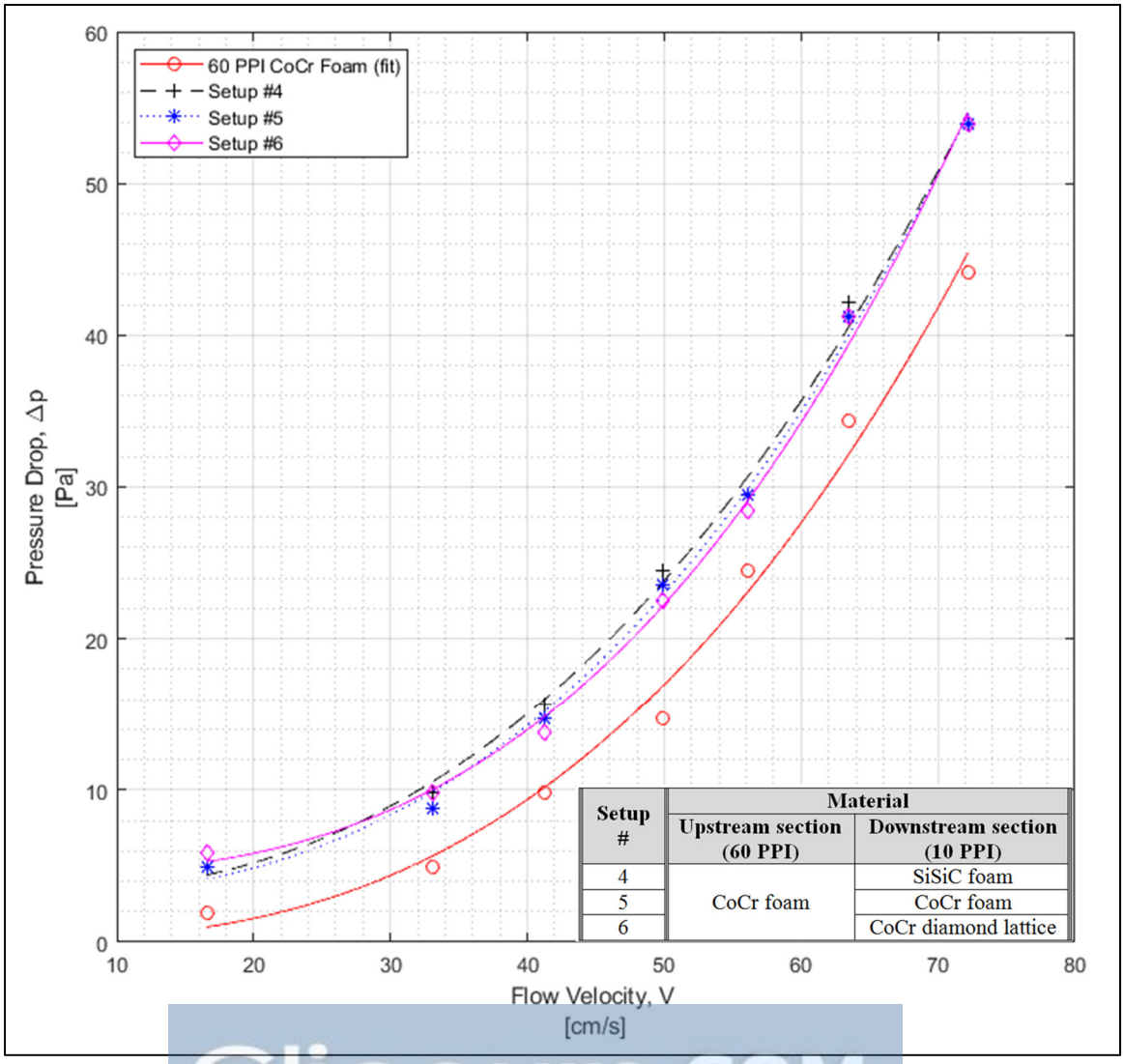

Setup #	Material	
	Upstream section (60 PPI)	Downstream section (10 PPI)
4	CoCr foam	SiSiC foam
5		CoCr foam
6		CoCr diamond lattice

Figure 3.3 Δp versus V: 60 PPI CoCr Foam, and setups #4, #5, #6

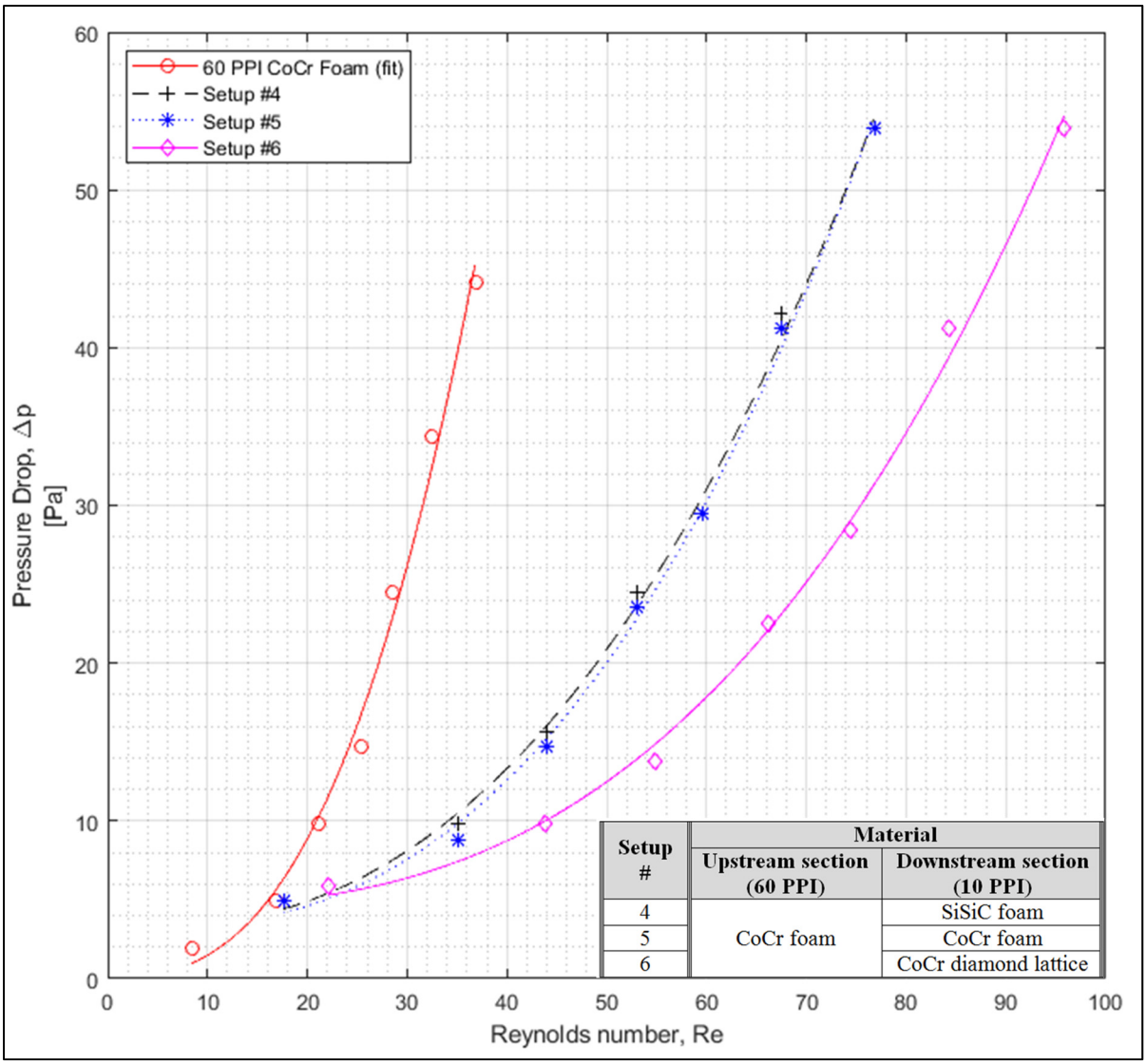

Setup #	Material	
	Upstream section (60 PPI)	Downstream section (10 PPI)
4	CoCr foam	SiSiC foam
5		CoCr foam
6		CoCr diamond lattice

Figure 3.4 Δp versus Re: 60 PPI CoCr Foam, and setups #4, #5, #6

Figure 3.5 demonstrates a comparison of pressure gradient results for 60 PPI CoCr between measured values and the values obtained according to Eq. (2.17). Both results demonstrated the same trends, though when compared to (B. Dietrich et al., 2009), suggested overpredicted values [for calculations, the $d_{h,c}$ of the 60 PPI CoCr specimen was evaluated according to Eqn. (2.17), such that S_v was evaluated from the adjusted value in VG 60 PPI SiSiC (#1) foam to the appropriate porosity ($\varepsilon = 75.2$ %)]. This result demonstrates that geometry plays an important role on flow parameters for structures like foams, which have high discrepancies in their morphologies, even for specimens with similar PPI.

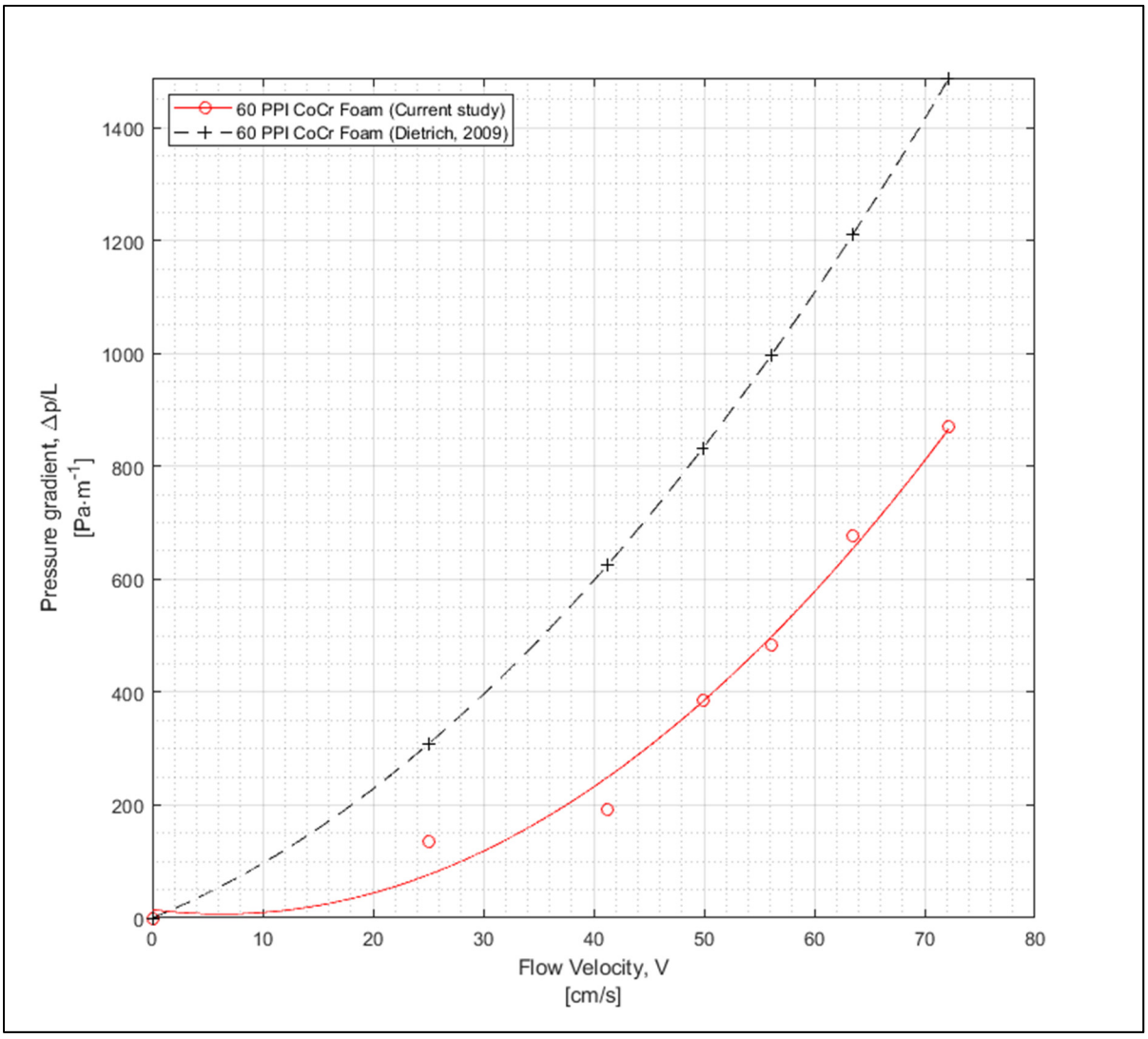

Figure 3.5 *Δp/L*: Comparing the results of the current study and those of B. Dietrich et al. (2009)

3.1.5 Structural durability

After the burning tests, specimens were examined based on their structural differences. Material oxidation was observed under high temperature conditions. Results from before and after the tests are presented in Figure 3.6. Due to oxidation, material degradation in the CoCr materials resulted in the formation of residual particles. In SiSiC specimens, oxidation was

characterized only by a change in the colour of the material. 60 PPI CoCr foam, however, was not susceptible to deterioration, since it was not exposed to high temperatures.

Figure 3.7a demonstrates that ceramic foams with small pores (60 PPI) were subject to structural damage as a result of thermal shock during unstable operation and flame propagation towards the inlet section, in contrast to the undamaged specimens with large pores (10 PPI). This finding agrees with the results obtained by V. R. Vedula et al. (1999), where it was found that ceramic foams with small pores are more susceptible to structural failure.

Table 2.1 demonstrates a comparison between SiSiC and CoCr materials in terms of thermal shock resistance (R) and fracture toughness (K_{1C}). Although 60 PPI CoCr foam was not subject to high temperatures during the experiments, perhaps the CoCr alloy possesses superior properties for resisting thermal shock (R for CoCr is almost twice that of SiSiC) and crack propagation (the K_{1c} of CoCr is 50 times higher than the K_{1c} of SiSiC). Thus, CoCr material might be beneficial for application in the upstream section to reduce the possibility of structural damage. This theory should be examined in future research.

After burning tests due to temperature gradients, 10 PPI CoCr foam became distorted, whereas the 10 PPI CoCr Diamond lattice kept its original form (see Figure 3.7b). According to the findings of (N. A. Fleck, 2004), this is due to the higher stiffness and higher initial yield strength of the diamond lattice when compared to foam-like structures.

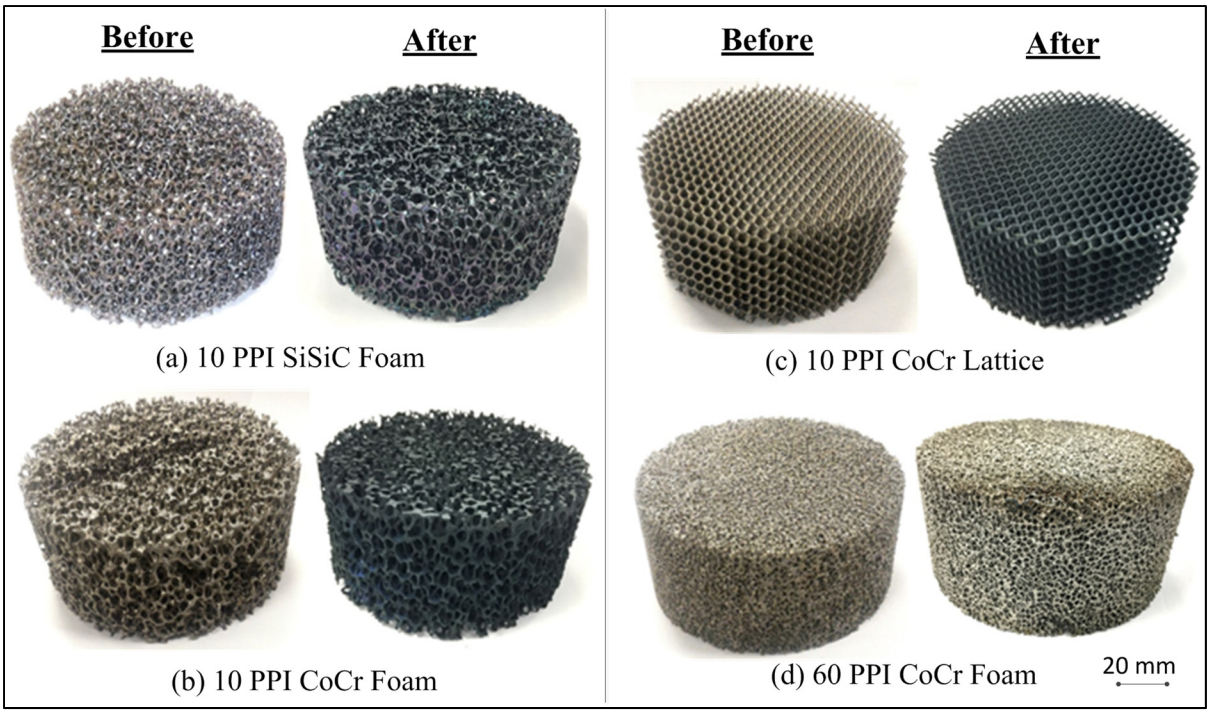

Figure 3.6 Oxidation of *SiSiC* and *CoCr* materials after operation in PMB

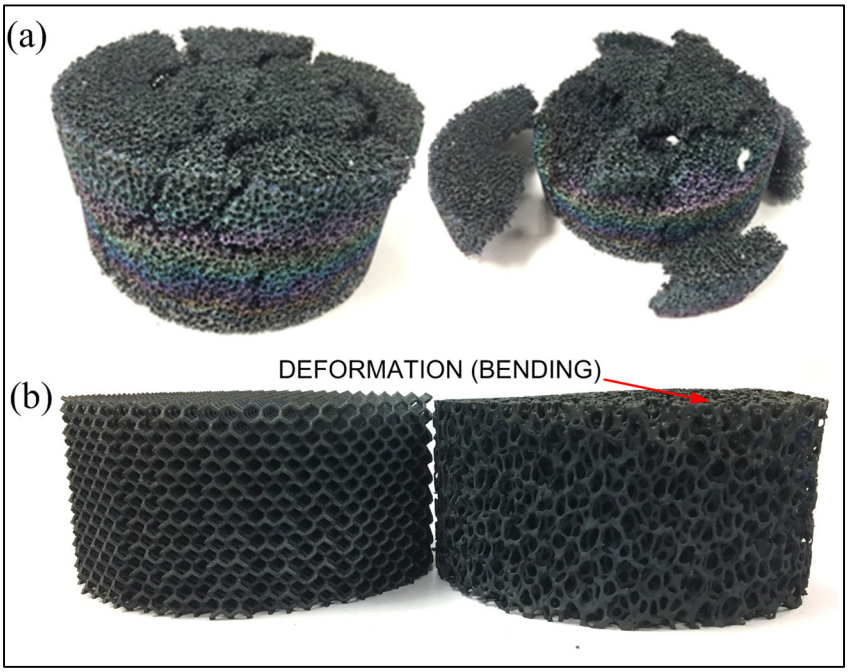

Figure 3.7 Failures after operation:
(a) SiSiC: crack formation of the 60 PPI foam;
(b) CoCr: Deformation, comparison between
the 10 PPI *lattice* and *foam* structures

By comparing the structural durability of the diamond lattice with that of conventional ceramic foams, we found that the diamond lattice geometry made of the metal CoCr material provided higher structural stiffness and superior resistance to thermal shock and crack propagation. However, due to CoCr oxidation under extreme temperatures, its application might be limited exclusively to the upstream region.

3.2 Summary of the experimental results

This chapter described our PMB combustion experiment through our six setups, which had the same operational regime ($\phi = 0.6$; $S_L = 34.6\, cm/s$). This regime examined the applicability of tailored diamond lattice geometries and metal CoCr materials. We examined this by taking measurements of the temperature, pollutant emissions, and pressure drop.

From our experiments, we found that CoCr had a more beneficial application in the upstream section than ceramic SiSiC, and resulted in a more stable and safer operation. Setup with SiSiC material in the upstream section resulted in flame propagation towards the inlet section without being quenched, which resulted in flashback. Moreover, CoCr provided higher resistance to thermal shock. Experimentally, we found that after operation the diamond lattice had no distortions when compared to the foam geometry, which demonstrated its higher structural rigidity. Through pressure drop measurements, we found that absolute permeability for foam and diamond lattice geometries was similar. However, it was determined that in terms of flame stabilization, Reynolds number (Re) [which is a function of pore diameter (d_p)] plays a crucial role, and should be taken into consideration during the design of diamond lattices.

An important part of the research was to provide measurements of CO, NO_x, and CH_4 levels which demonstrated an almost pollution-free operation in all experimental setups. This finding supports the results of previous research experiments (C. Keramiotis et al., 2012; W. M. Mathis & J. L. Ellzey, 2003). Our findings also suggested emission levels which were lower than those of open-flame burners (C.-Y. Wu, K.-H. Chen, & S. Y. Yang, 2014).

CONCLUSION

The primary objective of this work was to design PMB and to investigate the potential benefits of using AM by replacing an irregular foam with a regular diamond lattice. As a result, six experimental setups were created and tested, and subsequently compared in terms of their pollutant emissions and operational stability.

Conventional ceramic, sponge-like foams were acquired, and methods of foam analysis were investigated to define their main physical characteristics. We conducted our investigation using CT scan technology, which allowed us to obtain geometric parameters (porosity, pore size, strut thickness, etc.) as well as absolute permeabilities [by means of VGStudio Max software (VG)]. From this analysis, the geometric properties of the equivalent diamond lattice parameters were proposed.

Through foam analysis, it was determined that PPI value (the main parameter indicated by a manufacturer that represents pore diameter) provided underestimated results when compared to the actual measurements. Based on the results of manual pore size measurements from digitally reconstructed parts and correlations of absolute permeability on pore size, the combination of the developed tetrakaidecahedron model and the adapted method of cell size analysis ($d_{c,cs}$) by D3576-15 ASTM (2015) lead to favourable determination of pore diameter ($d_{p,cs}$) among the examined methods. Study of ceramic foams confirmed the complexity and discrepancies between geometries that have identical PPI value. Thus, from the manufacturer's point of view, regular diamond lattices should be favoured for their high repeatability. Finally, equivalent parameters of diamond lattices were obtained and corresponding structures have been proposed for LPBF using CoCr, which has the highest operational temperature of the available metals and for the LPBF equipment available in our laboratory.

The test bench was designed and assembled to allow for the measurements of temperature, pollutant emissions, and pressure drop. To examine the influence of CoCr material in the

upstream and downstream sections on the burner's pollutant emissions and operational stability, as well as to verify equivalency between foam and diamond lattice geometries, three specimens were prepared and printed: 10 PPI foam, 10 PPI equivalent diamond lattice, and 60 PPI foam.

Through our obtained data, we confirmed a PMB operation with low pollutant emissions and detailed the potential applications of AM (or 3D printing) in PMB design. The replacement of foam geometry with that of a diamond lattice might better predict the combustion processes by numerical methods. From the operational point of view, high PPI metal (CoCr) material was favourable in the *upstream* section. During experiments at steady state conditions, using high PPI SiSiC material in the *upstream* section resulted in a constant temperature increase in the medium followed by flame propagation towards the upstream region. This was attributed to the high thermal conductivity of the SiSiC matrix and excessive heat transfer from the downstream section to the upstream section. In contrast, using high PPI CoCr material in the *upstream* section resulted in better performance as a flame arrestor (as it did not allow flame propagation towards the upstream section) and better operational stability, since it shifted the flame front towards the downstream section. For the *downstream* region, applying low PPI SiSiC material was favourable because of the material's high temperature operational limit and higher heat transfer properties.

RECOMMENDATIONS

1) From the above-mentioned results, we recommend using AM to produce diamond lattices with high PPI metal (CoCr) material in the *upstream* section and low PPI ceramic (SiSiC) material in the d*ownstream* section. We recommend manufacturing high PPI CoCr diamond lattice using the LPBF method. Low PPI SiSiC diamond lattice, on the other hand, might be manufactured using a hybrid method: firstly, 3D-print its shape from the polymer and then apply the conventional ceramic replication technique (A. Ortona, C. D'Angelo, et al., 2012).

2) Another field of improvement in PMB design lies in the development of a multi-stage structure with gradient pore size distribution. Appropriate numerical models should be devised to find the optimized diamond lattice parameters. In this case, AM represents the optimal solution for the production of such complex geometries with a high level of accuracy.

3) Future research could investigate lattices of various unit cell types. A tetrakaidecahedron is a structure that has promising potential for future research. One of its advantages, in comparison with the diamond lattice, is that it has a higher specific surface and the same pore size, which is favourable for both flame quenching and heat transfer.

4) Current research is limited to one operational regime (flame velocity and equivalence ratio), thus the determination of stability limits at various equivalence ratios should fuel future research.

5) CoCr material in the upstream section was found to be beneficial, and ensured better flame stability. It would be interesting to verify the assumption of higher CoCr durability to thermal shock and crack propagation by exposing it to high temperature gradients in the upstream section.

6) The measured values of pollutant emissions were at the detection limits. More precise equipment would help us to investigate the influence of material types and geometric parameters.

7) Permeability results and derived correlations were based on VGStudio Max software, and discrepancies between various research efforts were observed. Therefore, it is of interest to validate the obtained data with the experimental data. To reduce the cost, we propose printing experimental structures from polymer materials, and only afterwards taking pressure drop measurements.

APPENDIX I

TETRAKAIDECAHEDRON MODEL

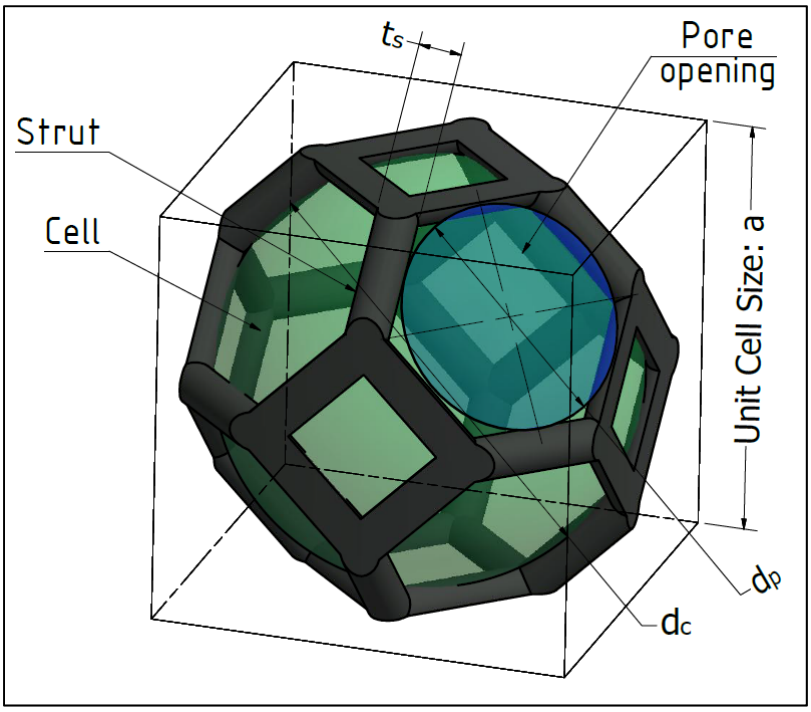

Figure-A I-I Tetrakaidecahedron unit cell

This section explains the main relationships characterizing tetrakaidecahedron unit cells. (W. Xu et al., 2008) defines pore size as an equivalent pore diameter (d_p) of the circle with an area, equal to the hexagon opening:

$$d_p = \sqrt{4A_{hex}/\pi} \tag{A I-1}$$

In this approach, however, additional square openings are not considered (A_{sq}), and so a better correlation was obtained by using:

$$d_{p,eq} = \sqrt{4A_{eq}/\pi} \tag{A I-2}$$

where,

$$A_{eq} = \frac{8A_{hex} + 6A_{sq}}{14} \tag{A I-3}$$

Analytically it might be found that:

$$A_{hex} = 2\sqrt{3}\left(a\frac{\sqrt{3}}{4\sqrt{2}} - \frac{t_s}{2}\right)^2 \quad \text{(A I-4)}$$

$$A_{sq} = \left(\frac{a}{2\sqrt{2}} - t_s\right)^2 \quad \text{(A I-5)}$$

And finally:

$$d_{p,eq} = \sqrt{\frac{6\left(\frac{a}{2\sqrt{2}} - t_s\right)^2 + 16\sqrt{3}\left(\frac{\sqrt{3}a}{8} - \frac{t_s}{2}\right)^2}{\pi}} \quad \text{(A I-6)}$$

Correlations for porosity (ε), cell diameter (d_c) and equivalent pore diameter ($d_{p,eq}$) were obtained as functions of unit cell size a and strut thickness (t_s). This approach was based on the combination of CAD modelling and MATLAB's "Curve fitting tool". Correlations were carried out for porosities $\varepsilon \geq 0.7$, which lie in the range of investigated ceramic foams.
Solid volume of the tetrakaidecahedron unit cell V_s is found from $V_s/a^3 = f(t_s/a)$ as:

$$V_s = 3.421a^3\left(\frac{t_s}{a}\right)^{1.754} \quad \text{(A I-7)}$$

Thus porosity of the unit cell ε is found as:

$$\varepsilon = 1 - 3.421\left(\frac{t_s}{a}\right)^{1.754} \quad \text{(A I-8)}$$

Volume of the tetrakaidecahedron cell V_c (not to be confused with the unit cell) is found as:

$$V_c = a^3(\varepsilon - 0.5) \quad \text{(A I-9)}$$

If we consider the volume of the sphere to be equal to the volume of the cell, then the cell diameter (d_c) is found as:

$$d_c = a\sqrt[3]{\frac{6(\varepsilon - 0.5)}{\pi}} \quad \text{(A I-10)}$$

Equivalent pore diameter $d_{p,eq}$ is found from $\frac{d_{p,eq}}{d_c} = f(\varepsilon)$ as:

$$d_{p,eq} = d_c(0.1306\varepsilon^{12.28} + 0.4114) \quad \text{(A I-11)}$$

In cases where the measurements are limited only by porosity ($0.7 < \varepsilon < 0.94$) and strut thickness, equivalent pore diameter might be found from $\frac{d_{p,eq}}{t_s} = f(\varepsilon)$ as:

$$d_{p,eq} = t_s(0.0869e^{3.723\varepsilon} + 1.995 \cdot 10^{-9}e^{21.79\varepsilon}) \quad \text{(A I-12)}$$

It should be noted that solutions were obtained for struts with circular cross-sections, so coefficients for other geometries may vary slightly.

For evaluation purposes, the number of pores in the tetrakaidecahedron lattice might be found as:

$$N_{pores,tetr} = 14n_xn_yn_z - (n_x + n_y + n_z - 3) \quad \text{(A I-13)}$$

where n_x, n_y, n_z – number of unit cells in *x*-, *y*-, *z*-directions.

APPENDIX II

DIAMOND LATTICE MODEL

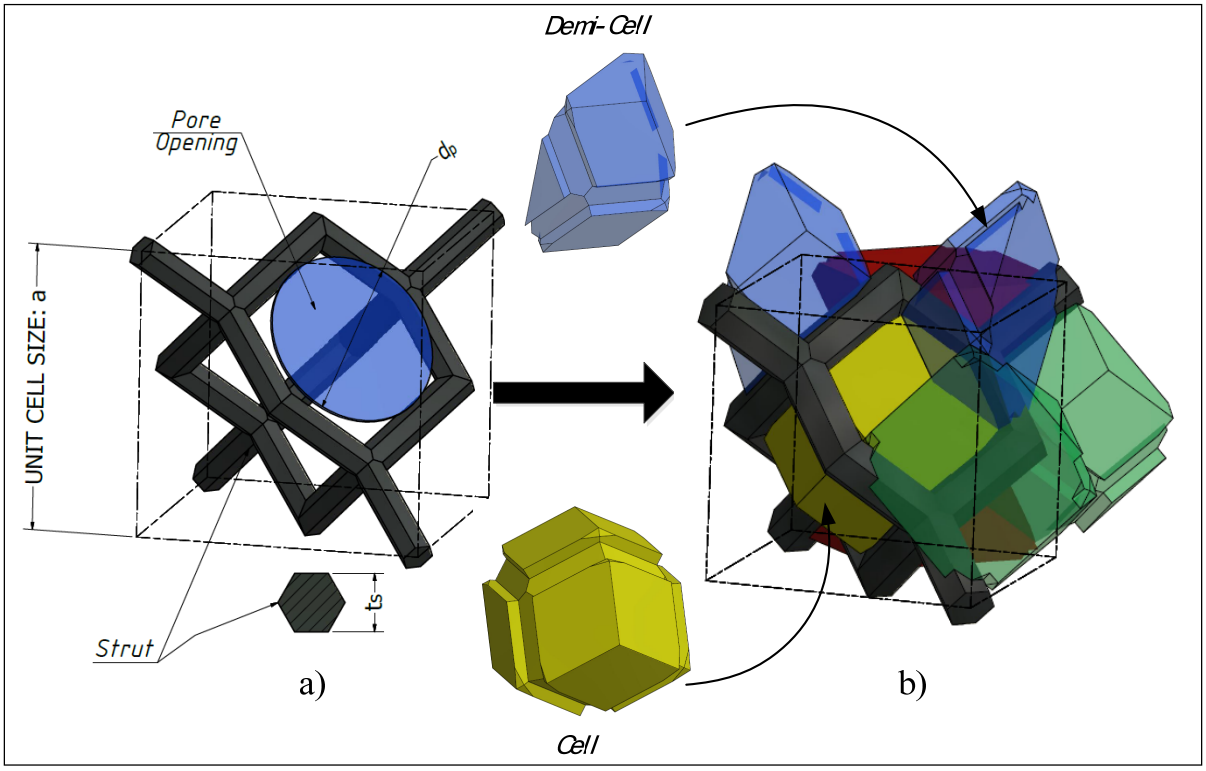

Figure-A II-I a) Diamond unit cell; b) Diamond "unit cell" with "cell" and "demi-cells"

This section explains the primary relationships characterizing a diamond lattice unit cell. Assumptions according to d_p are the same as in APPENDIX I (p. 95).

The MATLAB code, which generated our diamond lattice structure, was taken from the works of (M. Dumas, 2016). For this structure (see Figure-A II-I) hexagonal cross-sections of struts were used. Additionally, a distinction between *"unit cell"* (which represents a cubic repetitive volume in lattice) and *"cell"* (which is represented as inscribed between struts volume) should be understood. In a diamond lattice, each *"unit cell"* consists of a total of four *"cells"* (one inscribed in the centre, and six demi-cells, which are required for filling the volume during patterning).

Therefore, the total number of cells ($N_{cell,tot}$) might be defined as:

$$N_{cell,tot} = 4n_x n_y n_z \tag{A II-1}$$

where n_x, n_y, and n_z are the number of unit cells in the *x*-, *y*-, and *z*-directions.

For the evaluation of fully enclosed cells in the structure ($N_{cell,tot,cl}$) without considering open edges, the solution was found as:

$$N_{cell,tot,cl} = 4n_x n_y n_z - 2\left(n_x n_y + n_x n_z + n_y n_z\right) + (n_x + n_y + n_z) \tag{A II-2}$$

Each cell consists of four pores, and so by knowing the total number of cells, the total number of pores ($N_{pore,tot}$) in the diamond lattice can be evaluated as:

$$N_{pore,tot} = 4N_{cell,tot,cl} \tag{A II-3}$$

Total volume of the diamond lattice solid ($V_{s,tot,lat}$) is found as:

$$V_{s,tot,lat} = V_{s,uc} \cdot n_{uc,tot} \tag{A II-4}$$

where $V_{s,uc}$ is the solid volume of the unit cell and $n_{uc,tot}$ is the total number of *"unit cells"*, which found as:

$$V_{s,uc} = \frac{2t_s^2[3\sqrt{2}a\sec\beta - 7t_s\tan\beta]}{\sqrt{3}} \tag{A II-5}$$

$$n_{uc,tot} = n_x n_y n_z \tag{A II-6}$$

where t_s – strut thickness and $\beta = \tan^{-1}(\frac{1}{\sqrt{2}})$

By assuming that cell volume equals to the volume of the sphere, cell diameter d_c is found as:

$$d_c = \sqrt[3]{6V_C/\pi} \tag{A II-7}$$

where,

$$V_c = (a^3 - V_{s,uc})/4 \tag{A II-8}$$

Porosity (ε) of the whole structure is found as:

$$\varepsilon = 1 - \frac{V_{s,uc}}{a^3} \tag{A II-9}$$

Simplified relationship for porosity in terms of cell size and strut thickness:

$$\varepsilon_{lat} = 1.004 - 2.908\left(\frac{t_s}{a}\right)^{1.64} \quad \text{(A II-10)}$$

The total volume of the diamond lattice finally might be found as

$$V_{s,tot} = n_{uc,tot} \cdot V_{s,uc} \quad \text{(A II-11)}$$

Applying the principles described in APPENDIX I (p. 95), pore diameter ($d_{p,lat}$) is found from $\frac{d_{p,lat}}{a} = f(\frac{t_s}{a})$ as:

$$d_{p,lat} = 0.744a - 1.217t_s \quad \text{(A II-12)}$$

Dependence of the outer surface for unit cell is found as:

$$S_{surf,uc} = a^2\left(8.94\left(\frac{a}{t_s}\right)^{-0.44} - 1.07\right) \cdot 10^{-6}\ [m^2] \quad \text{(A II-13)}$$

The outer surface of the rectangular diamond lattice is found as:

$$S_{surf} = a^2\left(8.94\left(\frac{a}{t_s}\right)^{-0.44} - 1.07\right) \cdot 10^{-6} n_x n_y n_z [m^2] \quad \text{(A II-14)}$$

Specific surface $S_v = S_{surf}/V_{tot}$ is found as:

$$S_v = \frac{0.02083\left(\frac{a}{t_s}\right)^2 - 0.5697\left(\frac{a}{t_s}\right) + 5.643}{a}\ [m^{-1}] \quad \text{(A II-15)}$$

Therefore, by defining the number of unit cells in *x*-,*y*-,*z*-direction, unit cell size a and strut thickness (t_s), the main geometric parameters of diamond lattice may be obtained.

APPENDIX III

ADDITIONAL METHODS OF FOAM ANALYSIS

a) Ceramic foam manufacturers use PPI and d_p values that are taken from the producers of polymer foams. In turn, the latter usually define them according to their own internal test methods (FXI, 2014). Figure-A III-I shows dependence of average pore diameter on pore size.

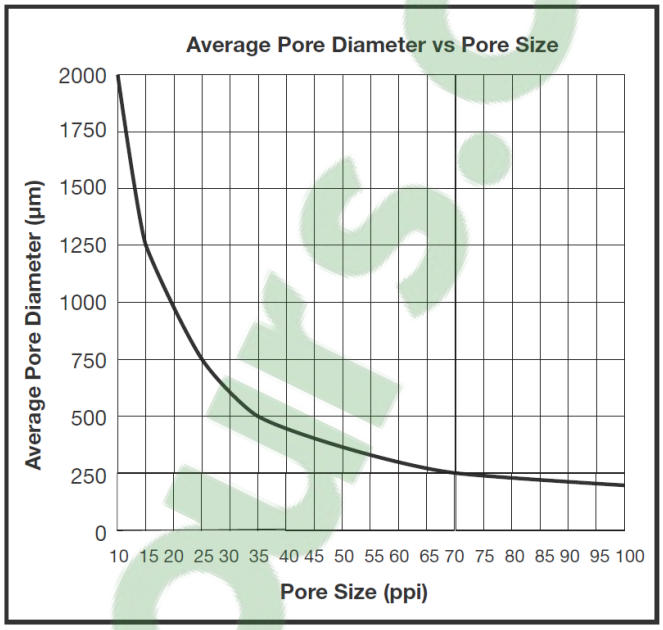

Figure-A III-I Average Pore Diameter vs Pore Size
Taken from (FXI, 2014)

From Figure-A III-I it might be obtained relationship $d_p = f(PPI)$ as:

$$d_p = \frac{17.7}{PPI - 1.4}\ [mm] \qquad \text{(A III-1)}$$

b) Assuming the pores are cylindrical and of uniform pore distribution, X. Fu et al. (1998) proposed the definition of the mean pore diameter by knowing PPI and the porosity of the foam:

$$d_p = 25.4\frac{\sqrt{4\varepsilon/\pi}}{\omega} \qquad \text{(A III-2)}$$

c) Assuming the tetrakaidecahedron unit cell with triangular strut cross-section, L. J. Gibson and M. F. Ashby (1988) proposed the definition of d_p based on strut thickness (t_s) and porosity (ε):

$$d_p = \frac{t_S[1 - 0.971(1-\varepsilon)^{0.5}]}{0.5338(1-\varepsilon)^{0.5}} \quad \text{(A III-3)}$$

d) According to J.-F. Despois and A. Mortensen (2005) d_p is defined as:

$$d_p = d_c\sqrt{\frac{\varepsilon - 0.64}{1.08}} \quad \text{(A III-4)}$$

Table-A III-1 Comparison of various methods for finding pore diameters

Parameter	Method	Pore Density, PPI					
		10 PPI		30 PPI		60 PPI	
		#1	#2	#1	#2	#1	#2
Open Porosity ($\varepsilon_{tot,VG}$), [%]	e)	85.61	84.77	81.37	74.80	87.71	89.34
Strut thickness (t_s), [mm]	f)	0.94	0.98	0.69	0.91	0.42	0.39
d_p, [mm]	a)	2.0		0.619		0.302	
	b)	2.66	2.64	0.86	0.82	0.45	0.45
	c)	2.93	2.92	1.74	1.74	1.48	1.53
	d)	2.48	2.59	1.19	0.85	0.97	1.14

a) (FXI, 2014)
b) (X. Fu et al., 1998)
c) (L. J. Gibson & M. F. Ashby, 1988)
d) (J.-F. Despois & A. Mortensen, 2005)
e) VGStudio MAX 3.0 (see section 2.2.2.1).
f) Analysis of image cross-sections (see section 2.2.2.2).

APPENDIX IV

TEST BENCH: OVERALL DIMENSIONS

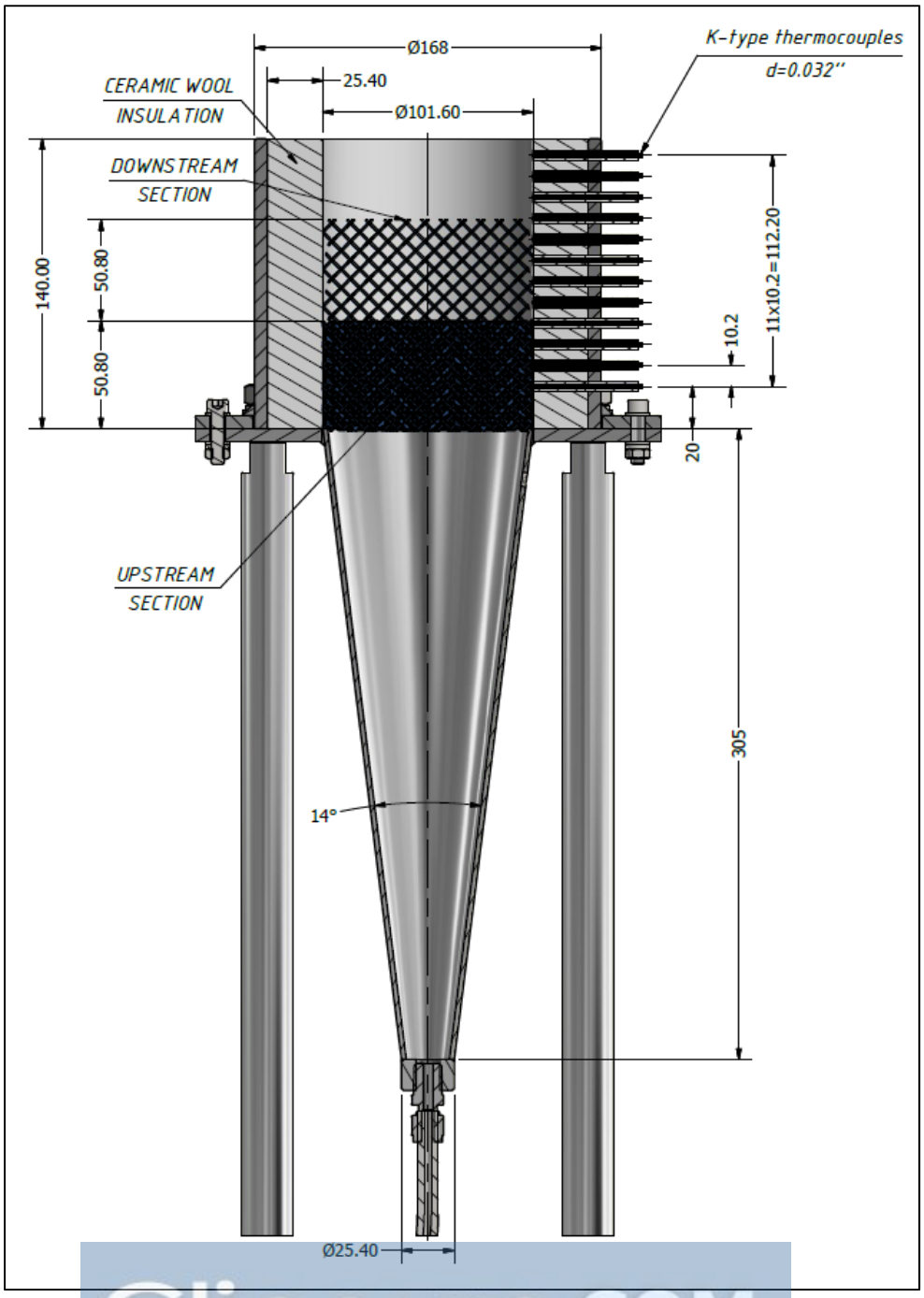

Figure-A IV-I Test bench overall dimensions

APPENDIX V

USED EQUIPMENT AND UNCERTAINTY ANALYSIS

Uncertainty analysis of equipment (u_c) has been calculated according to R. S. Figliola and D. E. Beasley (2011) as:

$$u_c = \sqrt{u_1^2 + u_2^2 + \cdots + u_k^2} \tag{A V-1}$$

where u_k is the uncertainty of some *k*-element of error.

List of used equipment with corresponding instrumental uncertainties is presented in Table-A V-1. Uncertainties for each gas analyzer were calculated according to Eqn. (A V-1) based on linearity and repeatability errors.

List of used concentrations of span gases is presented in Table-A V-2.

Table-A V-1 List of equipment's operation range and accuracy

Parameter	Equipment	Full scale	Instrument uncertainty*
Mass flow controllers			
Air	Azbil MFC MQV0200	0–200 *lpm*	± 1 *%* (± 2 *lpm*)
	Cole-Parmer IRF RK-32900-54	10–100 *lpm*	± 4 *%* (± 4 *lpm*)
CH_4	Omega FMA 5400/5500	0–15 *lpm*	± 1.5 *%* (± 0.225 *lpm*)
	Omega FMA 5400/5500	0–15 *lpm*	± 1.5 *%* (± 0.225 *lpm*)
Gaz analyzers			
CO	CAI Model 200	0–10 *%*	± 0.17 *%*
NO_x	CAI 600 Series	0-50 *ppm*	± 0.43 *ppm*
CH_4	CAI 600 Series	0-200 *ppm*	± 1.73 *ppm*
CO_2	ABB Multifid URAS 14	0–30 *%*	± 0.45 *%*
O_2		0–100 *%*	± 1.73 *ppm*
Thermocouples			
Temperature	Omega K-type (d=0.032'')	273-1523 *K*	max ± 9.4 *K*

Uncertainties according to flame speed (E_S) and equivalence ratio (E_ϕ) were calculated according to H. Gao, Z. Qu, W. Tao, Y. He, and J. Zhou (2011) as:

$$E_S = \left[\left(\frac{\partial S}{\partial \dot{V}}\partial\dot{V}\right)^2 + \left(\frac{\partial S}{\partial A}\delta A\right)^2\right]^{\frac{1}{2}}/S \quad \text{(A V-2)}$$

$$E_\phi = \left[\left(\frac{\partial \phi}{\partial \dot{V}_{CH_4}}\partial\dot{V}_{CH_4}\right)^2 + \left(\frac{\partial \phi}{\partial \dot{V}_{air}}\partial\dot{V}_{air}\right)^2\right]^{\frac{1}{2}}/\phi \quad \text{(A V-3)}$$

Flame speed

$A = 81.07\ [cm^2]$

$\delta A = \frac{\pi(0.1)^2}{4} = 7.85 \cdot 10^{-3}\ [cm^2]$

$S = 34.6\ [\frac{cm}{s}]$

$\dot{V}_{max} = 168.23\ \left[\frac{L}{min}\right] = 2803.83\ [\frac{cm^3}{s}]$

$\frac{\partial S}{\partial \dot{V}} = \frac{1}{A} = 1.23 \cdot 10^{-2}\ [cm^{-2}]$

$\frac{\partial S}{\partial A} = -\dot{V}_{max}\left(\frac{1}{A^2}\right) = -0.427\ [cm^{-1}s^{-1}]$

$\partial\dot{V} = \sqrt{(\partial\dot{V})^2_{air,1} + (\partial\dot{V})^2_{air,2} + (\partial\dot{V})^2_{CH_4,1} + (\partial\dot{V})^2_{CH_4,2}} = \sqrt{2^2 + 4^2 + 2 \cdot 0.225^2} =$

$= 4.48\ \left[\frac{L}{min}\right] = 74.72\ [\frac{cm^3}{s}]$

Finally, the uncertainty according to flame speed (E_S) is calculated as:

$E_S = [(1.23 \cdot 10^{-2} \cdot 74.72)^2 + (-0.427 \cdot 7.85 \cdot 10^{-3})^2]^{\frac{1}{2}}/34.6 \cdot 100\% = 2.66[\%]$

Equivalence ratio

$$\dot{V}_{air,max} = 158.28\ [\frac{L}{min}]$$
$$\dot{V}_{CH_4,max} = 9.95\ [\frac{L}{min}]$$

$$\frac{\partial \phi}{\partial \dot{V}_{CH_4}} = 9.48 \frac{1}{\dot{V}_{air,max}} = 5.99 \cdot 10^{-2}\ [\frac{min}{L}]$$

$$\frac{\partial \phi}{\partial \dot{V}_{air}} = -9.48 \left(\frac{\dot{V}_{CH_4,max}}{\dot{V}^2_{air,max}}\right) = -0.38 \cdot 10^{-2}\ [\frac{min}{L}]$$

$$\partial \dot{V}_{air} = \sqrt{2^2 + 4^2} = 4.47\ [\frac{L}{min}]$$

$$\partial \dot{V}_{CH_4} = \sqrt{0.225^2 + 0.225^2} = 0.32\ [\frac{L}{min}]$$

Finally, the uncertainty according to equivalence ratio (E_ϕ) is calculated as:

$$E_\phi = [(5.99 \cdot 10^{-2} \cdot 0.32)^2 + (-0.38 \cdot 10^{-2} \cdot 4.47)^2]^{\frac{1}{2}} / 0.6 \cdot 100\% = 2.54\ [\%]$$

Table-A V-2 Used concentrations of span gases

Gas type	Equipment	Span gas
CO	CAI Model 200	0.24 *%*
NO_x	CAI 600 Series	39.8 *ppm*
CH_4	CAI 600 Series	160 *ppm*
CO_2	ABB Multifid URAS 14	30 *%*
O_2		20.95 *%*

APPENDIX VI

WIRING DIAGRAM

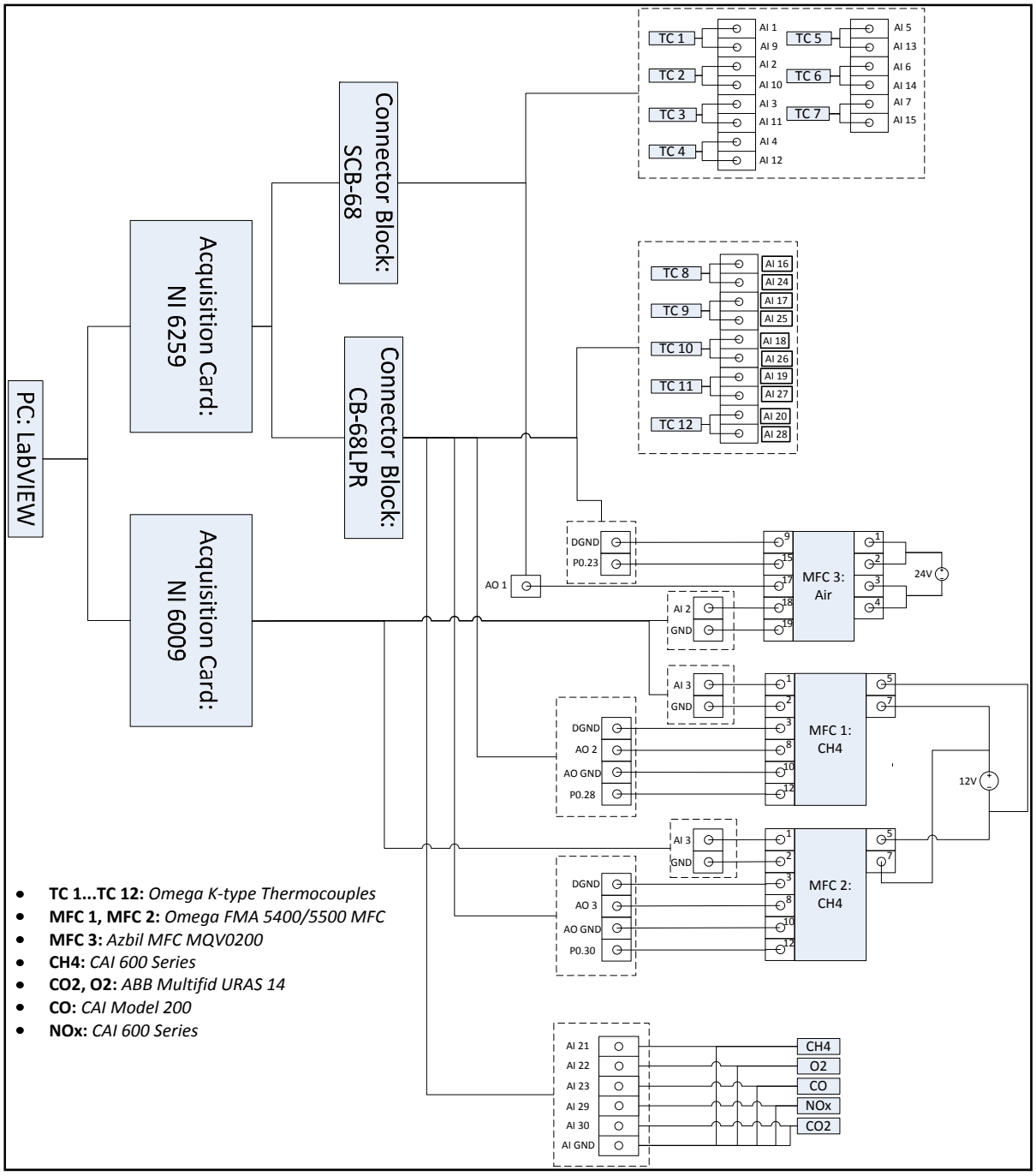

Figure-A VI-I Test bench wiring diagram

LIST OF BIBLIOGRAPHICAL REFERENCES

Ahearne, E., Baron, S., Keaveney, S., & Byrne, G. (2015). *An Assessment of Medical Grade Cobalt Chromium Alloy ASTM F1537 as a Difficult-to-Cut (DTC) Material.* Paper presented at the Proceedings of Machine Tool Technology Research Foundation.

Alavandi, S. K., & Agrawal, A. K. (2008). Experimental study of combustion of hydrogen–syngas/methane fuel mixtures in a porous burner. *International journal of hydrogen energy, 33*(4), 1407-1415.

ASTM International. (2015). *Standard Test Methods for Density of Compacted or Sintered Powder Metallurgy (PM) Products Using Archimedes' Principle*. Standard ASTM B962-15. West Conshohocken, PA: ASTM International.

ASTM International. (2015). *Standard Test Method for Cell Size of Rigid Cellular Plastics*. Standard ASTM D3576-15. West Conshohocken, PA: ASTM International.

ASTM International. (2017). *Standard Terminology Relating to Plastics*. Standard ASTM D883-17. West Conshohocken, PA: ASTM International.

Avdic, F. (2004). *Application of the porous medium gas combustion technique to household heating systems with additional energy sources.* (PhD), Universität Erlangen-Nürnberg.

Babkin, V. S., Korzhavin, A. A., & Bunev, V. A. (1991). Propagation of Premixed Gaseous Explosion Flames in Porous Media. *Combustion and flame, 87*, 182-190.

Barra, A. J., Diepvens, G., Ellzey, J. L., & Henneke, M. R. (2003). Numerical study of the effects of material properties on flame stabilization in a porous burner. *Combustion and flame, 134*(4), 369-379.

Barra, A. J., & Ellzey, J. L. (2004). Heat recirculation and heat transfer in porous burners. *Combustion and flame, 137*(1), 230-241.

Baukal Jr., C. E. (2012). *The john zink hamworthy combustion handbook: Volume 1-Fundamentals*: CRC press.

Bechtold, J. K., & Matalon, M. (2001). The dependence of the Markstein length on stoichiometry. *Combustion and flame, 127*(1), 1906-1913.

Boomsma, K., & Poulikakos, D. (2001). The Effects of Compression and Pore Size Variations on the Liquid Flow Characteristics in Metal Foams. *Journal of Fluids Engineering, 124*(1), 263-272.

Bose, N. R. (2013). Thermal shock resistant and flame retardant ceramic nanocomposites *Ceramic Nanocomposites* (pp. 3-50): Elsevier.

Buckmaster, J., & Takeno, T. (1981). Blow-Off and Flashback of an Excess Enthalpy Flame. *Combustion Science and Technology, 25*, 153-158.

CeramTec Rocar® SiF Silicon Carbide, SiSiC. (2018). Retrieved from http://www.matweb.com/search/datasheet.aspx?MatGUID=8d3ace18a3074b6fae4bd7b435df3956

Conner, B. P., Manogharan, G. P., Martof, A. N., Rodomsky, L. M., Rodomsky, C. M., Jordan, D. C., & Limperos, J. W. (2014). Making sense of 3-D printing: Creating a map of additive manufacturing products and services. *Additive Manufacturing, 1-4*, 64-76.

Despois, J.-F., & Mortensen, A. (2005). Permeability of open-pore microcellular materials. *Acta Materialia, 53*(5), 1381-1388.

Dietrich, B., Schabel, W., Kind, M., & Martin, H. (2009). Pressure drop measurements of ceramic sponges—Determining the hydraulic diameter. *Chemical Engineering Science, 64*(16), 3633-3640.

Dikici, B., Pantoya, M. L., & Levitas, V. (2010). The effect of pre-heating on flame propagation in nanocomposite thermites. *Combustion and flame, 157*(8), 1581-1585.

Djordjevic, N., Habisreuther, P., & Zarzalis, N. (2009). *Experimental study on the influence of the pore size of SiSiC sponge on the flame stabilization in a porous burner.* Paper presented at the 4th European Combustion Meeting.

Djordjevic, N., Habisreuther, P., & Zarzalis, N. (2011). A numerical investigation of the flame stability in porous burners employing various ceramic sponge-like structures. *Chemical Engineering Science, 66*(4), 682-688.

Djordjevic, N., Habisreuther, P., & Zarzalis, N. (2012a). Experimental Study on the Basic Phenomena of Flame Stabilization Mechanism in a Porous Burner for Premixed Combustion Application. *Energy & Fuels, 26*, 6705–6719.

Djordjevic, N., Habisreuther, P., & Zarzalis, N. (2012b). Porous Burner for Application in Stationary Gas Turbines: An Experimental Investigation of the Flame Stability, Emissions and Temperature Boundary Condition. *Flow, Turbulence and Combustion, 89*(2), 261-274.

Dukhan, N., Bağcı, Ö., & Özdemir, M. (2014). Metal foam hydrodynamics: Flow regimes from pre-Darcy to turbulent. *International journal of heat and mass transfer, 77*, 114-123.

Dumas, M. (2016). *Modélisation et simulation du comportement d'une tige fémorale poreuse.* (M.A.Sc.), École de technologie supérieure, Montréal.

Dumas, M., Terriault, P., & Brailovski, V. (2017). Modelling and characterization of a porosity graded lattice structure for additively manufactured biomaterials. *Materials & Design, 121*, 383-392.

Durst, F., Trimis, D., & Pickenäcker, K. (1997). Compact porous medium burner and heat exchanger for household applications. *Contract No. JOE3-CT95-0019, University of Erlangen-Nuremberg*.

Eichhorn, F., Biggemann, J., Kellermann, S., Kawai, A., Kato, K., Kakimoto, K., & Fey, T. (2017). Influence of Cell Size on Mechanical and Piezoelectric Properties of PZT and LNKN Ceramic Foams. *Advanced Engineering Materials, 19*(10), 1700420.

El-Mahallawy, F., & El-Din Habik, S. (2002). *Fundamentals and technology of combustion*: Elsevier.

Elverum, P. J., Ellzey, J. L., & Kovar, D. (2005). Durability of YZA ceramic foams in a porous burner. *Journal of Materials Science, 40*(1), 155-164.

EngiCer. Material Data Sheet: SiSiC. Retrieved from http://www.engicer.com/wp-content/uploads/materialdatasheet/EngiCer_Material_Data_Sheet_SiSiC.pdf

EOS. (2011). Material data sheet: EOS CobaltChrome MP1. Retrieved from http://ip-saas-eos-cms.s3.amazonaws.com/public/4b839242298b3d77/721463526ca053889c9784ec989f3c88/EOS_CobaltChrome_MP1_en.pdf

ERG Materials and Aerospace Corp. The Basics of Duocel® Foam. Retrieved from http://ergaerospace.com/technical-data/the-basics-of-duocel-foam/

Ergun, S., & Orning, A. A. (1949). Fluid Flow through Randomly Packed Columns and Fluidized Beds. *Industrial & Engineering Chemistry, 41*(6), 1179-1184.

Figliola, R. S., & Beasley, D. E. (2011). *Theory and design for mechanical measurements*: John Wiley & Sons, Inc.

Fleck, N. A. (2004). An overview of the mechanical properties of foams and periodic lattice materials. *Cell Met Polym*, 3-7.

Francisco Jr., R. W., Rua, F., Costa, M., Catapan, R. C., & Oliveira, A. A. M. (2009). On the combustion of hydrogen-rich gaseous fuels with low calorific value in a porous burner. *Energy & Fuels, 24*(2), 880-887.

Fu, X., Viskanta, X. F., & Gore, J. P. (1998). Measurement and correlation of volumetric heat transfer coefficients of cellular ceramics. *Experimental thermal and fluid science, 17*(4), 285-293.

Fu, Z., Schlier, L., Travitzky, N., & Greil, P. (2013). Three-dimensional printing of SiSiC lattice truss structures. *Materials Science & Engineering A: Structural Materials: Properties, Microstructure and Processing, 560*, 851-856.

FXI. (2014). Function Sheet: Filtering. Retrieved from http://fxi.com/assets/pdf/FS_MEC4.pdf

Gao, H., Qu, Z., Tao, W., He, Y., & Zhou, J. (2011). Experimental study of biogas combustion in a two-layer packed bed burner. *Energy & Fuels, 25*(7), 2887-2895.

Gao, H. B., Qu, Z. G., Feng, X. B., & Tao, W. Q. (2014). Methane/air premixed combustion in a two-layer porous burner with different foam materials. *Fuel, 115*, 154-161.

Gauthier, S., Nicolle, A., & Baillis, D. (2008). Investigation of the flame structure and nitrogen oxides formation in lean porous premixed combustion of natural gas/hydrogen blends. *International journal of hydrogen energy, 33*(18), 4893-4905.

Ghanbari-Bavarsad, P. (2008). *Modeling stretched methane-air flame growth.* (M.A.Sc.), University of Windsor, Windsor, Ontario, Canada.

Gianella, S. (2013). Porous Ceramics for CSP Applications: New opportunities to increase solar absorber efficiency. Retrieved from http://www.engicer.com/wp-content/uploads/presentations/Porous_Ceramics_for_CSP_Workshop_2013.pdf

Gianella, S., & Ortona, A. (2010). *Si-SiC Reticulated Foams for High Temperature Applications.* Paper presented at the CELLMAT 2010: Cellular Materials, Dresden, Germany.

Gibson, L. J., & Ashby, M. F. (1988). *Cellular Solids: Structure And Properties* (Vol. 9).

Gibson, L. J., & Ashby, M. F. (1997). *Cellular Solids: Structure and Properties* (2 ed.). Cambridge: Cambridge University Press.

GoGas. (2008). Porous Burner - A New Approach to Infrared. Retrieved from http://www.superiorradiant.com/sites/default/files/product_documents/SRP-GoGaS-RADIMAX.pdf

Grosse, J., Dietrich, B., Garrido, G. I., Habisreuther, P., Zarzalis, N., Martin, H., . . . Kraushaar-Czarnetzki, B. (2009). Morphological characterization of ceramic sponges for applications in chemical engineering. *Industrial & engineering chemistry research, 48*(23), 10395-10401.

Hardesty, D. R., & Weinberg, F. J. (1974). Burners Producing Large Excess Enthalpies. *Combustion Science and Technology, 8*(5-6), 201-214.

Heywood, J. B. (1988). *Internal combustion engine fundamentals*.

Horsman, A. P. (2010). *Design Optimization of a Porous Radiant Burner.* (M.A.Sc.), University of Waterloo, Waterloo, Ontario, Canada.

Howell, J. R., Hall, M. J., & Ellzey, J. L. (1996). Combustion of Hydrocarbon Fuels within Porous Inert Media *Progress in Energy and Combustion Science, 22*(2), 121-145.

Hsu, P.-F., Evans, W. D., & Howell, J. R. (1993). Experimental and numerical study of premixed combustion within nonhomogeneous porous ceramics. *Combustion Science and Technology, 90*(1-4), 149-172.

Hsu, P.-F., & Howell, J. R. (1992). Measurements of Thermal Conductivity and Optical Properties of Porous Partially Stabilized Zirconia. *Experimental Heat Transfer, 5*(4), 293-313.

Huang, R., Cheng, L., Qiu, K., Zheng, C., & Luo, Z. (2016). Low-Calorific Gas Combustion in a Two-Layer Porous Burner. *Energy & Fuels, 30*(2), 1364-1374.

Innocentini, M. D. M., Salvini, V. R., Macedo, A., & Pandolfelli, V. C. (1999). Prediction of ceramic foams permeability using Ergun's equation. *Materials Research, 2*, 283-289.

Jetté, B., Brailovski, V., Dumas, M., Simoneau, C., & Terriault, P. (2018). Femoral stem incorporating a diamond cubic lattice structure: Design, manufacture and testing. *Journal of the Mechanical Behavior of Biomedical Materials, 77*, 58-72.

Jones, A. R., Lloyd, S. A., & Weinberg, F. J. (1978). Combustion in heat exchangers. *Proceedings of the Royal Society of London. A. Mathematical and Physical Sciences, 360*(1700), 97-115. doi:10.1098/rspa.1978.0059

Joo, H. I., Duncan, K., & Ciccarelli, G. (2006). Flame-Quenching Performance of Ceramic Foam. *Combustion Science and Technology, 178*(10-11), 1755-1769.

Keramiotis, C., Stelzner, B., Trimis, D., & Founti, M. (2012). Porous burners for low emission combustion: An experimental investigation. *Energy, 45*(1), 213-219.

Khanna, V., Goel, R., & Ellzey, J. L. (1994). Measurements of Emissions and Radiation for Methane Combustion within a Porous Medium Burner. *Combustion Science and Technology, 99*(1-3), 133-142.

Kiefer, J., Weikl, M. C., Seeger, T., von Issendorff, F., Beyrau, F., & Leipertz, A. (2009). Non-intrusive gas-phase temperature measurements inside a porous burner using dual-pump CARS. *Proceedings of the Combustion Institute, 32*(2), 3123-3129.

Lapalme, D., Lemaire, R., & Seers, P. (2017). Assessment of the method for calculating the Lewis number of H2/CO/CH4 mixtures and comparison with experimental results. *International journal of hydrogen energy, 42*(12), 8314-8328.

Lewis, K. M., Kijak, I., Reuter, K. B., & Szabat, J. B. (1996). An image analysis method for cell-size and cell-size distribution measurement in rigid foams. *Journal of Cellular Plastics, 32*(3), 235-259.

Liu, S., Afacan, A., & Masliyah, J. (1994). Steady incompressible laminar flow in porous media. *Chemical Engineering Science, 49*(21), 3565-3586.

Lyamin, G. A., & Pinaev, A. V. (1987). Combustion regimes for gases in an inert porous material. *Combustion, explosion, and shock waves, 22*(5), 553-558.

Mach, F. R. A., Issendorff, F. V., Delgado, A., & Ortona, A. (2009). Experimental Investigation of the Oxidation Behaviour of SiSiC Foams *Advances in Bioceramics and Porous Ceramics: Ceramic Engineering and Science Proceedings, Volume 29, Issue 7* (pp. 299-311): John Wiley & Sons, Inc.

Mangan, A. P., & Whitaker, R. T. (1999). Partitioning 3D surface meshes using watershed segmentation. *IEEE Transactions on Visualization and Computer Graphics, 5*(4), 308-321.

Mathis, W. M., & Ellzey, J. L. (2003). Flame stabilization, operating range, and emissions for a methane/air porous burner. *Combustion Science and Technology, 175*(5), 825-839.

McAllister, S., Chen, J.-Y., & Fernandez-Pello, A. C. (2011). *Fundamentals of Combustion Processes*: Springer.

Mital, R., Gore, J. P., & Viskanta, R. (1997). A study of the structure of submerged reaction zone in porous ceramic radiant burners. *Combustion and flame, 111*(3), 175-184.

Mößbauer, S., Durst, F., Trimis, D., & Haas, T. (2001). *Zero Emission Engine : A Novel Steam Engine for Automotive Applications((NCS-3)Novel Combustion Systems 3-Homogeneous Charge, Premixed Charge Compression Ignition Engines)*. Paper presented at the Proceedings The 5th International Symposium on Diagnostics and Modeling of Combustion in Internal Combustion Engines (COMBURA 2001), Nagoya.

Mujeebu, M. A., Abdullah, M. Z., Abu Bakar, M. Z., Mohamad, A. A., Muhad, R. M. N., & Abdullah, M. K. (2009). Combustion in porous media and its applications – A comprehensive survey. *Journal of environmental management, 90*(8), 2287-2312.

Mujeebu, M. A., Abdullah, M. Z., Bakar, M. Z. A., & Mohamad, A. A. (2011). A Mesoscale Premixed LPG Burner with Surface Combustion in Porous Ceramic Foam. *Energy sources. Part A, Recovery, utilization, and environmental effects, 34*(1), 9-18.

Ortona, A., D'Angelo, C., Gianella, S., & Gaia, D. (2012). Cellular Ceramics Produced by Rapid Prototyping and Replication. *Materials Letters, 80*, 95-98. doi:10.1016/j.matlet.2012.04.050

Ortona, A., Pusterla, S., D'Angelo, C., Barbato, M., Gianella, S., & Gaia, D. (2012). *Si-SiC reticulated macroporous foams: processing, properties, and applications*. Paper presented at the MCARE, Clearwater Beach.

Ouimette, P., & Seers, P. (2009). Numerical comparison of premixed laminar flame velocity of methane and wood syngas. *Fuel, 88*(3), 528-533.

Pilusa, T., Mollagee, M., & Muzenda, E. (2012). Reduction of vehicle exhaust emissions from diesel engines using the whale concept filter. *Aerosol and Air Quality Research, 12*(5), 994-1006.

Pitois, O., Lorenceau, E., Louvet, N., & Rouyer, F. (2009). Specific Surface Area Model for Foam Permeability. *Langmuir, 25*(1), 97-100.

Richardson, J. T., Peng, Y., & Remue, D. (2000). Properties of ceramic foam catalyst supports: pressure drop. *Applied catalysis A: General, 204*(1), 19-32.

Rørtveit, G. J., Zepter, K., Skreiberg, Ø., Fossum, M., & Hustad, J. E. (2002). A comparison of low-NOx burners for combustion of methane and hydrogen mixtures. *Proceedings of the Combustion Institute, 29*(1), 1123-1129.

Sathe, S. B., Kulkarni, M. R., Peck, R. E., & Tong, T. W. (1991). An experimental and theoretical study of porous radiant burner performance. *Symposium, International, on Combustion, 23*(1), 1011-1018.

Sathe, S. B., Peck, R. E., & Tong, T. W. (1990). A numerical analysis of heat transfer and combustion in porous radiant burners. *International journal of heat and mass transfer, 33*(6), 1331-1338.

Scheffler, M., & Colombo, P. (2005). *Cellular Ceramics: Structure, Manufacturing, Properties and Applications*: Wiley-VCH Verlag GmbH & Co. KGaA.

Schindelin, J., Arganda-Carreras, I., Frise, E., Kaynig, V., Longair, M., Pietzsch, T., . . . Cardona, A. (2012). Fiji - an Open Source platform for biological image analysis. *Nature methods, 9*(7).

Schlegel, A., Benz, P., & Buser, S. (1993). Wärmeübertragung und Druckabfall in keramischen Schaumstrukturen bei erzwungener Strömung. *Wärme - und Stoffübertragung, 28*(5), 259-266.

Shao, Z., & Dallmann, T. (2016). European Stage V non-road emission standards. *The International Council on Clean Transportation*.

Smucker, M. T., & Ellzey, J. L. (2004). Computational and Experimental Study of a Two-Section Porous Burner. *Combustion Science and Technology, 176*(8), 1171-1189.

Stone, R., Clarke, A., & Beckwith, P. (1998). Correlations for the Laminar-Burning Velocity of Methane/Diluent/Air Mixtures Obtained in Free-Fall Experiments. *Combustion and flame, 114*(3), 546-555.

Takeno, T., & Hase, K. (1983). Effects of Solid Length and Heat Loss on an Excess Enthalpy Flame. *Combustion Science and Technology, 31*, 207-215.

Takeno, T., & Sato, K. (1979). An Excess Enthalpy Flame Theory. *Combustion Science and Technology, 20*, 73-84.

Takeno, T., Sato, K., & Hase, K. (1981). A theoretical study on an excess enthalpy flame. *Symposium, International, on Combustion, 18*(1), 465-472.

Trimis, D., & Durst, F. (1996). Combustion in a Porous Medium-Advances and Applications. *Combustion Science and Technology, 121*(1-6), 153-168.

Trimis, D., & Wawrzinek, K. (2004). Flame Stabilization of Highly Diffusive Gas Mixtures in Porous Inert Media. In J. Vad, T. Lajos, & R. Schilling (Eds.), *Modelling Fluid Flow: The State of the Art* (pp. 107-121). Berlin, Heidelberg: Springer Berlin Heidelberg.

Turns, S. R. (2000). *An introduction to combustion : concepts and applications, second edition*: McGraw-Hill Co.

Vedula, V. R., Green, D. J., & Hellman, J. R. (1999). Thermal shock resistance of ceramic foams. *Journal of the American Ceramic Society, 82*(3), 649-656.

Videla, A., Lin, C.-L., & Miller, J. D. (2006). Watershed Functions Applied to a 3D Image Segmentation Problem for the Analysis of Packed Particle Beds. *Particle & Particle Systems Characterization, 23*(3-4), 237-245.

Volume Graphics, G. (2016). *VGStudio MAX 3.0. Reference Manual*

Vrana, R., Koutny, D., & Paloušek, D. (2016). Impact resistance of different types of lattice structures manufactured by SLM. *MM Science Journal, 2016*(06), 1579-1585. doi:10.17973/MMSJ.2016_12_2016186

Weinberg, F. J. (1971). Combustion Temperatures: The Future? *Nature, 233*(5317), 239-241.

Wellington, S. L., & Vinegar, H. J. (1987). X-ray computerized tomography. *Journal of Petroleum Technology, 39*(08), 885-898.

Wharton, J. A., Ellzey, J. L., & Bogard, D. G. (2005). An experimental study of turbulence intensities and non-uniformities in the exit flow from a porous combustor. *Experiments in Fluids, 38*(6), 701-707.

Williams, A., Woolley, R., & Lawes, M. (1992). The formation of NOx in surface burners. *Combustion and flame, 89*(2), 157-166.

Williams, A. M., Garner, C. P., & Binner, J. G. P. (2008). Measuring pore diameter distribution of gelcast ceramic foams from two-dimensional cross sections. *Journal of the American Ceramic Society, 91*, 3113-3116.

Wood, S., & Harris, A. T. (2008). Porous burners for lean-burn applications. *Progress in Energy and Combustion Science, 34*(5), 667-684.

Wu, C.-Y., Chen, K.-H., & Yang, S. Y. (2014). Experimental study of porous metal burners for domestic stove applications. *Energy conversion and management, 77*, 380-388.

Xu, W., Zhang, H., Yang, Z., & Zhang, J. (2008). Numerical investigation on the flow characteristics and permeability of three-dimensional reticulated foam materials. *Chemical Engineering Journal, 140*(1), 562-569.

Zhu, X.-K., & Joyce, J. A. (2012). Review of fracture toughness (G, K, J, CTOD, CTOA) testing and standardization. *Engineering Fracture Mechanics, 85*, 1-46.

Zimmermann, J. W., Hilmas, G. E., & Fahrenholtz, W. G. (2008). Thermal shock resistance of ZrB2 and ZrB2–30% SiC. *Materials Chemistry and Physics, 112*(1), 140-145.